ANKARA YILDIRIM BEYAZIT UNIVERSITY

GRADUATE SCHOOL OF NATURAL AND APPLIED SCIENCES

WELDABILITY PROCESS AND POST-WELD MECHANICAL AND MICROSTRUCTURAL ANALYSIS OF DIFFERENT STEELS

M.Sc. Thesis by

Yasin SANCAR

Department of Mechanical Engineering

December, 2022

ANKARA

WELDABILITY PROCESS AND POST-WELD MECHANICAL AND MICROSTRUCTURAL ANALYSIS OF DIFFERENT STEELS

A Thesis Submitted to

The Graduate School of Natural and Applied Sciences of

Ankara Yıldırım Beyazıt University

In Partial Fulfillment of the Requirements for the Degree of Master of Science in Mechanical Engineering, Department of Mechanical Engineering

by

Yasin SANCAR

December, 2022

ANKARA

M.Sc. THESIS EXAMINATION RESULT FORM

We have read the thesis entitled "**WELDABILITY PROCESS AND POST-WELD MECHANICAL AND MICROSTRUCTURAL ANALYSIS OF DIFFERENT STEELS**" completed by **YASİN SANCAR** under the supervision of **Assist. Prof. Dr. YASİN SARIKAVAK** and we certify that in our opinion it is fully adequate, in scope and in quality, as a thesis for the degree of Master of Science.

Assist. Prof. Dr. Yasin SARIKAVAK

Supervisor

Assoc. Prof. Dr. Tunç APATAY

Jury Member

Prof. Dr. Adem ÇİÇEK

Jury Member

Prof. Dr. Sadettin ORHAN

Director

Graduate School of Natural and Applied Sciences

ETHICAL DECLARATION

I hereby declare that, in this thesis which has been prepared in accordance with the Thesis Writing Manual of Graduate School of Natural and Applied Sciences,

- All data, information and documents are obtained in the framework of academic and ethical rules,
- All information, documents and assessments are presented in accordance with scientific ethics and morals,
- All the materials that have been utilized are fully cited and referenced,
- No change has been made on the utilized materials,
- All the works presented are original,

and in any contrary case of above statements, I accept to renounce all my legal rights.

Date: **Signature: ……**

Name & Surname:……...…

ACKNOWLEDGMENTS

Firstly, I would like to express my sincere gratitude to my supervisor, Assist. Prof. Dr. Yasin SARIKAVAK for his continuous support and practical suggestions.

Beside my advisor, I would like to thank Ankara Yıldırım Beyazıt University Scientific Research Projects Coordination Unit for providing financial support to the Project No: FYL-2021-2282. I would like to acknowledge the AYBU Metallurgical and Materials Engineering Department, which made use of its laboratory facilities, for their support. I would also like to thank Bahadır AYDAŞ, Uğur BARUT and Necati UÇAK for their assistance in the microstructural investigation. I would like to extend my deepest gratitude to my family for their invaluable contribution and financial supports.

2022, 30 December **Yasin SANCAR**

WELDABILITY PROCESS AND POST-WELD MECHANICAL AND MICROSTRUCTURAL ANALYSIS OF DIFFERENT STEELS

ABSTRACT

Dissimilar materials with different properties can be joined by various welding methods under different boundary conditions. Gas metal arc welding (GMAW) is one of the most widely used welding methods among the melting-based welding processes. GMAW has many advantages in terms of applicability and extensively used in the metal manufacturing industry. In practice joining dissimilar steel sheets frequently conducted however weld quality strongly dependent to boundary conditions during the welding process. Joining dissimilar alloy steels by GMAW finds applications various industries such as manufacturing, aviation, defense and automotive. Therefore, in this study 10 mm thick dissimilar steel sheets are joined by GMAW under various boundary conditions. Post weld mechanical and microstructural behaviors are investigated in detail. For the process in experimental design three level variables of parameters i.e., welding speed, welding current and welding voltage were used for the Taguchi L9 orthogonal array where tensile, impact and hardness tests were conducted, and microstructural properties investigated in detail. Frequently used dissimilar St37 and St52 steel sheet materials with a thickness of 10 mm were joined with ‘V’ butt weld and SG-2 electrode wire. In terms of mechanical strength, the contribution of each variable was evaluated in detail and optimum welding parameters were clarified with gray relational analysis as 35 V, 330 A and 250 mm/min. Tempering processes with three level were applied to the optimum materials to increase the mechanical strength. Then, the effect of tempering process on mechanical properties and microstructure was investigated in detail.

Keywords: Gas metal arc welding (GMAW), taguchi method, optimization, mechanical properties, tempering.

FARKLI ÇELİKLERİN KAYNAKLANABİLİRLİĞİ VE KAYNAK SONRASI MEKANİK VE MİKROYAPISAL ANALİZİ

ÖZ

Günümüzde farklı özellikteki malzemelerin kaynağı çeşitli kaynak yöntemleri ile yapılabilmektedir. Gaz metal ark kaynağı, ergitme esaslı kaynak işlemleri arasında en yaygın olarak kullanılan kaynak yöntemlerinden biridir. Gaz metal ark kaynağı uygulanabilirlik açısından birçok avantaja sahiptir ve metal imalat sanayinde yaygın olarak kullanılmaktadır. Kaynak kalitesi, kaynak işlemi sırasında uygulanan sınır koşullarına bağlıdır. Farklı alaşım özelliklerine sahip çelik malzemelerin gaz altı kaynağı yöntemiyle birleştirilmesi imalat sanayi, havacılık, savunma sanayi ve otomotiv sanayi gibi birçok alanda kullanılmaktadır. Bu nedenle, bu çalışmada farklı özelliklere sahip düşük alaşımlı çelik malzemeler gaz altı kaynağı yöntemiyle çeşitli sınır koşulları altında birleştirilmiştir. Kaynak sonrası numunelere mekanik testler uygulanarak mekanik davranışları detaylı olarak incelenmiştir. Mekanik özelliklerin detaylı olarak incelendiği deney tasarımında Taguchi L9 ortogonal dizilimi için prosesin üç seviyeli değişkeni olan kaynak hızı, kaynak akımı ve kaynak voltajı kullanılmıştır. Bu çalışmada 10 mm kalınlığında St37 ve St52 düşük alaşımlı çelik malzemeler, SG-2 elektrot teli kullanılarak V alın kaynağı yöntemi ile birleştirilmiştir. Mekanik dayanım kapsamında optimum kaynak parametreleri netleştirilerek değişkenlerin katkısı detaylı olarak değerlendirilmiş ve tanımlanan değişkenler altında en yüksek darbe dayanımı 35 V, 330 A ve 250 mm/dk kaynak hızı şartlarında elde edilmiştir. Elde edilen optimum parametreler ile birleştirilen üç malzemeye artık gerilmeleri azaltarak mekanik mukavemeti artırmak için temperleme işlemleri uygulanmıştır. Daha sonra temperleme işleminin mekanik özelliklere ve mikroyapıya etkisi incelenmiştir.

Anahtar Kelimeler: Gaz metal ark kaynağı, taguchi yöntemi, optimizasyon, mekanik özellikler, temperleme.

CONTENTS

NOMENCLATURE

Subscripts

℃	Celsius Degree
I	Current
V	Voltage
J	Joule
HV	Vickers Hardness
L_0	First Length
mm	Milimeter
$R_{p0.2}$	Yield Strength
R_{eH}	Upper Yield Point
R_{eL}	Lower Yield Point
R_m	Tensile Strength
µm	Micrometer

Acronyms

GMAW	Gas Metal Arc Welding
ANOVA	Analysis of Variance
ASTM	American Society for Testing and Materials
DF	Degree of freedom
PF	Polygonal Ferrite
AF	Acicular Ferrite
WF	Widmanstatten Ferrite
HAZ	Heat Affected Zone
WM	Weld Metal
PTS	Predict Tensile Strength
SS	Sum of Square
SEM	Scanning Electron Microscope
XRD	X-Ray Diffraction
MS	Mean Square

LIST OF TABLES

LIST OF FIGURES

CHAPTER 1

INTRODUCTION

Welding methods are widely used in many industry fields such as aerospace, defense, and automotive. The characteristics of the welding process vary according to the application areas. For joining dissimilar materials gas metal arc welding (GMAW) is one of the most widely used method among the melting-based welding methods and its application frequency increasing day by day. GMAW has been developed earlier and still find many applications in the metal manufacturing industry because of the many advantages. Ensuring the safety of the welded parts is critical to the reliability of the entire structure in which the weld joints represent a discontinuity in the system. Therefore, in this study, an optimization conducted to improve mechanical properties of dissimilar low alloyed steels joined by GMAW method. Post weld mechanical and microstructural analysis were conducted.

St37-2 and St52-3 structural steels which have low carbon ratio, good weldability and ductility properties are frequently used due to its low production cost, and in many sectors. Thus, in this study, it is aimed to join 10 mm thick St37-2 and St52-3 steel materials via GMAW to clarify optimum welding conditions in terms of mechanical and microstructural properties. DIN 8559 (SG-2) electrode wire with 1 mm diameter and mixed gas was used as shielding gas in welding process. In design of experiment three level variables of parameters i.e., welding speed, welding current and welding voltage were used for the Taguchi L9 orthogonal array where mechanical and microstructural properties were investigated in detail. Single V butt welding was used in the welding process. Tensile test, hardness test, Charpy V notch impact test and microstructural analysis were applied to the welded samples. Optimization of welding parameters were analyzed by using Taguchi L9 orthogonal array.

In the scope of mechanical strength, the contribution of each variable was evaluated in detail and optimum welding parameters were clarified. Under optimum boundary conditions three level of tempering processes were applied to the welded joints to

increase the mechanical strength by reducing the residual stresses. Then, the effect of tempering process on mechanical properties and microstructure were investigated in detail. By examining the effects of the temper temperature, the ideal temper temperature was determined for the weld sample combined with the optimum welding parameters.

In chapter 2, the studies in the literature on the weldability of steel materials and their post-weld mechanical and microstructural analysis are explained in detail. In chapter 3, the details of the method carried out within the scope of the experimental work are presented. In chapter 4, mechanical test results and microstructure analyzes obtained within the scope of the experimental study are presented. The results of the optimization process performed according to the test results are also included in this section. In chapter 5, information about the conclusion and future works is presented.

CHAPTER 2

LITERATURE REVIEW

In 1930, the use of an inert gas as a shielding gas was patented by Hobart and Devers in the United States. In 1940, it was used by the Nortrop Aircraft Company for the welding of magnesium and its alloys in aircraft construction. Here, first helium gas was used, and then in 1942, light metals and their alloys were welded by Linde Air Product Company and Union Carbide and Carbon Corporation using both helium and argon gases. The first studies on the use of an active gas such as carbon dioxide in the source area other than inert gases were started in 1952. Today, various gas arc welding methods are available, using various inert gases and active gases, with the same equipment but different gas mixtures [1].

Hakam Muzakki et al. investigated the welding parameters of Metal Inert Gas (MIG) which affected to tensile strength of weld joint. In this study, ST37 steel sheet with 0,3 mm thickness was used as a material. Tensile strength values were measured at the different welding current, wire speed, and welding speed. The welding current level was 80 A, 90 A and 100 A. Wire speed was set to 55 inch/min, 60 inch/min, and 65 inch/min. The levels of welding speed were 5 mm/sec, 6 mm/sec and 7 mm/sec. The highest tensile strength was obtained with welding current 100 A, wire speed 60 inch/min and welding speed 5 mm/sec. Increasing welding speed affected the tensile strength tend to decrease, it was different with welding current, increasing welding current effected tensile strength average also increase [2].

S.Utkarsh et al. performed the experimental investigation of MIG welding for ST37. In this study, ST37 steel with 6 mm thickness was used as base material. ER70S-6 with 0.9 mm diameter was used as electrode. Tensile strength was examined at different parameters such as current, voltage, welding speed, and gas flow rate. The welding current level was 110 A, 120 A, and 130 A. Voltage was set to 21 V, 22 V, and 23 V. The levels of welding speed were 4.5 m/min, 5.5 m/min, and 6.5 m/min. The levels of gas flow rate were 8 L/min, 9 L/min, and 10 L/min. The parameters obtained after the Taguchi experiment for ultimate tensile strength (UTS) were found

as 110 A, 22 V, 5.5 m/min, and 9 L/min. When the current is too low, the molten metal cannot wet the joint surface, causing a lack of fusion. The melting rate of the electrode increases with increasing current. The arc voltage to be used depends on the base metal thickness, type of joint, electro composition and size, shielding gas composition, welding position, type of weld and other factors. The experimental results show that among the input parameters, voltage and current have the greatest effect on the weld strength and it was observed that gas flow rate does not affect the weld strength [3].

S. R. Patil and C. A. Waghmare investigated the influence of welding parameters like welding current, welding voltage, welding speed on UTS of AISI 1030 mild steel material with 10 mm thickness during welding. ER70S-6 with a 1.2 mm diameter was used as electrode. The welding current level was 200 A, 220 A, and 240 A. Voltage was set to 23 V, 25 V, and 27 V. The levels of welding speed were selected as 250 mm/min, 350 mm/min, and 450 mm/min. Taguchi method was used to determine the maximum ultimate tensile strength and process parameters in GMAW for plan carbon steel. The optimum levels obtained after the Taguchi experiment for UTS are 240 A, 27 V, and 450 mm/min. The results show that the effect of welding speed is significant among the main input welding parameters. Increasing the welding speed and decreasing the current increases the UTS of the welded joint. According to the experiment results, the voltage did not contribute as such to weld strength. It was found that welding speed has major influence on tensile strength of welded joints. Thus, a little variation in the welding speed is expected to greatly affect the tensile strength of the weld. Hence, the more the welding speeds, higher the strength. From this study, it is observed that welding current and welding speed are major parameters which influence on the tensile strength of welded joint [4].

T Appa Rao et al. investigated the optimization of MIG welding parameters for improving strength of welded joints. In the study, AISI 1050 mild steel was used as base material. In this study, experiments were made to understand the effect of MIG welding parameters welding speed, welding current and welding voltage on output parameters such as hardness of welding, tensile strength of welding. The welding current level was 180 A, 230 A, and 280 A. Voltage was set to 22 V, 24 V, and 26 V. The levels of welding speed were selected as 200 m. m/s, 300 m. m/s, and 400 m. m/s.

The optimum levels obtained after the Taguchi experiment for UTS are 180 A, 26 V, and 400 m. m/s. According to the experiment results, the tensile strength increased when the welding current was decreased. From this study, it is observed that welding current and welding speed are major parameters which influence on the tensile strength of welded joint [5].

Ajit Hooda et al. investigated the optimization of MIG welding process parameters to predict maximum yield strength in AISI 1040 with 8 mm thickness. ER 70S-6 with a diameter of 1.2 mm was selected as welding wire. In this study, the effect of the process parameters such as voltage, wire speed, welding current and gas flow rate on the weld joint yield strength both transverse and longitudinal has been investigated. The welding current level was 190 A, 200 A, and 210 A. Voltage was set to 23 V, 24 V, and 25 V. The levels of wire speed were selected as 2.4 m/min, 2.8 m/min, and 3.2 m/min. The levels of gas flow rate were selected as 12 L/min, 14 L/min, and 16L/min. The optimum levels obtained for transverse yield strength are 190 A, 22.5 V, 12 L/min, and 2.4 m/min. The optimum levels obtained for longitudinal yield strength are 210 A, 22.5 V, 12 L/min, and 2.4 m/min. It was found that the longitudinal yield strength was greater than the transverse yield strength because of experiments [6].

Biswajit Das et al. investigated the influence of process parameters on depth of penetration of welded joint in MIG welding process. The low carbon steel of grade EN-3A with 6 mm thickness was used as a base material. EN-3A electrode wire with a diameter of 1.2 mm was used in experiments. Welding speed, voltage and current are considered as design factors in this study. The welding current level was 140 A, 150 A, 160 A, 170 A, and 180 A. Voltage was set to 24 V, 25 V, 26 V, 27 V, and 28 V. The levels of welding speed were selected as 0.165 m/min, 0.179 m/min, 0.193 m/min, 0.206 m/min, and 0.220 m/min. As current and voltage increase, it creates more heat, therewith more metal melts, thus creates greater depth of penetration. It was obtained that higher voltage causes sudden increase in penetration depth, and very high current also causes the same thing because of experiments. In the experiments, it was observed that very high welding speed caused a decrease in the penetration depth [7].

Nabendu Ghosh et al. investigated the effects of welding parameters on maximum tensile strength and yield strength in MIG welding. AISI 409 ferritic stainless steel and AISI 316L Austenitic Stainless-Steel materials with 3 mm thickness were used as material. AISI 308L austenitic filler wire was used as welding electrode. The effects of welding parameters such as welding current, gas flow rate and nozzle-plate distance were examined in this study. Three different current values were selected as 100 A, 112 A, and 124 A. Gas flow rate values were selected as 10 L/min, 15 L/min, and 20 L/min. Nozzle to plate distance were set as 9 mm, 12 mm, and 15 mm. The maximum UTS value was obtained at 112 A (current), 15 L/min (gas flow rate), 15 mm (nozzle to plate distance) [8].

Vishvesh Dixit et al. investigated the effect of changing welding current with constant voltage on the impact strength of weld seams made of similar and different materials. AISI 410 and AISI 1030 steels with 3.2 mm thickness were used in the experiment. Three different current values were selected as 120 A, 140 A, and 160 A. As a result of the experiment, among the three different weld joint categories, namely AISI 1030-AISI 1030, AISI 410-ISI 410 and AISI 1030-AISI 410 welded joints, the highest strength of the joint was obtained at 140 A in the AISI 410 - AISI 410 welded joint, and the lowest energy was obtained from the AISI 1030-AISI 410 welded joint at 120 A [9].

Vivek Singh et al. investigated the weld bead characteristics and optimization of GMAW of Nitrogen Strengthened Austenitic Stainless Steel. Austenitic stainless steel (AISI 201) with 5 mm thickness were used as base material. ER308L wire with a diameter of 1.2 mm was used as weld electrode. In this study, wire feed rate, voltage, nozzle to plate distance, and welding speed were selected as welding factors. The penetration and bead width increased with increase in wire feed rate. Wire feed rate, voltage and nozzle to plate distance were found as influencing factors in penetration according to the experiment results. Penetration and weld bead width increase with increase in wire feed rate and voltage, but they decrease with increasing nozzle to plate distance and welding speed. The wire feed rate and nozzle to plate distance were found as efficient factors on the weld reinforcement. A decrease in the weld reinforcement was observed when increase in voltage and welding speed [10].

H. R. Ghazvinloo et al. investigated the post weld mechanical strength of CK45 carbon steel. CK45 medium carbon steel in the form of a 20 mm thick plate was used as the base material. ER70S-6 wire with a diameter of 1.0 mm was used as weld electrode. After welding process, cylindrical tensile test specimens with a diameter of 5.64 mm and a length of 28 mm were extracted from the weld metals. In the study, voltage values were set as 23 V, 25 V, and 27 V. The welding current values were set as 100 A, 110 A, and 120 A. The welding speeds were selected as 42 cm/min, 62 cm/min, and 82 cm/min. Increasing the welding current from 100 A to 120 A resulted in a decrease in the yield strength and ultimate tensile strength of the weld metal. As the welding speed increased from 42 to 82 cm/min, the yield strength and ultimate tensile strength of the weld metal became higher. Increasing the voltage from 23 to 27 V led to a decrease in the yield strength and ultimate tensile strength of the weld metal [11].

Ramazan Kaçar et al. investigated the effect of controlled atmosphere on the MIG-MAG arc weldment properties. GMAW process was performed by using the same weld parameters in an argon atmosphere and a controlled atmosphere cabinet. In the experimental study, low carbon steel with 12 mm thickness and SG2 electrode with a diameter of 1 mm were used as base material and electrode, respectively. The GMAW process allows the evolution of electrochemical and thermochemical reactions between the arc plasma and the weld pool. The resulting oxygen, nitrogen and hydrogen content reduces the mechanical properties of the weld metal. In this study, a controlled atmosphere cabinet was designed to examine the changes in the mechanical and metallurgical properties. The results showed that welded materials obtained by the conventional GMAW, which was performed in argon atmosphere, exhibited lower tensile and yield strength compared to the other GMAW process, which was performed in controlled atmosphere cabinet. The toughness of the weld metal obtained in the controlled atmosphere cabinet was much higher than in the conventional GMAW process according to the experiment results. The metallographic examination results also showed that there was no gas porosity and residue in the weld metal compared to the conventional process [12].

Amruta Rout et al. investigated a new approach formed by combining fuzzy regression with the Enhanced Teaching Learning Based Optimization (ETLBO) algorithm logic

to obtain the best weld quality. In this study, optimization of process variables of laser sensor assisted robotic GMAW process for mild steel material was examined. AISI 1030 with 5 mm thickness and ER70 S-6 wire with a diameter of 1.2 mm were used as base material and weld electrode, respectively. In the experiment, values of the welding voltage were selected as 18 V, 20 V, and 22 V. The values of welding current were set as 100 A, 120 A, and 140 A. The gas flow rates were selected as 10 L/min, 15 L/min, and 20 L/min. The welding gaps were set as 1 mm, 1.3 mm, and 1.6 mm. The values of wire stick out were selected as 10 mm, 12.5 mm, and 15 mm. The results of experiment such as yield strength test, ultimate strength test, micro hardness test, properties of weld bead examined, and optimum welding parameters were calculated. 1.25 mm (weld gap), 22 V (welding voltage), 131 A (welding current), 11 mm (wire stick out), and 12 L/min (gas flow rate) were determined as optimum welding parameters [13].

M. U. Deshpande et al. investigated the effects of welding parameters on penetration in materials joined by GMAW method. EN10025 S 235 steel with 3 mm thickness and ER70 S6 electrode wire with a diameter of 0.8 mm were used as base material and weld electrode, respectively. In the experiment, values of the welding voltage were selected as 16 V, 19 V, and 22 V. The values of welding current were set as 160 A, 190 A, and 220 A. The values of wire speed were selected as 8 m/min, 10 m/min, and 12 m/min. According to the test results, the best penetration was obtained at 160 A, 19 V, 12 m/min [14].

Arthur Casarini et al. investigated the geometric and mechanical properties of the weld jointed with GMAW using the Taguchi method and analysis of variance. In the experimental study, DIN C20 steel with 3 mm thickness and electrode wire with a diameter of 0.8 mm were used as base material and wire electrode. In the experiment, values of the welding voltage were selected as 22.4 V, 23.3 V, and 24.1 V. The values of welding speed were set as 200 mm/min, 300 mm/min, and 400 mm/min. The values of torch angle were selected as 0º, 15º, and 30º. Optimum levels for reinforcement were determined as 22.4 V, 400 mm/min, and 30°. Optimum levels for width were determined as 22.4 V, 300 mm/min, 0°. Optimum levels for penetration were determined as 23.3 V, 400 mm/min, and 0°. Optimum levels for ultimate transversal

tensile strength were determined as 24.1 V, 200 mm/min, 15°. The welding speed is the most influential parameter regarding the geometric parameters of the weld according to the test results. The angle of the welding torch has become the most important for ultimate transverse tensile strength [15].

William Hackenhaar et al. investigated the effect of welding parameters on fusion efficiency using the GMAW method. In the experimental study, AISI 1010 steel with 6.35 mm thickness and AWS ER70S-6 electrode wire with a diameter of 1.2 mm were used as base material and welding electrode, respectively. The effects of wire feed speed, voltage, and welding speed on the fusion efficiency were examined. The values of welding speed were set as 4 mm/sec, 5.5 mm/sec, and 7 mm/sec. The values of voltage were selected as 18 V, 20 V, and 22 V. The wire feed speeds were set as 3.5 m/min, 4.5 m/min, and 5.5 m/min. The melting efficiency is directly related to the heat flow extraction in the welded joint, and thus to the joint geometry. As a result of the experiment, an increase in the welding seam area and melting efficiency was determined because of increasing the welding current. According to the test results, it was observed that the seam width increased as the wire feed speed increased and the welding speed decreased, there was a common behavior for all three arc voltage levels, and the width increased as the arc voltage increased. The experiment results were confirmed the increase in melting efficiency as the welding speed increased [16].

Glauco Nobrega et al. examined the parameter optimization study on steel materials joined by the GMAW method. In this study, two austenitic stainless steel (X6CrNiTi18-10) pipes with 1.5 mm thickness were welded automatically. ESAB lead with a diameter of 1 mm was used as weld electrode. The values of welding current were set as 180 A, 200 A, and 214 A. The values of voltage were selected as 20.8 V, 23.8 V, and 25.6 V. The travel angles were set as 33°, 36°, and 53°. All experiments were carried out at a welding speed of 150 cm/min. In the experimental study, two quality welding parameters (weld root penetration and welding bead width) were examined. The optimum welding parameters for weld root penetration and welding bead width were obtained by using the Taguchi method. The optimum parameters for weld bead root penetration were found as, 150 cm/min, 20.8 V, 36º, and 180 A. The

optimum parameters for bead width were found as, 150 cm/min, 20.8 V, 53º, and a 180 A [17].

A. Kuppusamy et al. investigated the parameters affecting the pore defect in the longitudinal seam welding of pressure vessels. In the experimental study, IS 2062 E250BR steel with 4 mm thickness and AWS SFA 5.18 ER 70s6 wire were used as base material and weld electrode, respectively. The values of welding current were set as 280 A and 320 A. The values of travel speeds were selected as 400 mm/min and 500 mm/min. The gas flow rates were set as 11 L/min and 21 L/min. The values of torch angles were set as 3º and 5º. The values of wire stick out were 18 mm and 20 mm. The optimum parameters for good weld for without porosity were found by setting to current value of 280 A, travel speed of 450 mm/min, gas flow rate of 16 L/min, torch angle of 4º, and stick out distance of 19 mm [18].

The welding current is highly effective to obtain weld joint which has a good quality. Arunava et al. investigated the optimum parameters for the GMAW method under 100% Carbon Dioxide shielding gas in their study. In their study, they investigated the effects of welding parameters such as welding current, welding torch speed and voltage to obtain a quality weld joint. As a result of the study, they observed that the effect of the welding current is maximum to obtain a quality weld joint. The welding voltage was observed to be the least effective parameter in this study [19].

Shielding gas compositions have a great influence on the cooling rate due to the ionization potential of each shielding gas that controls to produce high or low heat input. Increasing the amount of CO2 in the shielding gas decreases the hardness of the weld metal. The required absorbed energy (impact toughness) of the weld metal decreases when the percentage of CO2 in the shielding gas increases. Byju John et al. investigated the effect of shielding gas on the metallurgical and corrosion properties of corten steel welded joints of railway coaches using GMAW. In their study, gas metal arc welding using shielding gas composition (80%Ar – 20% CO2), by keeping the parameters constant, obtained better mechanical, metallurgical and corrosion properties [20].

Mohamad Ebrahimnia et al. investigated the effect of the shielding gas composition on the welding properties of St 37-2 steel in gas metal arc welding. In their study, Charpy V-notch test and hardness test were examined. According to the experiment results, increasing the amount of carbon dioxide causes a decrease in the amount of residue and porosity. It was observed that due to the increase in the amount of CO_2 in the shielding gas composition, the hardness of the weld metal decreases. Charpy V-notch energy first increases and then remains constant as the amount of carbon dioxide in the shielding gas increases [21].

Mohamed Mezaache et al. investigated the maximum penetration depth in the GMAW method using particle swarm optimization. In the experimental study, 6 mm thick St37 material and 0.8 mm diameter ER70S-6 electrode wire was used. The welding voltage, welding speed, nozzle to plate distance, and wire feed speed were examined as input parameters in the experimental study. It was observed that the depth of penetration decreased when the voltage increased. If the welding speed was increased, the depth of penetration decreased. According to the experiment results, the depth of penetration increased when the wire feed speed increased. The voltage must be balanced with the wire feed speed to obtain an efficient metal transfer. If the nozzle to plate distance was increased, the depth of penetration was decreased because of the more resistance to the flow of electricity through the electrode occurs [22].

Vijaya Sankar B et al. investigated the optimization of welding parameters by examining the effect of welding current, welding voltage and gas flow rate with the Grey relational analysis (GRA) method. AISI 310 steel is used as base material. It was observed that lowering the welding current value increases the tensile strength and hardness value. Increasing the voltage value increases the tensile strength and decreases the hardness. According to the experiment results, increasing the gas flow rate value increases the tensile strength and decreases the hardness [23].

M. Azadi Moghaddam et al. investigated the multi criteria modeling and optimization procedure in GMAW process of API-X42 alloy. In the experimental study, weld seam geometry and heat affected zone were investigated. ER70S-6G4Si1 electrode wire with a diameter of 1 mm and API-X42 steel with 10 mm thickness were used in

experimental study. The heat input is most important factor affecting heat affected zone (HAZ). At the end of the study, optimized parameters values showed that both nozzle to plate distance and welding voltage should be set at their lower ends [24].

Cynthia S. Abima et al. investigated the welding parameters which provide the optimum tensile strength of AISI 1018 steel joined with the GMAW method. In the experimental study, AISI 1018 steel with 6 mm thickness and ER 70S/6 electrode wire were used. The values of welding current were set as 200 A, 250 A, and 280 A. The values of voltage were selected as 20 V, 25 V, and 30 V. The gas flow rates were set as 15 L/min, 17 L/min, and 19 L/min. The optimum welding parameters for optimum tensile strength were observed that the voltage of 30 V, current of 180 A, and gas flow rate of 17 L/mm. In this study, it was observed that the voltage had the most important effect on the tensile strength, followed closely by the gas flow rate. Welding current has the least effect on tensile strength. The surface plots in the study show that a lower voltage, higher welding current, and higher gas flow rate favored the maximum ultimate tensile strength [25].

A. G. Kamble et al. developed the mathematical models for weld bead height (HB), bead width (WB) and bead penetration (PB) and to investigate the effects of four process parameters such as welding voltage, welding speed, wire feed speed and gas flow rate. Welding bead geometry, hardness, and microstructure of AISI321 steel with 10 mm thickness were investigated. AISI308 electrode wire with a diameter of 1.2 mm was used as welding electrode. According to the experiment results, it was observed that the weld bead width increased with the increase in gas flow rate, voltage and wire feeding speed, and decreased with the increase in welding speed. The increase in welding voltage produces flatter, wider, less penetrating weld beads. The increase in voltage also increases the size of the droplets and thus reduces the number of droplets. An increase in the wire feed rate increases the amount of metal deposited and therefore the weld seam width will increase. At high welding speed, the volume of deposited metal is reduced and the heat input per unit length is reduced. According to the experiment results, while the weld bead height decreases with the increase in welding speed and wire feed rate, it increases with the increase in gas flow rate and voltage. With the increase in welding speed, less metal amount per unit length will accumulate

on the base metal and this will reduce the bead height. The melting of the base metal will be greater as the Voltage increases, resulting in a slight increase in bead height. Increase in gas flow rate produces high velocity plasma, resulting in an increase in fusion area and bead height. An increase in wire feed speed will deposit less molten metal on the base metal and therefore reduce the bead height. According to the experiment results, weld bead penetration decreases with an increase in welding speed. Weld bead penetration increases with the increase in gas flow rate, which fills the material into the weld bead groove and provides greater penetration in the bead. Increase in voltage and wire feed speed will deposit more molten metal inside the trough and increase penetration. According to the experiment results, it is seen that the hardness value increases with the increase in voltage, wire feeding speed and gas flow rate.

Hardness decreases with increasing welding speed. The hardness and HAZ in the weld zone are caused by the increased amount of carbon precipitation. If the hardness is too high, the weld strength will be high, and the ductility will be very low. The hardness decreases with distance from the HAZ [26].

Anusit Ampaiboon et al. examined the effect of welding parameters on the ultimate tensile strength. ST37-2 structural steel with 6 mm thickness was welded using the GMAW method. ER70S-6 electrode wire with a diameter of 0.8 mm was used as the electrode. Wire feed rate, welding voltage, welding speed, travel angle, tip to work distance and shielded gas flow rate were investigated as welding parameters. The values of welding voltage were set as 20V and 30V. The gas flow rates were set as 10 L/min and 20 L/min. The values of wire feed rate were set as 7 m/min and 19 m/min. The welding speed values were selected as 200 mm/min and 500 mm/min. The travel angle values were set as 60º and 80º. Tip to work distances were set as 7 and 15 mm. The optimum welding parameters for optimum tensile strength were observed that the voltage of 30 V, welding speed of 200 mm/min, travel angle of 80º, wire feed speed of 19 m/min, tip to work distance of 7 mm and gas flow rate of 10 L/min. The process parameters that showed the greatest to least effect on the UTS of the welded joint were during weld feed rate, tip to work distance, welding speed, welding voltage, and travel angle. The shielding gas flow rate in the selected range was found to have little effect.

The value of UTS increased with increasing weld feed rate, weld voltage and travel angle. In contrast, UTS increased with decreasing welding speed and tip to work distance [27].

Masood Aghakhani et al. investigated the parameter optimization in GMAW method by using the Imperialist Competitive Algorithm (IPA) method. St37 steel with a thickness of 6 mm and ER70S-6 electrode wire with a diameter of 0.8 mm were used as base material and weld electrode, respectively. In this study, the effects welding parameters such as wire feed rate, welding voltage, nozzle to plate distance, welding speed, and gas flow rate were examined. According to the experiment results, to obtain higher penetration depth and lower heat affected zone width at the same time; wire feed rate, welding voltage and nozzle to plate distance must be at the lowest level, while welding speed and gas flow rate must be at the highest level [28].

Amit Kumar et al. examined the welding parameter optimization in GMAW. In the experimental study, weld bead geometry and heat affected zone were investigated. AISI 1020 steel with a 6 mm thickness and ER 70 S-6 electrode wire with a diameter of 0.8 mm were used as base material and weld electrode, respectively. At the end of the study, it was observed that welding speed and welding voltage have a significant effect on the weld bead geometry, while the welding current has a reducing effect on the weld bead geometry. The effect of welding speed was observed to be the most significant. It has also been observed that the current has almost no effect on the bead geometry. Welding speed, welding voltage and welding current were found to be the most influential parameters on the weld bead geometry, respectively [29].

Shekhar Srivastava et al. investigated the effect of various process parameters on weld bead geometry and penetration in gas metal arc welding method. IS:2062 mild steel plate with a thickness of 6 mm and copper-clad soft electrode with a diameter of 0.8 mm were used as base material and weld electrode, respectively. In the study, it was aimed to minimize the weld seam width and seam height and to maximize the penetration depth. Preliminary study was carried out to determine the welding parameters. In the preliminary study, porosity at the weld edges and overlap in the weld bead were observed with a voltage lower than 24 V. On the other hand, if the

voltage is greater than 32 V; porosity, spatter and weld notch are seen. If the shielding gas flow rate is less than 10 L/min, air bubbles and defects in porosity have been observed. However, gas entrapment was observed if the gas flow rate was higher than 18 L/min. Superficial penetration, wider weld seam and overlap of the weld seam were observed for welding speed less than 160 mm/min. On the other hand, if it is higher than 220 mm/min for the welding speed, it will lead to incomplete fusion and low material deposition rate. With a wire feed speed higher than 9.5 m/min, poorly shaped weld bead and spatters were observed, while wire feed speed lower than 4.5 m/min caused less penetration and incomplete fusion defects were observed. At the end of the preliminary study, the values of welding voltage were set as 24 V, 28 V, and 32 V. The gas flow rates were set as 10 L/min, 14 L/min, and 18 L/min. The values of wire feed rate were set as 4.5 m/min, 7 m/min, and 9.5 m/min. The travel speed values were selected as 160 mm/min, 190 mm/ and 220 mm/min. The optimum welding parameters were observed that the voltage of 32 V, travel speed of 160 mm/min, wire feed rate of 4.5 m/min, and gas flow rate of 10 L/min. Wire feed speed, then voltage and travel speed were found as effective parameters, respectively. Gas flow rate was the least influential parameter [30].

P. Sathiya et al. focused on parameter optimization in gas metal arc welding of super austenitic AISI 904 L stainless steel sheet with 5 mm thickness. Electrode wire with a diameter of 1.2 mm was used. In the study, it was tried to minimize the weld bead width and height and to maximize the penetration depth by using genetic algorithm. The values of welding voltage were set between 28 V, and 32 V. The gas flow rates were set between 12 L/min and 16 L/min. The values of wire feed rate were set between 1.5 m/min and 2 m/min. The travel speed values were selected between 90 mm/ and 110 mm/min. The optimum welding parameters were observed that the voltage of 28 V, travel speed of 95 mm/min, wire feed rate of 2 m/min, and gas flow rate of 13 L/min. The welding current is directly proportional to the wire feed speed. According to the obtained experiment results, high wire feed rate and lower voltage have important effect for maximizing the depth of penetration and minimizing the bead width [31].

Sudhir Kumar et al. investigated the effect of process parameters such as welding current, voltage, and preheating temperature. The welded samples were examined using X-ray radiographic tests. In the study, AISI 1018 steel with a 12 mm thickness and ER70S-6 electrode wire with a diameter of 0.8 mm were used as base material and weld electrode, respectively. The values of welding voltage were set as 25 V, 30 V, and 35 V. The values of current were set as 75 A, 100 A, and 120 A. The values of preheat temperatures were selected as 275ºC, 285ºC, and 300ºC. The optimum welding parameters were observed that the voltage of 35 V, current of 120 A, and preheat temperature of 275ºC. UTS and the percent elongation of welds decrease with increasing preheat temperature but increases with increasing current. According to experimental results, preheating temperature was the most effective input parameter to achieve optimum ultimate tensile strength and percentage elongation of weldments, followed by welding current and voltage [32].

Nabendu Ghosh et al. investigated the effects of welding parameters on the maximum tensile strength. In the study, welding current, gas flow rate and nozzle to plate distance were selected as MIG welding parameters. AISI 409 ferritic stainless steel with a 3 mm thickness and AISI 316L austenitic filler wire with a diameter of 1.2 mm were used as base material and weld electrode, respectively. The values of current were set as 100 A, 112 A, and 124 A. The values of gas flow rate were selected as 10 L/min, 15 L/min, and 20 L/min. The values of nozzle to plate distances were set as 9 mm, 12 mm, and 15 mm. The optimum welding parameters were observed that the current of 124 A, gas flow rate of 10 L/min, and nozzle to plate distance of 9 mm. According to results of UTS experiments, it has been observed that the welding current has more effect than the parameters used in the experiment, and the next effective parameter is the gas flow rate. It was observed that the distance from the nozzle to the plate had the least effect. According to results of percentage elongation, it has been observed that gas flow rate has more effect than the parameters used in the experiment, and the next effective parameter is welding current. It was observed that the distance from the nozzle to plate had the least effect [33].

Zong-Liang Liang et al. performed a study on the MOORA (Multi-Objective Optimization Method by Ratio Analysis) based Taguchi method for optimization in automatic GMAW welding process.

In the study, weld bead geometry and hardness were examined. It was aimed that minimizing the bead width and height and maximizing the hardness. The values of current were set as 135 A, 165 A, and 195 A. The values of voltage were selected as 18 V, 23 V, and 28 V. The values of contact tip to work distance were set as 12 mm, 15 mm, and 18 mm. The values of welding speeds were set as 400 mm/min, 600 mm/min, and 800 mm/min. The optimum welding parameters were observed that the current of 135 A, voltage of 18 V, contact tip to work distance of 18 mm, and welding speed of 800 mm/min [34].

H. Ates et al. performed an Artificial Neural Network (ANN)-based study for the prediction of material properties after gas metal arc welding. In the study, S355J2+N steel with 15 mm thickness and electrode wire with a diameter of 1.2 mm were used. In the experiment, the current of 180 A, voltage of 28 V, and gas flow rate of 13 L/min were used as welding parameters. In the experimental study, the input parameters in the welding process were selected as various shielding gas mixtures of Ar, O_2 and CO_2. Mechanical properties such as tensile strength, impact test, elongation and weld metal hardness were investigated. In the experimental study, it has been understood that the amount of heat input and the gas mixture ratio play an important role in the samples in the case of elongation. The experimental results showed that some predictive values were consistent with the experimental data, while others had relatively higher errors. It can be argued that ANN algorithm will be most useful in estimation of yield strengths according to the experimental results and results of ANN estimations. Therefore, this method can be used to estimate yield strength and elongation values, especially when shielding gas ratios are determined before welding [35].

S. Kim et al. examined the mathematical model of weld bead penetration. In the experimental study, AS 1204 low carbon steel with 12 mm thickness and electrode wires with the diameters of 0.9, 1.2 and 1.6 mm were used. The values of current for electrode with a diameter of 0.9 mm were set as 90 A, 190 A, and 250 A. The values

of current for electrode with the diameters of 1.2 mm and 1.6 mm were set as 180 A, 260 A, and 360 A. The values of voltage were selected as 20 V, 25 V, and 30 V. The values of gas flow rate were set as 6 L/min, 10 L/min, and 14 L/min. The values of welding speeds were set as 250 mm/min, 330 mm/min, and 410 mm/min. According to the test results, it was found that weld bead penetration increased as wire diameter, welding current and welding voltage increased, while increase in welding speed decreased weld bead penetration. The gas flow rate does not have a significant effect on weld bead penetration [36].

Aim of Study

St37-2 and St52-3 steels are widely used today. However, there are a limited number of studies in the literature on the optimization of welding parameters of these steels which are joined by the GMAW method. In addition, there are almost no studies in the literature on the interpretation of the results with a holistic approach by applying the optimization process with more than one criterion and then the tempering process. It is known from the literature that welding parameters affect the mechanical and microstructural properties of welded structures. In this study, it is aimed to join 10 mm thick St37-2 and St52-3 steel materials via GMAW to clarify optimum welding conditions in terms of mechanical and microstructural properties. Tempering processes are applied to welded joints to increase mechanical strength by reducing residual stresses. Therefore, it is also aimed to determine the ideal tempering temperature by examining the effect of the tempering process on the mechanical properties and microstructure.

CHAPTER 3

EXPERIMENTAL WORK

In this chapter, working principle, advantages, limitations and effective factors of GMAW are presented. Then, Taguchi method and material and methods used in experimental work are also presented in this section.

3.1 Working Principle of GMAW

GMAW is an arc welding process. In this method, the arc occurs between the consumable electrode and the metal to be welded. In this process, the arc occurs under a shielding gas atmosphere such as Argon, Helium, CO, or various gas mixtures. The most important advantage of welding with this method is that the place to be welded is protected by certain gases during welding and thus it is not affected by the air and other factors. The choice of gases and gas mixtures depends on the metal being welded and other factors.

Since the area to be welded is protected by a gaseous environment from the negative effects of air, this method is called "Gas arc welding method". The electrode wire is fed continuously and automatically from a spool through the welding gun, as shown in Figure 3.1. The wire electrode melts to form the weld metal.

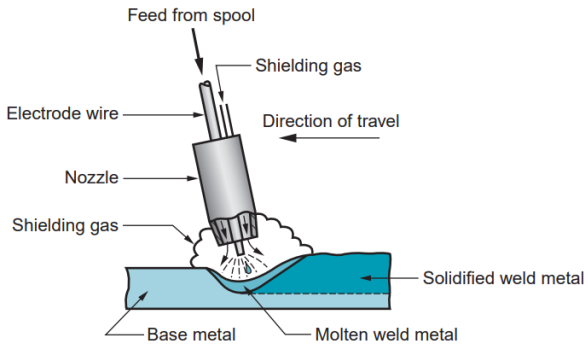

Figure 3.1 Gas metal arc welding (GMAW) [37]

In GMAW, the heat required for welding is produced by a melting and continuously fed wire electrode, through the arc formed between the workpiece and by heating the welding current passing through the electrode with the resistance created on the electrode. Wire diameters ranging from 0.8 to 6.5 mm (1/32–1/4 inch) are generally used in GMAW. The size of the electrode wire used depends on the thickness of the parts to be joined and the desired deposition rate.

The combination of electrode wire and shielding gases eliminates the slag coating on the weld seam, thus eliminating the need for manual grinding and cleaning of the slag. The GMAW process is therefore ideal for performing multiple welds passes on the same joint [37].

There are three types of Gas metal arc welding. The types of these welding are MIG (Metal Inert Gas) and TIG (Tungsten Inert Gas) and MAG (Metal Active Gas). The gases used in MIG welding method are inert gases and are protected by Helium and Argon gases. It is not generally used for steel.

The gases used in MAG welding method are CO_2 and mixed gases. It is used in steel, low carbon steel or alloy steel. In MIG and MAG welding, there is no need to change electrodes as in electric arc welding. The need for electrodes is provided by the welding wire, which is constantly driven into the welding area by the welding machine.

TIG welding is also a type of GMAW. It is different from MIG-MAG welding in terms of method. The additional wire is supplied by hand, as in the oxygen welding. The additional wire that creates the arc is tungsten. Since tungsten has a high melting point, it is also classified as a non-melting electrode.

3.2 Advantages of GMAW

There are many advantages of the GMAW method. It has eliminated the problem of using limited length electrodes encountered in electric arc welding. Metal deposition rate compared to electric arc welding is quite high. Due to the continuous electrode feeding and high metal deposition rate, welding speeds are higher compared to electric arc welding. Long weld seams can be drawn without stopping due to the continuous feeding of the electrode. These advantages have made the gas metal arc welding

method especially suitable for high production speeds and automatic welding applications [38].

3.3 Limitations of GMAW

As with other welding methods, there are some limitations that make it difficult to use GMAW [38]. Welding equipment is more complex, more expensive, and more difficult to move from one place to another than electric arc welding. The welding arc must be protected from air currents that remove the shielding gas from its location. Therefore, it is not possible to use the method in open areas unless the area around the welding area is protected against air flow. Due to the relatively high heat dissipation and arc density during operation, some welders may avoid using this method.

3.4 Effective Factors in GMAW

There are many welding variables that affect weld penetration, seam geometry and overall weld quality. Some of them are welding current (electrode feed rate), polarization, arc voltage (arc length), welding speed, free electrode length, electrode angles, welding positions, shielding gases, and diameter of electrode wire.

To obtain weld seams with sufficient quality, it is necessary to understand the effects of these variables and to control them. These variables are not independent of each other. Changing one requires changing the others or more of them to achieve the desired result. Considerable skill and experience are required to select the most appropriate settings in each application.

3.5 Taguchi Method

Taguchi method is a statistical method developed by Genichi Taguchi. The Taguchi method is used in many fields such as product manufacturing, biotechnology, marketing, and advertising. According to the Taguchi method, quality control design is more important than the production process. In this context, it is aimed to eliminate the variances in production before they occur. By using the Taguchi method, it is possible to determine which factors are important with a reduced number of

experimental runs. This saves the time and resources needed to determine the most appropriate factors and levels.

3.5.1 Design of Experiment

The traditional design of experiments was developed in the 1920s by Ronald A. Fisher of England for the rationalization of agricultural experiments. This approach was later applied in medical and biological studies as well.

Design of experiments means for finding the relationship between various factors (variables) and responses to them. Therefore, expressing their relationship precisely and efficiently by an equation is important. If the interactions between variables (factors) are important, it is important to include the interaction terms in the equation.

There are two main areas in quality engineering, offline and online quality engineering. The first is about technology development. The second is applied in daily production activities for process control or management. In offline quality engineering, there are three basic steps as system selection, parameter design, and tolerance design.

Selection of a system is a task for engineers working in a specific engineering field. Parameter design, on the other hand, is to improve the function of a product by changing parameter levels in a system.

The signal to noise (S/N) ratio expresses and evaluates the function of a system. Many design variables are listed and assigned to an orthogonal array.

Tolerance design is to assign the noise factors affecting the variability to an orthogonal array and examine the effects of each noise factor. Elimination of noise factors by upgrading components or raw materials is determined the using the loss function. Noise factors are uncontrollable factors that affect the processing result, where the derived response is known as the signal.

Variations are generally of three types, namely "lower is better", "higher is better" and "nominal is better" [39]. S/N ratios are calculated for each control factor to evaluate the effect of each selected factor on responses. S/N ratio calculations (see Eq 1.1a-c) are shown in the Table 3.1.

Table 3.1 S/N ratio equations [40]

Variations	S/N formula	Desired y value	Equation
Higher is better	S/N Ratio = - 10 log $\frac{1}{N}\sum_{i=1}^{N}\frac{1}{y_i^2}$	Limitless	1.1 a
Lower is better	S/N Ratio = - 10 log $\frac{1}{N}\sum_{i=1}^{N} y_i^2$	Zero	1.1 b
Nominal is better	S/N Ratio = 10 log $\sum_{i=1}^{N}\frac{y^{-2}}{S^2}$	Target Value	1.1 c

The main difference between traditional design of experiments and the design of experiments for quality engineering is that the SN ratio is used as an index for functionality rather than using a response. There is no distinction between control factors and noise factors in traditional design of experiments. The error is considered to change randomly, and its distribution is discussed. However, neither random error nor distribution is considered in quality engineering [41].

3.5.2 Orthogonal Array

Orthogonal arrays are a series of tables of numbers, each of which can be used to organize experiments for a range of experimental situations. Orthogonal arrays are denoted by the L notation with a subscript or hyphen (L9 or L-9). For example, an L9 will have nine rows, an L-n will have n rows. In addition to character notation, arrays contain some numerical notations that show the number of factors involved and the full factorial combinations. The designation of 2^3 with L-4 has these meanings. For example, 2^3 shows that the number of possible combinations is eight. Since the number of factors for which an experiment can be designed depends on the number of columns in the array, the 3 exponents in 2^3 also denotes the number of columns in the array [39].

There are many orthogonal arrays. The orthogonal arrays of the two-level series are as L4 (2^3), L8 (2^7), L12 (2^{11}), L16 (2^{15}) or L32 (2^{31}). The orthogonal arrays of the three-level series are as L9 (3^4), L27 (3^{13}), or L81 (3^{40}). The orthogonal arrays of the mixed

level series are as L18 (2 x 3^7) or L36 (2^3 x 3^{13}). The use of arrays such as L12, L18, and L36 is recommended in quality engineering because the interactions are distributed almost evenly to other columns, and there is no concern that an interaction confounds with a particular column or columns, thus causing confusion [41].

3.5.3 Gray Relational Optimization

Gray relational analysis (GRA) was developed by Deng Julong of Huazhong University of Science and Technology [42]. GRA is one of the most widely used models of gray system theory. Gray system means a system in which some of the information is known and some of the information is not. GRA defines situations with no information as black, and states with perfect information as white. In fact, states between these extremes with partial information are described as gray, hazy, or blurry. A variant of the GRA model, the Taguchi-based GRA model is a popular optimization method in many areas such as manufacturing engineering.

Gray relationship analysis is a quantitative and systematic approach and is most used in solving complex systems [43]. The GRA method can be used effectively in multi-criteria problems and when they have a complex relationship between criteria [44]. It can also be used effectively to determine the optimum process parameter that affects two or more response variables [45]. Multi-criteria problems can be handled effectively using Gray Relationship analysis [46].

In the gray system theory, if the points in the series are desired to be small values, the points with small values take values close to "1" in linear normalization, while the points with large values take values close to "0" [47]. In the gray system theory, the higher is better, the normalization is calculated by using Eq. 1.2.

$$x_i^* \text{ (k)} = \frac{x_i^0 (k) - \min x_i^0(k)}{\max x_i^0(k) - \min x_i^0(k)} \quad \textbf{(1.2)}$$

In the case of “lower is better”, the normalization is calculated by using Eq. 1.3.

$$x_i^* \text{ (k)} = \frac{\max x_i^0(k) - x_i^0(k)}{\max x_i^0(k) - \min x_i^0(k)} \quad \textbf{(1.3)}$$

The deviation sequence values are calculated using Eq. 1.4.

$$\Delta_{0i}(k) = \left| x_0(k) - x_i(k) \right| \quad \textbf{(1.4)}$$

The Gray Relational Coefficient (GRC) to express the relationship between the real and ideal normalized experimental results is calculated by using Eq. 1.5.

$$\zeta_i(k) = \frac{\Delta_{min} + \zeta\Delta_{max}}{\Delta_{oi}(k) + \zeta\Delta_{max}} \quad \textbf{(1.5)}$$

ζ is distinctive coefficient and it is usually in the range of $0 < \zeta < 1$. In this study, considering the engineering approach and other studies, the ζ value was determined as 0.5 [48-52]. Finally, the Gray Relational degree is found by the following Eq. 1.6.

$$a_n = \frac{1}{n}\sum_{i=1}^{n} Y_i(k) \quad \textbf{(1.6)}$$

All results of the relevant experimental parameter are evaluated on the same scale with this value. The parameter with the highest value is determined as optimum. Degrees close to this value represent acceptable parameters [53].

3.6 Materials and Methods

St37-2 and St52 low alloy steel materials were joined by GMAW method using different current, voltage, and welding speed parameters. Tensile test, impact test, and hardness test were applied to the welded samples. Optimum welding parameters were determined by using mechanical test results and Taguchi optimization method. Then, three new samples were joined using the optimum welding parameters which were obtained according to the results of Taguchi analysis. These samples were exposed to three different temper temperatures and the effect of temperature on mechanical properties was examined. The procedures carried out within the scope of the experiment method are explained in the following sections.

3.6.1 Material Properties

Within the scope of the thesis study, the joining of steel materials with different alloy properties by GMAW was investigated. St37-2 and St52-3 alloy steels with a thickness

of 10 mm were used as the base material. The chemical properties of the ST37-2 and St52-3 alloy steels to be used in the experimental study are shown in Table 3.2.

Table 3.2 Chemical composition of low carbon steel ST37-2 and ST52-3 according to DIN 17100

	Chemical Composition, %, ≤					
Steel Grade	C max	Si max	Mn max	P max	S max	Thickness (d) (mm)
St37-2	0.17 0.20	--	1.40	0.045	0.045	≤ 16 mm
St52-3	0.20 0.22	0.55	1.60	0.040	0.040	≤ 30 mm

The tensile strength of the St37-2 alloy steel ranges between 360 and 460 MPa, yields at 235 MPa with a minimum elongation of 25% [9]. The tensile strength of the St52-3 alloy steel ranges between 490 and 630 MPa, yields at 355 MPa with a minimum elongation of 22%.

The SG2 electrode wire with a diameter of 1.0 mm was used as welding electrode. The chemical and mechanical properties of the electrode wire to be used in the experimental study are shown in Table 3.3 and 3.4, respectively.

Table 3.3 Chemical composition of SG2 electrode wire

	C	Si	Mn	P	S	Cu
Chemical Composition (%)	0.06-0.15	0.80-1.15	1.40-1.85	≤ 0.025	≤ 0.035	≤ 0.50

Table 3.4 Mechanical properties of SG2 electrode wire

Model	Yield Strength (Mpa)	Tensile Strength (Mpa)	Elongation (%)
ER70S-6	≥ 420	≥ 500	≥ 22

3.6.2 Welding Operations

St37-2 and St52-3 alloy steels were joined by using GMAW process. The mixed gas was used as shielding gas in welding process. BUĞRA MIG 550 SW welding machine was used as welding machine. The picture and technical specifications of the welding machine are shown in Figure 3.2 and Table 3.5, respectively.

Figure 3.2 The welding machine (BUĞRA MIG 550 SW)

Table 3.5 The technical specifications of the BUĞRA MIG 550 SW

Input power	3 X 380V
Max. installed power	25,4 KVA
No load voltage	21 – 48 V
Adjustment positions	30
Welding current	40 - 550 A
Duty cycle	% 60 – 550 A
Wire speed	1 - 22
Suitable wire diameter	0,8 – 1,0 – 1,2 – 1,6 mm
Protection class	IP21
Cooling	F
Dimensions	460 X 1360 X 980 mm
Weight	214 kg

Single V butt weld was used in welding processes of St37-2 and St52-3 dissimilar steel materials. The weld groove angle is 60º, the root face is 2 mm. Materials were machined to these dimensions and machined materials can be seen are in Figure 3.3.

Figure 3.3 The machined material to obtain groove angle of 60º and root face of 2 mm

In the experimental study, welding current, voltage and welding speed were investigated as GMAW parameters. The welding parameters and experimental factors used in the experimental study were given in Table 3.6. The layout of the samples in the materials joined with GMAW is shown in Figure 3.4.

Table 3.6 Welding parameters and their levels used in the orthogonal array matrix

Symbol	Factor	Unit	Level 1	Level 2	Level 3
A	Voltage	Volt	25	30	35
B	Current	Ampere	250	290	330
C	Welding Speed	mm/min	200	250	350

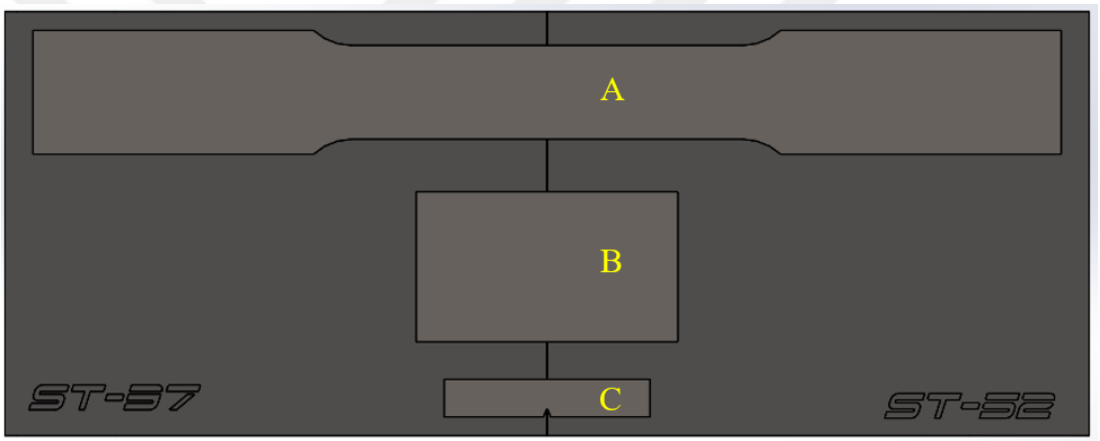

Figure 3.4 The layout of the samples in the materials joined with GMAW; (A) Tensile test specimen, (B) Specimen for hardness test and microstructural examination, (C) Impact test specimen

3.6.3 Taguchi Experimental Design

Taguchi orthogonal array was used to minimize the number of experiments to be performed. In this context, the L9 orthogonal array, which consists of nine different experiments applied, as shown in Table 3.7.

Table 3.7 Taguchi L9 Orthogonal Array

Experiment Number	Voltage (A)	Current (B)	Welding Speed (C)
1	1	1	1
2	1	2	2
3	1	3	3
4	2	1	2
5	2	2	3
6	2	3	1
7	3	1	3
8	3	2	1
9	3	3	2

Optimum values were determined by using parameters as levels and mechanical properties as noise data. Welding current, welding voltage and welding speed were determined as variable parameters. The yield and rupture points, hardness values and impact test results obtained because of the tensile test were used to determine the signal/noise ratios. Minitab software was used to perform the Taguchi method.

3.6.4 Mechanical Tests

Mechanical properties such as impact energy, tensile strength, breaking point, fracture toughness was examined in detail. Tensile and impact tests were applied to the welded samples in accordance with international standards. After the welding process was completed, rough cutting process of the specimens of tensile, hardness and Charpy impact tests were performed with a band saw which is the brand of Cuteral. The rough cutting process is shown in Figure 3.5. Then, tensile, and v-notch impact tests were performed according to the boundary conditions as explained below sections.

Figure 3.5 The rough cutting process

3.6.4.1 V-Notch Charpy Impact Test

Charpy impact test specimen dimensions are given in Figure 3.6. The V-notch specimen has an angle of 45°, a depth of 2 mm, and a root radius of 0.25 mm.

To perform Charpy impact test according to the ASTM A370 standard, Charpy impact samples with dimensions of 7.5 x 10 x 55 (mm) were prepared from 12 different materials.

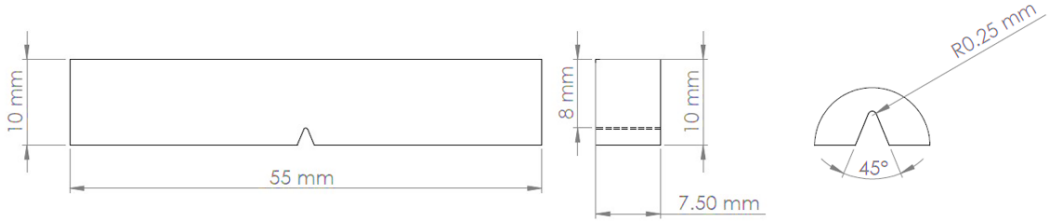

Figure 3.6 Charpy impact test specimen dimensions

The specimens were machined on the VMC 850E type CNC machine. In Figure 3.7 machining of V-notch can be seen where notch was machined with a specific notch tool after precision machining.

Figure 3.7 Machining of notch

The Charpy impact tests were carried out at 25°C in a pendulum device with a capacity of 300 J. The Charpy impact tester is shown in Figure 3.8.

Figure 3.8 Charpy impact tester

3.6.4.2 Tensile Test

For the tensile test, welded samples were machined to the dimensions specified in TSE EN ISO 6892-1 via CNC machine as shown in Figure 3.9.

Figure 3.9 Cutting process of tensile test specimen

The tensile tests were carried out on a 250 kN capacity, tensile tester of Zwick Roell Z250 with high precision and strength. Tensile test device can be seen in Figure 3.10.

Figure 3.10 Tensile test device

3.6.4.3 Hardness Test

In the hardness and metallographic examination, the samples which have the dimensions of 40 x 70 x 10 mm were used. Hardness traverse was carried out at 1 mm intervals at different determined points as shown in Figure 3.11. For this purpose, the samples were ground by using sandpapers with a grit number of 200, 400, 600, 800, 1000 and 1200, respectively. Afterwards, the samples were polished with 3μ and 1μ diamond polishers, respectively, with a Presi polishing device, as shown in Figure 3.12.

Figure 3.11 Specimen for hardness test

Figure 3.12 Presi polishing device

Then, a hardness test was carried out with a Shimadzu HMV-G, Vickers hardness tester as seen in Figure 3.13. The hardness value was calculated from the trace diagonals left by the diamond tip by the device software. The 300-gr load was applied up to 15 second on the specimens [54, 55].

Figure 3.13 Hardness test device

After applying tensile test, hardness test, and Charpy impact test to welded samples, parameter optimization was made according to the results of these tests. Optimum welding parameters were evaluated in line with the mechanical and microstructural analysis results. To verify the experimental result, a new sample was welded by using optimum welding parameters.

3.6.5 Tempering Processes

In order to examine the effect of temper temperature, three new samples were welded by using optimum welding parameters. To determine the temper temperature, studies in the literature were examined. A lightweight, laminated carbon steel/6061 aluminum composite was designed and manufactured utilizing the facile cold roll bonding procedure in the study by Amanollahi et al. Changes in the interfacial microstructure, mechanical characteristics, strain partitioning, and bonding strength of incorporated layers were examined using a variety of annealing treatments [56]. Adedayo et al. investigated the effects of annealing heat treatment on steel welds in their study [57]. The temper temperatures were determined by examining the used materials and temperature ranges used in these studies. The determined temper temperatures are given in Table 3.8.

In order to relieve the stresses after welding, three new samples were heated at 250 ℃, 350 ℃ and 450 ℃ for 2 hour and cooled in air. The effects of temper temperature were examined by applying tensile test, hardness test, Charpy impact test and microstructure

analysis to welded samples subjected to three different temper temperatures. Then, the ideal temper temperature was determined for the weld sample combined with the optimum welding parameters.

Table 3.8 Parameters which were used in the tempering process

Temperature (℃)	Cooling medium	Hold time (min)
250	Air	120
350	Air	120
450	Air	120

3.6.6 Microstructural Characterization

After sandpapering, polishing, and etching processes, microstructural characterizations were carried out to the samples. 40 x 70 x 10 mm sized specimens prepared for metallographic examination as shown in Figure 3.14. Since the samples are in sizes that can be easily held by hand, molding was not required.

Figure 3.14 Sample for microstructural examination

Samples were etched with 2% Nital for 15 seconds at room temperature [21, 58, 59]. Microstructure images of all etching samples were taken with Nikon optical microscope, which enables image recording with Clemex software integration. Images obtained at 50x, 100x, 200x, and 500x magnifications are presented in the results section.

CHAPTER 4

RESULTS and DISCUSSIONS

The results are presented in three parts. Firstly, mechanical test results are presented with tables and graphics, secondly, Taguchi and ANOVA analysis results and graphics are presented. Finally, multi criteria decision making for optimization via gray relational analysis presented in this section.

4.1 Mechanical Test Results

Within the scope of Taguchi optimization, impact test, tensile test, and hardness test were performed on nine samples joined with different welding parameters. Three new samples were then joined with the optimum parameters obtained via mechanical and microstructural analysis. In order to improve mechanical properties after welding, these three new samples were heated at 250 ℃, 350 ℃ and 450 ℃ for 2 hour and cooled in air.

4.1.1 Impact Test Results

Significant increases were observed in the impact energy compared to the base metals where all results are presented in Table 4.1.

Table 4.1 Impact test results

Experimental Set	Impact Energy (J)
1	42.55
2	66.95
3	84.66
4	133.6
5	59.41
6	139.21
7	137.73
8	79.56
9	171.72

The fracture regions of the samples are shown in Figure 4.1. Ductile rupture has occurred in the sample 6, 7, 8, and 9. Brittle fracture was observed in the sample 1, 2, 3, 4, and 5. The highest impact strength with a value of 171.72 Joule was obtained in the sample 9, which was welded at 35 V, 330 A, and 250 mm/min. The lowest impact strength with a value of 42.55 Joule was also obtained in the sample 1, which was welded at 25 V, 250 A, and 200 mm/min. The fracture regions of the sample 1 and 9 are shown in the Figure 4.2 and Figure 4.3, respectively.

When the fracture zones of the sample 1 and 9 were examined, it was observed that the porosities and the lack of penetration of the weld metal were observed in the fracture zone of the sample 1. Sample 1 was welded using the lowest current, voltage, and welding speed. Low current, voltage and welding speed values can lead to a lack

of penetration of the weld metal. When the rupture region of the sample 9 is examined, it is seen that a ductile rupture has occurred.

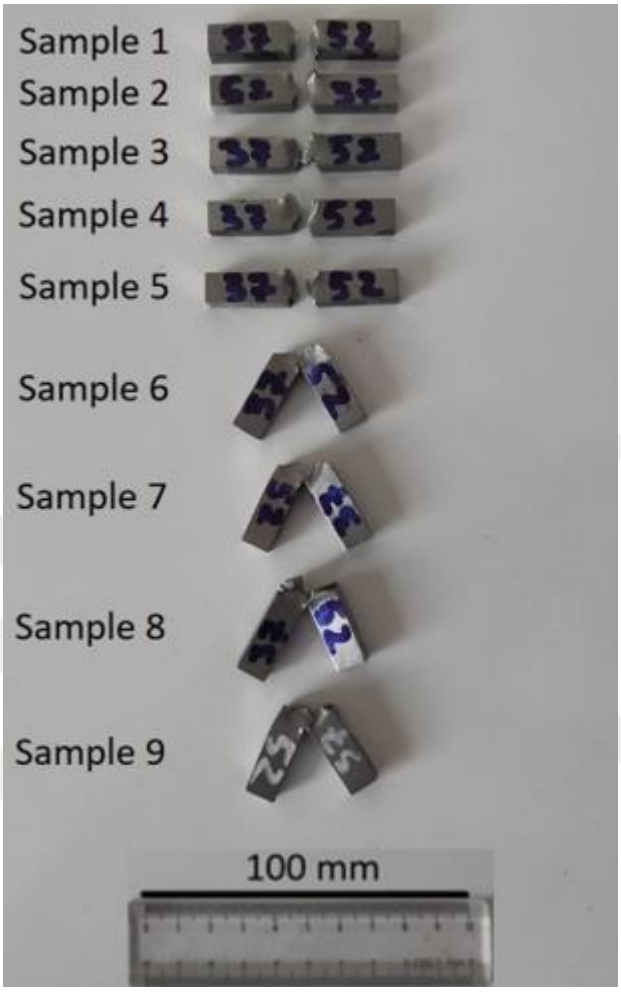

Figure 4.1 Fracture regions of the impact test samples

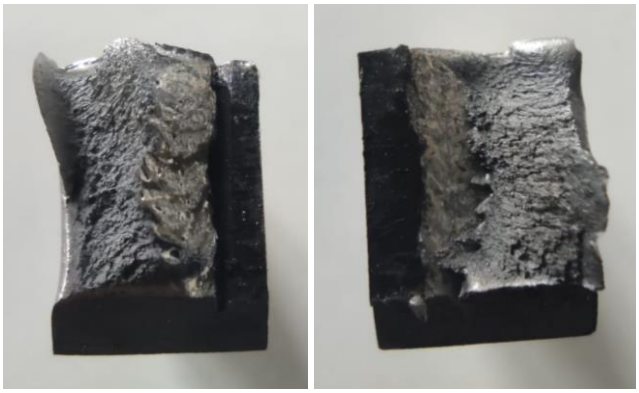

(a) (b)

Figure 4.2 Fracture regions of the impact test sample 1, (a) - St52-3, (b) – St37-2

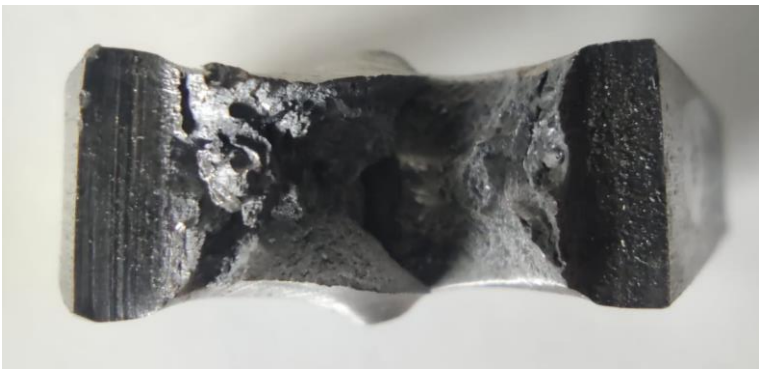

Figure 4.3 Fracture regions of the impact test sample 9

4.1.2 Tensile Test Results

Tensile test results are presented in Table 4.2. In this table, upper and lower yield points are shown as R_{eH} and R_{eL}, respectively. Stress at 0.2 % non-proportional elongation is shown as $R_{p0.2}$ in Table 4.2. The highest tensile strength with a value of 529 MPa was obtained in the A3B3C2 sample. In addition, the highest elongation with 17.5% was obtained in the A3B3C2 sample.

Table 4.2 Tensile test results

Experimental Set	Tensile Strength (MPa)	Yield Strength (MPa)	Elongation (%)
1	285	269 ($R_{p0.2}$)	1.7
2	457	391 (R_{eH}), 382 (R_{eL})	4.8
3	470	448 (R_{eH}), 441 (R_{eL})	2.8
4	403	376 ($R_{p0.2}$)	3.2
5	453	419 ($R_{p0.2}$)	3.3
6	519	395 (R_{eH}), 392 (R_{eL})	8.3
7	483	386 (R_{eH}), 379 ($_{ReL}$)	5.3
8	324	308 ($R_{p0.2}$)	2.1
9	529	375 (R_{eH}), 367 (R_{eL})	17.5

Stress-strain plots are given in three different groups according to the current values, see Figures 4.4, 4.5, and 4.6.

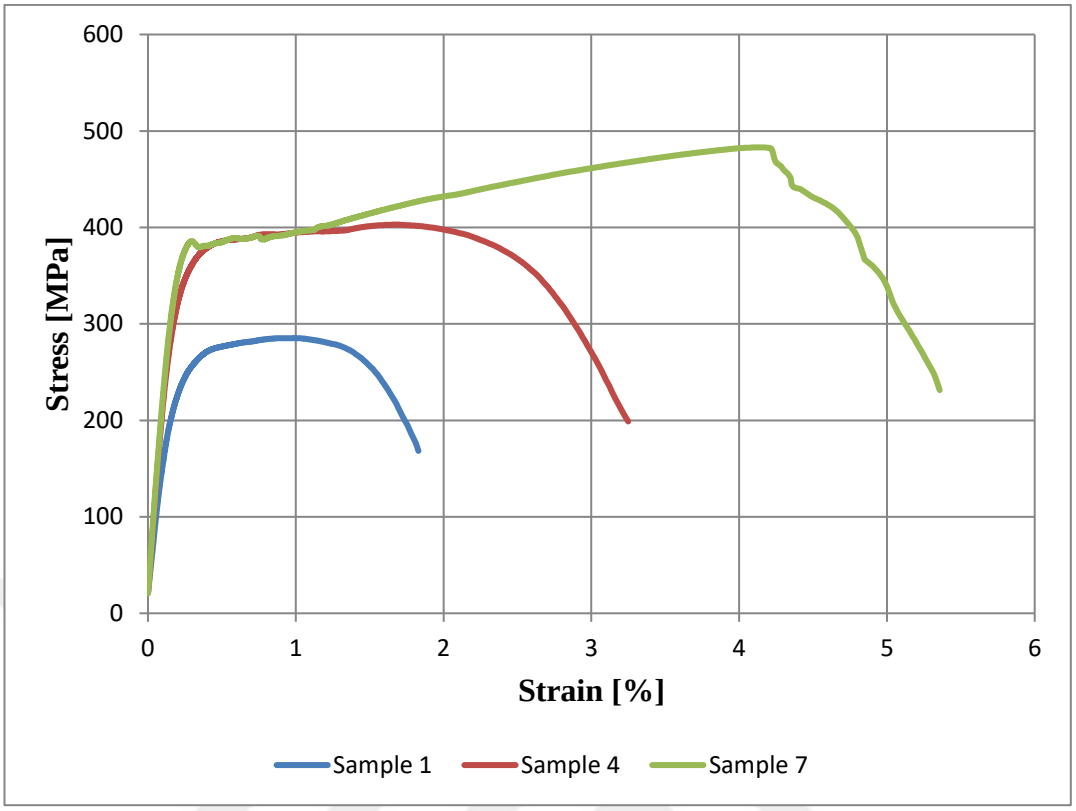

Figure 4.4 Stress-strain plot for current at 250 A [(1)-A1B1C1, (4) - A2B1C2), (7) - A3B1C3]

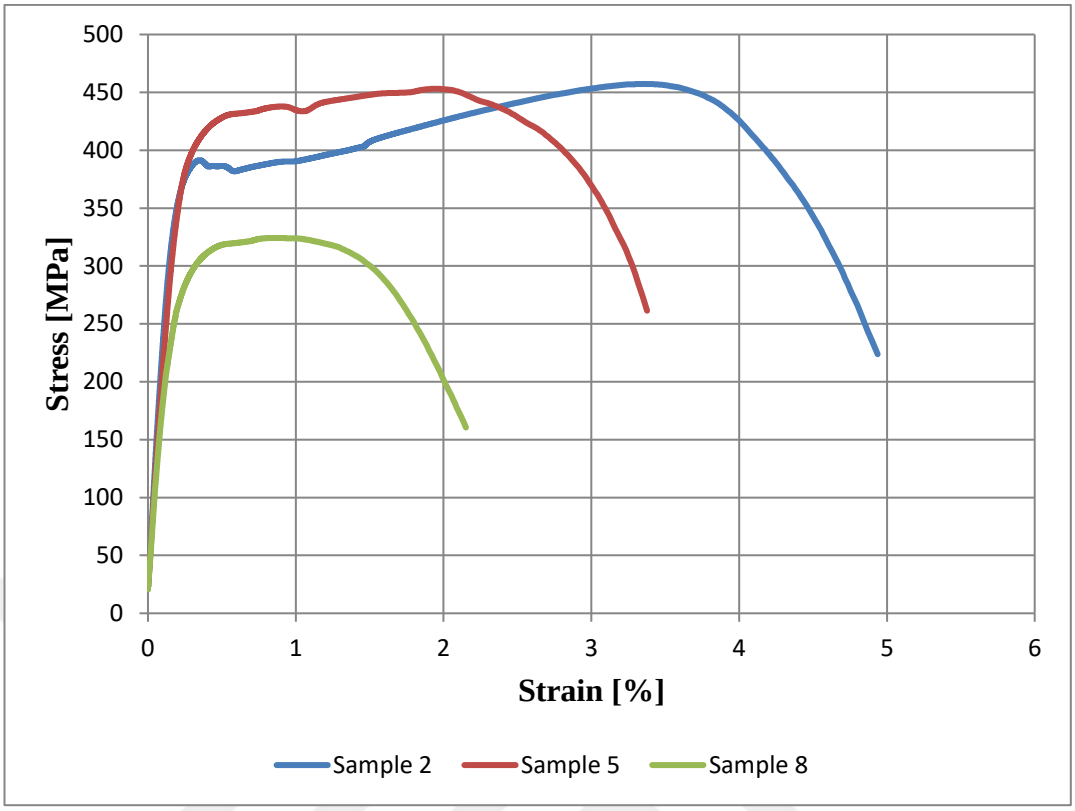

Figure 4.5 Stress-strain plot for current at 290 A [(2)-A1B2C2, (5) - A2B2C3), (8) - A3B2C1]

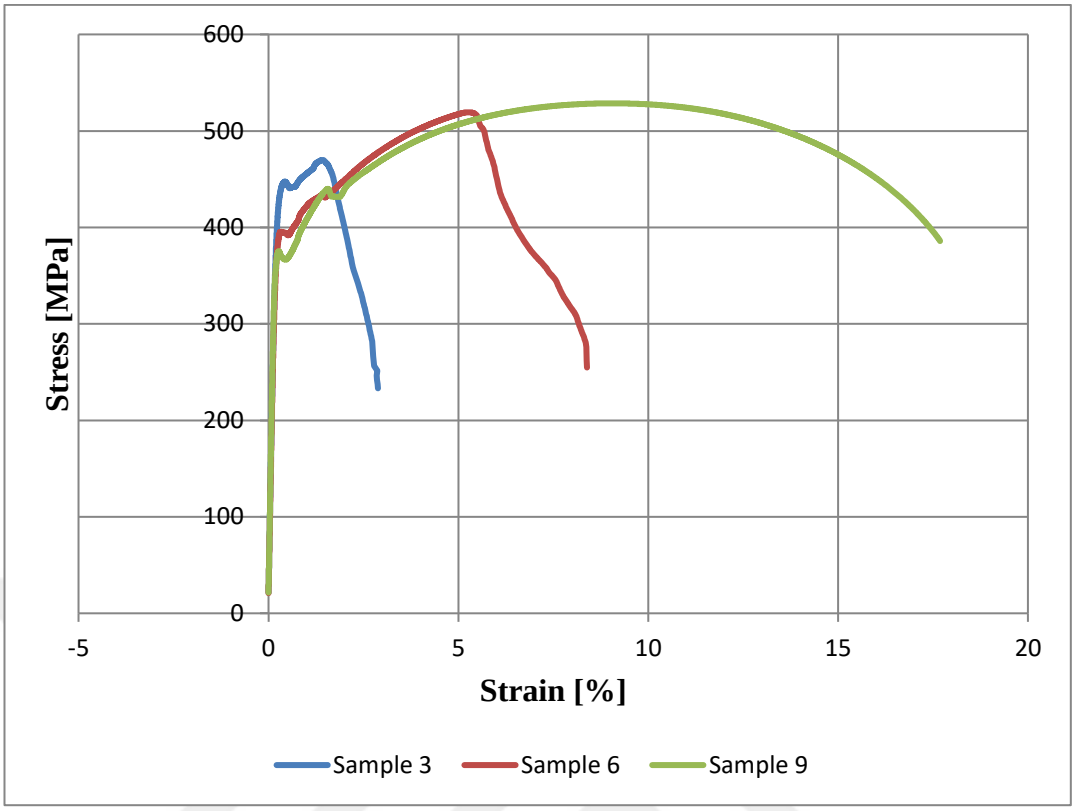

Figure 4.6 Stress-strain plot for current at 330 A [(3) -A1B3C3, (6) - A2B3C1), (9) - A3B3C2]

According to results, the highest values in terms of tensile strength and elongation were obtained in the sample 9, which was welded at 35V, 330A, and 250 mm/min. The lowest tensile strength and elongation were obtained in the sample 1, which was welded at 25V, 250A, and 200 mm/min.

The fracture regions of the tensile test samples are shown in Figure 4.7. It can be seen from this figure that the sample 9 has the highest elongation value. In the sample 9, fracture was occurred in the St52-3 base material.

The lowest tensile strength and elongation value were seen in the sample 1. The highest tensile strength and elongation value were seen in the sample 9. The fracture regions of the sample 1 and 9 are shown in the Figures 4.8 and 4.9, respectively. When the fracture zones of the sample 1 and 9 were examined, it was observed that the porosities and the lack of penetration of the weld metal were observed in the fracture zone of the sample 1. Sample 1 was welded using the lowest current, voltage, and welding speed. Low current, voltage and welding speed values can lead to a lack of penetration of the weld metal. When the rupture region of the sample 9 is examined, it is seen that a

ductile rupture has occurred. Breaking points of tensile test specimens are also shown in Figure 4.10.

Figure 4.7 Fracture regions of the tensile test samples

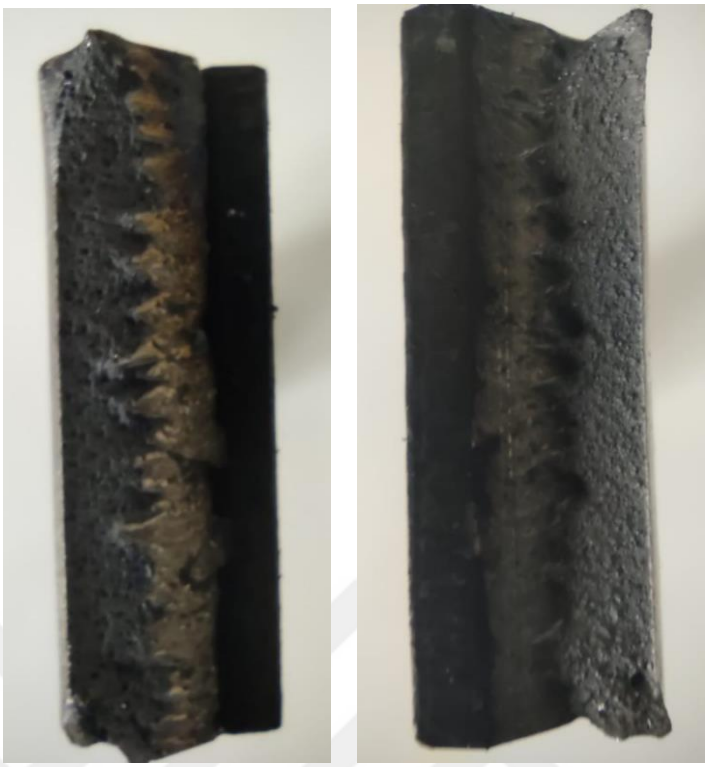

(a) (b)

Figure 4.8 Fracture regions of the tensile test sample 1, (a) - St52-3, (b) – St37-2

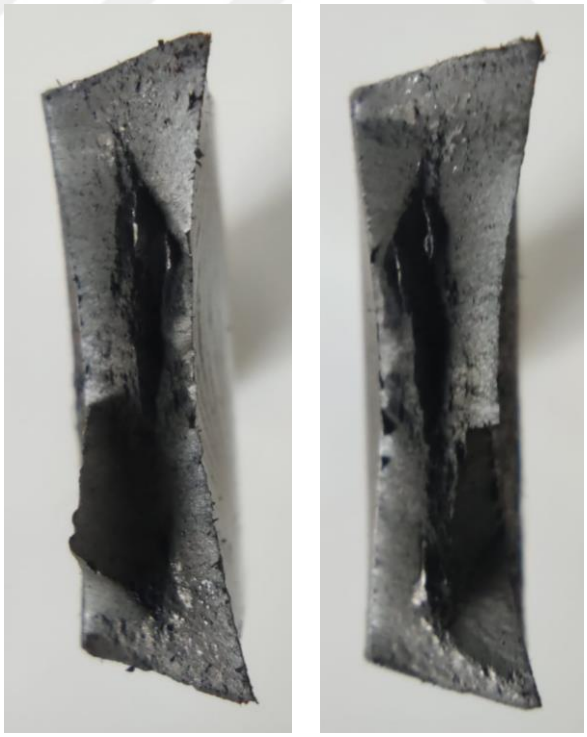

(a) (b)

Figure 4.9 Fracture regions of the tensile test sample 9, (a) - St52-3, (b) – St37-2

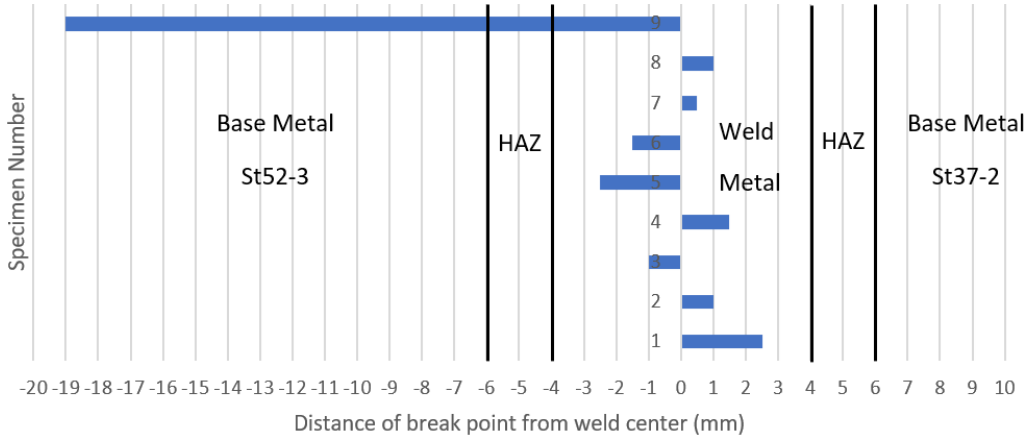

Figure 4.10 Breaking points of tensile test specimens

4.1.3 Hardness Test Results

According to the hardness test results which were presented in Table 4.3, significant increases were observed in the hardness values compared to the base metal.

Table 4.3 Hardness test results

Experimental Set	Hardness (HV)
1	225
2	219
3	230
4	235
5	239
6	222
7	224
8	228
9	215

Hardness distribution of weld metal, heat affected zone (HAZ) and base metal are given in 3 different groups according to the current values, see Figure 4.11, 4.12, and 4.13.

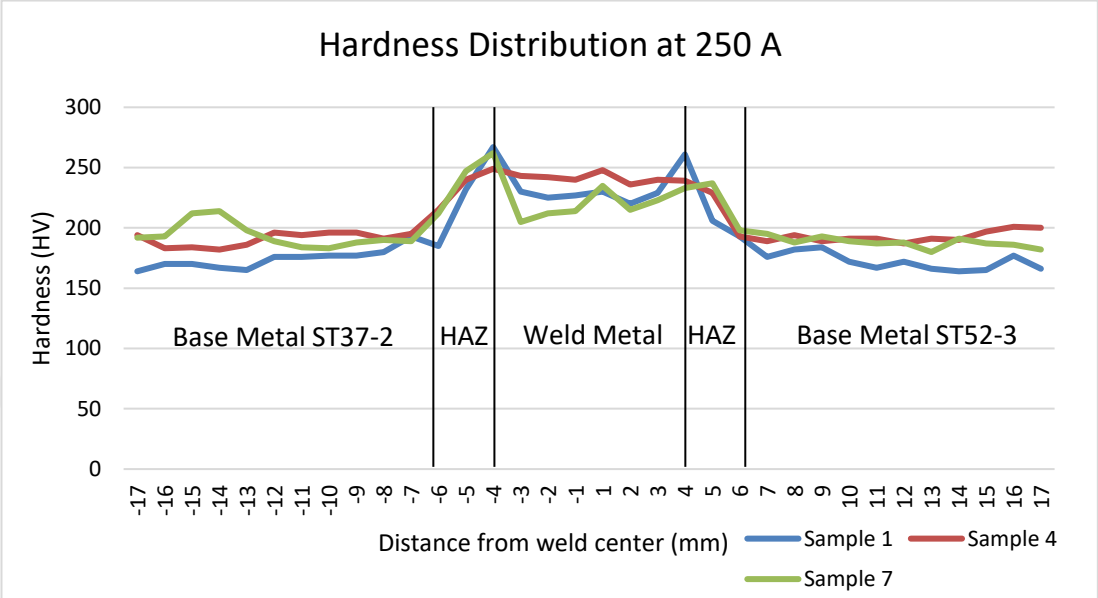

Figure 4.11 Hardness distribution at 250 A

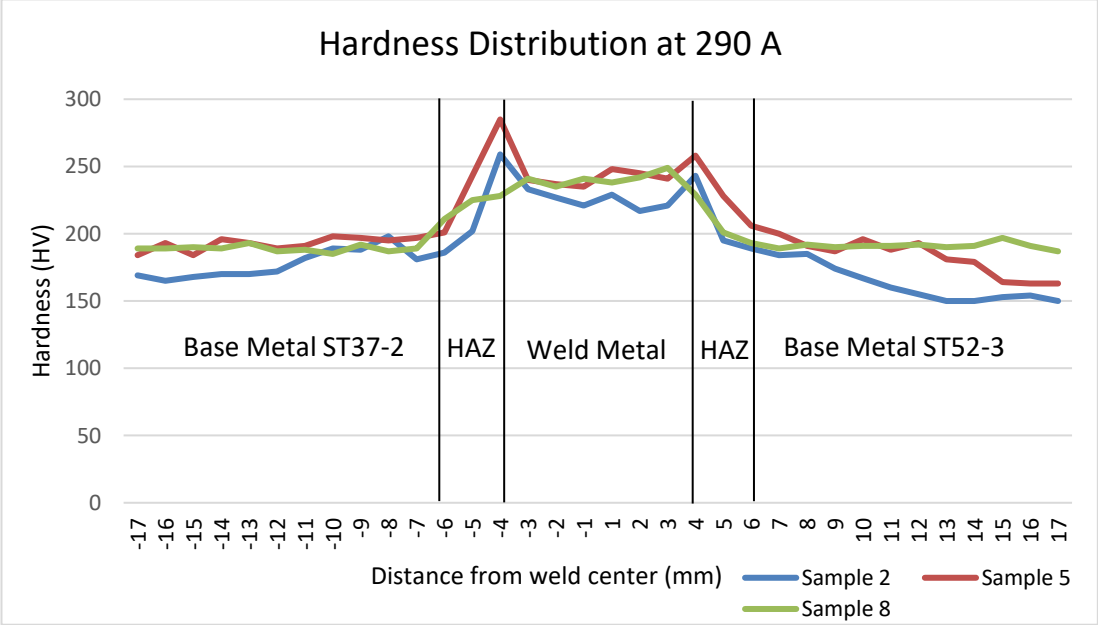

Figure 4.12 Hardness distribution at 290 A

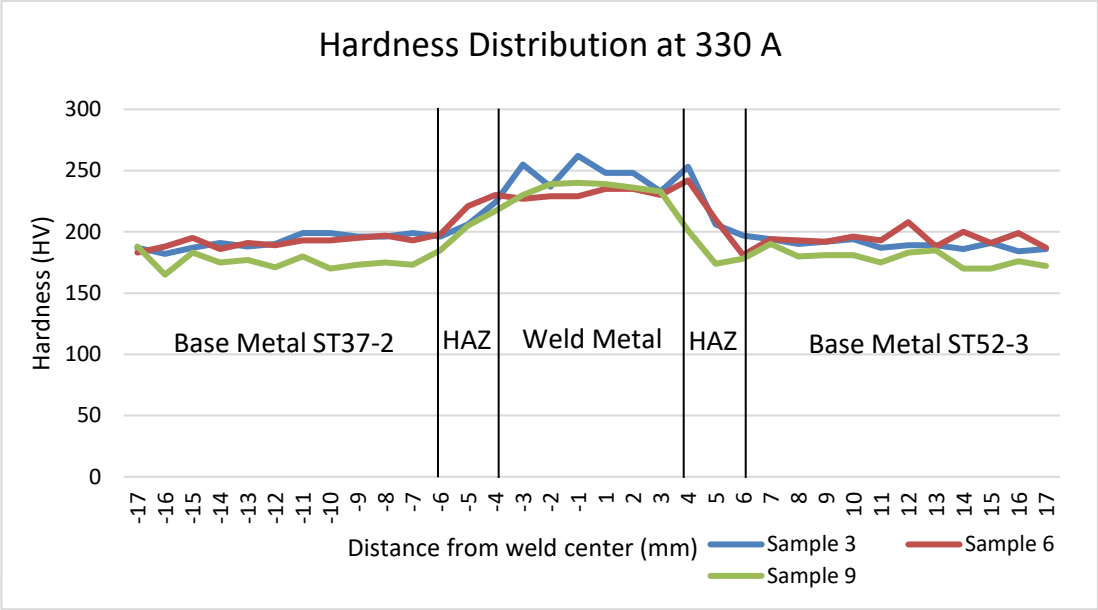

Figure 4.13 Hardness distribution at 330 A

4.2 Results of Taguchi Analysis

Optimization of the parameters which were in the Taguchi experimental design was carried out by using Minitab software. S/N ratios calculated using Equation 1.1a,b and other ANOVA terms were obtained with the help of this software. The 'Larger is better' approach was used in the design since the properties that must be high in the welded specimen were tested.

4.2.1 S/N Ratios

The total S/N ratios of each parameter in the experimental design are given in Table 4.4.

Table 4.4 Total S/N Ratios for parameters

Experimental Set	Variables	A	B	C	S/N for Impact Energy	S/N for Tensile Strength	S/N for Hardness
1	A1B1C1	1	1	1	32.58	49.10	47.06
2	A1B2C2	1	2	2	36.52	53.20	46.79
3	A1B3C3	1	3	3	38.55	53.44	47.25
4	A2B1C3	2	1	3	42.52	52.11	47.40
5	A2B2C2	2	2	2	35.48	53.12	47.56
6	A2B3C1	2	3	1	42.87	54.30	46.94
7	A3B1C3	3	1	3	42.78	53.68	47.02
8	A3B1C1	3	2	1	38.01	50.21	47.15
9	A3B3C2	3	3	2	44.70	54.47	46.64

A: Voltage, B: Current, C: Welding Speed

4.2.1.1 Impact Energy

S/N ratios of impact energy are given in table 4.5. As a result of the analysis, A3B3C2 was determined as the optimum parameters in terms of impact energy. The most influential factor for impact energy was found to be voltage, see Figure 4.14.

Table 4.5 Response Table for Signal to Noise Ratios of Impact Energy

Level	Voltage	Current	Welding Speed
1	35.88	39.29	37.82
2	40.29	36.67	41.24*
3	41.83*	42.04*	38.94
Rank	1	2	3

* Optimum level

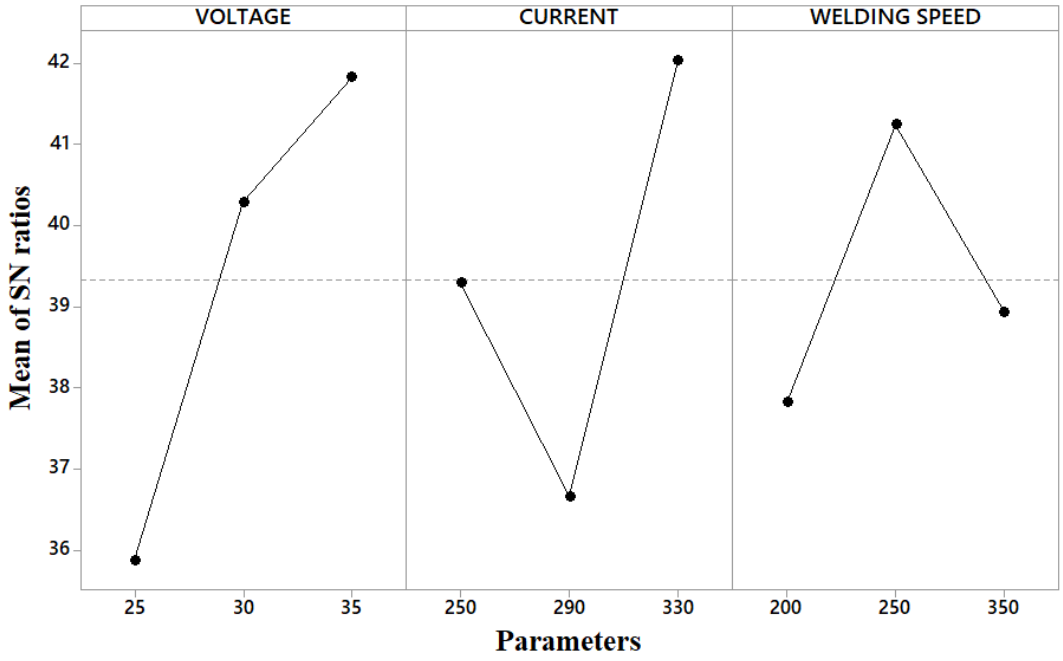

Figure 4.14 Main effects plot for S/N ratios of impact energy

4.2.1.2 Tensile Strength

S/N ratios of tensile strength are given in Table 4.6. As a result of the analysis, A2B3C3 was determined as the optimum parameters in terms of tensile strength. The most influential factor for tensile strength was found to be current, see Figure 4.15.

Table 4.6 Response Table for Signal to Noise Ratios of Tensile Strength

Level	Voltage	Current	Welding Speed
1	51.91	51.63	51.20
2	53.18*	52.18	53.26
3	52.79	54.07*	53.41*
Rank	3	1	2

* Optimum level

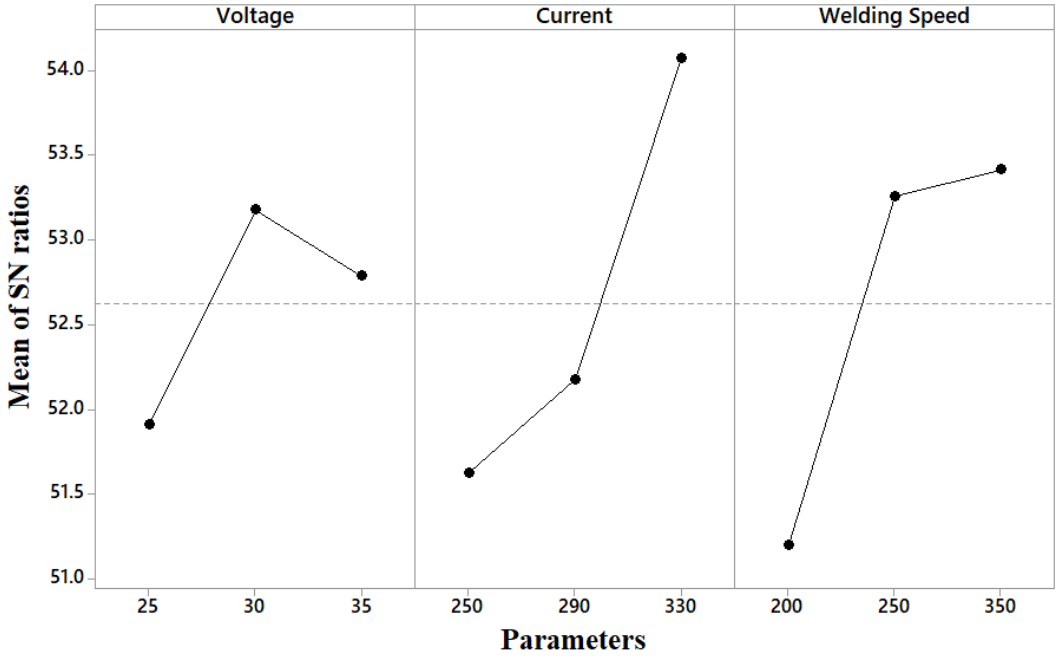

Figure 4.15 Main effects plot for S/N ratios of tensile strength

4.2.1.3 Hardness

S/N ratios of hardness are given in Table 4.7. As a result of the analysis, A2B2C3 was determined as the optimum parameters in terms of hardness. The most influential factor for hardness was found to be voltage, see Figure 4.16.

Table 4.7 Response Table for Signal to Noise Ratios of Hardness

Level	Voltage	Current	Welding Speed
1	47.03	47.16	47.05
2	47.30*	47.17*	46.94
3	46.94	46.94	47.28*
Rank	1	3	2

* Optimum level

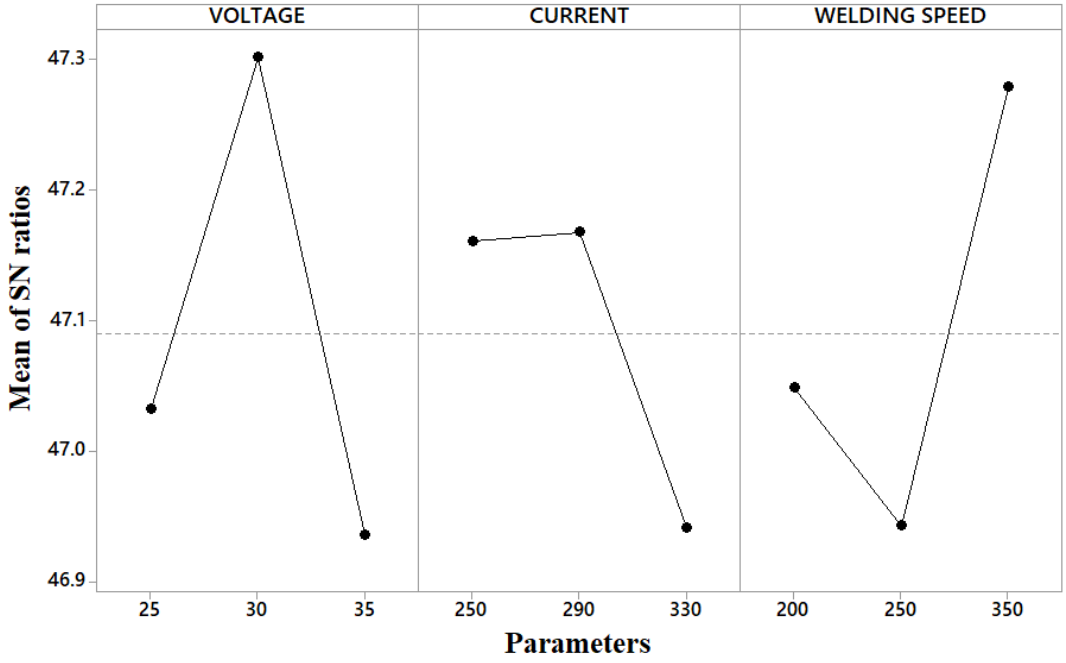

Figure 4.16 Main effects plot for S/N ratios of hardness

4.2.2 ANOVA

4.2.2.1 ANOVA for Impact Energy

ANOVA analysis results of impact energy are shown in Table 4.8. It was found that the most effective factor was voltage when the S/N ratios of the impact energy were examined. ANOVA analysis results also show that voltage has the highest contribution rate for impact energy with a contribution rate of 42.10%. Welding speed has the lowest contribution rate for impact energy with a contribution rate of 14.61%.

Table 4.8 ANOVA for Impact Energy

Parameters	DF	SS	Contribution	MS	F	P
Voltage	2	6694.7	42.10%	3347.3	7.89	0.112
Current	2	6034.1	37.95%	3017	7.11	0.123
Welding Speed	2	2323.8	14.61%	1161.9	2.74	0.267
Error	2	848.3	5.33%	424.1		
Total	8	15900.8	100%			

DF: Degree of freedom, SS: Sum of squares, MS: Mean square

4.2.2.2 ANOVA for Tensile Strength

ANOVA analysis results of tensile strength are shown in Table 4.9. It was found that the most effective factor was current when the S/N ratios of the tensile strength were examined. ANOVA analysis results also show that current has the highest contribution rate for tensile strength with a contribution rate of 40.63%. Voltage has the lowest contribution rate for tensile strength with a contribution rate of 8.61%.

Table 4.9 ANOVA for Tensile Strength

Parameters	**DF**	**SS**	**Contribution**	**MS**	**F**	**P**
Voltage	2	4830	8.61%	2415	0.39	0.718
Current	2	22782	40.63%	11391	1.86	0.35
Welding Speed	2	16188	28.87%	8094	1.32	0.431
Error	2	12268	21.88%	6134		
Total	8	56067	100%			

DF: Degree of freedom, SS: Sum of squares, MS: Mean square

4.2.2.3 ANOVA for Hardness

ANOVA analysis results of hardness are shown in Table 4.10. It was found that the most effective factor was voltage when the S/N ratios of the hardness were examined. ANOVA analysis results also show that voltage has the highest contribution rate for hardness with a contribution rate of 32.25%. Current has the lowest contribution rate for hardness with a contribution rate of 14.53%.

Table 4.10 ANOVA for Hardness

Parameters	**DF**	**SS**	**Contribution**	**MS**	**F**	**P**
Voltage	2	148.51	32.25%	74.25	1.18	0.459
Current	2	66.89	14.53%	33.45	0.53	0.653
Welding Speed	2	119.08	25.86%	59.54	0.94	0.514
Error	2	126.05	27.37%	63.02		
Total	8	460.53	100%			

DF: Degree of freedom, SS: Sum of squares, MS: Mean square

4.2.3 Prediction

Predicted values which are obtained by Taguchi analysis are given in Table 4.11.

Table 4.11 Predicted values

Experimental Set	Variables	A	B	C	Predicted Impact Energy	Predicted Tensile Strength	Predicted Hardness
1	A1B1C1	1	1	1	53.03	298.56	225.38
2	A1B2C2	1	2	2	54.03	406.56	223.10
3	A1B3C3	1	3	3	87.10	506.89	225.85
4	A2B1C3	2	1	3	136.04	439.89	229.94
5	A2B2C2	2	2	2	69.89	466.56	238.88
6	A2B3C1	2	3	1	126.29	468.56	226.85
7	A3B1C3	3	1	3	124.81	432.56	229.02
8	A3B2C1	3	2	1	82.00	360.89	223.19
9	A3B3C2	3	3	2	182.20	542.56	214.71

A: Voltage, B: Current, C: Welding Speed

Regression analysis was carried out by using the obtained data. Polynomial quadratic regression analysis with 95% confidence interval was performed. The results of analyses are shown in Figure 4.17, 4.18, and 4.19. CI in the graphs represents the confidence interval and PI represents the prediction interval.

As a result, it is seen from the obtained graphs that the impact energy, tensile strength, and hardness values are within the confidence interval. According to the results of graphs, it was determined that the test results were reliable.

Regression analysis results of impact energy are shown in Figure 4.17. R-sq value of impact test results is calculated as 95.7%. It was determined that the fit assigned to the impact energy values was reliable since almost all values were within the confidence interval.

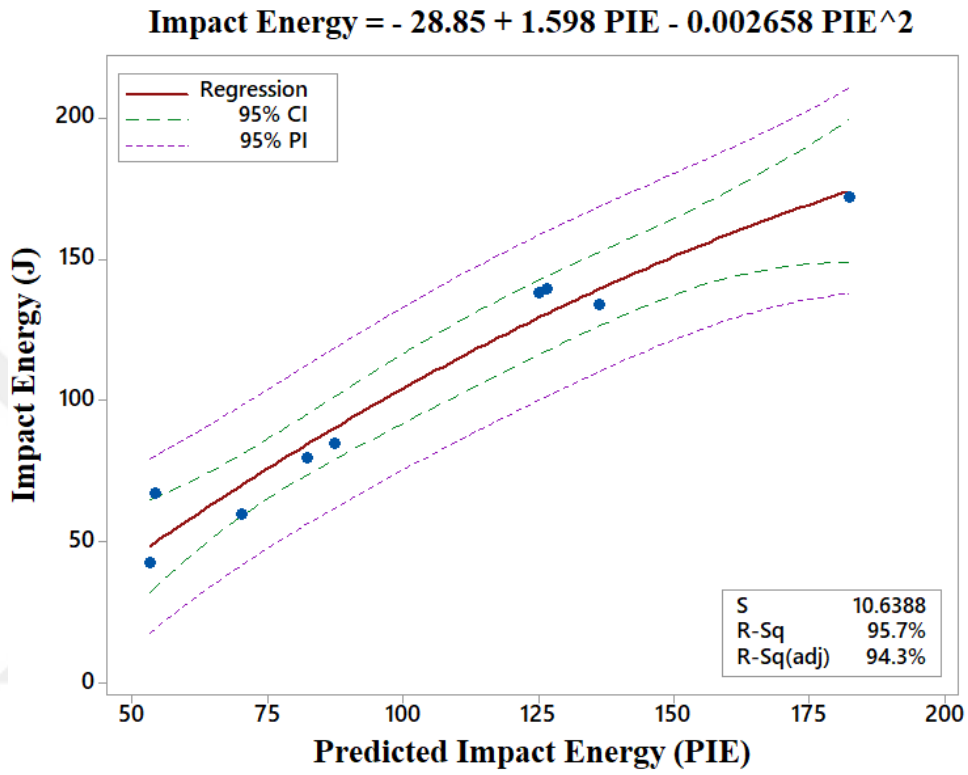

Figure 4.17 Fitted line plot for impact energy

Regression analysis results of tensile strength are shown in Figure 4.18. R-sq value of tensile test results is calculated as 81.3%. It was determined that the fit assigned to the tensile strength values was reliable since almost all values were within the confidence interval.

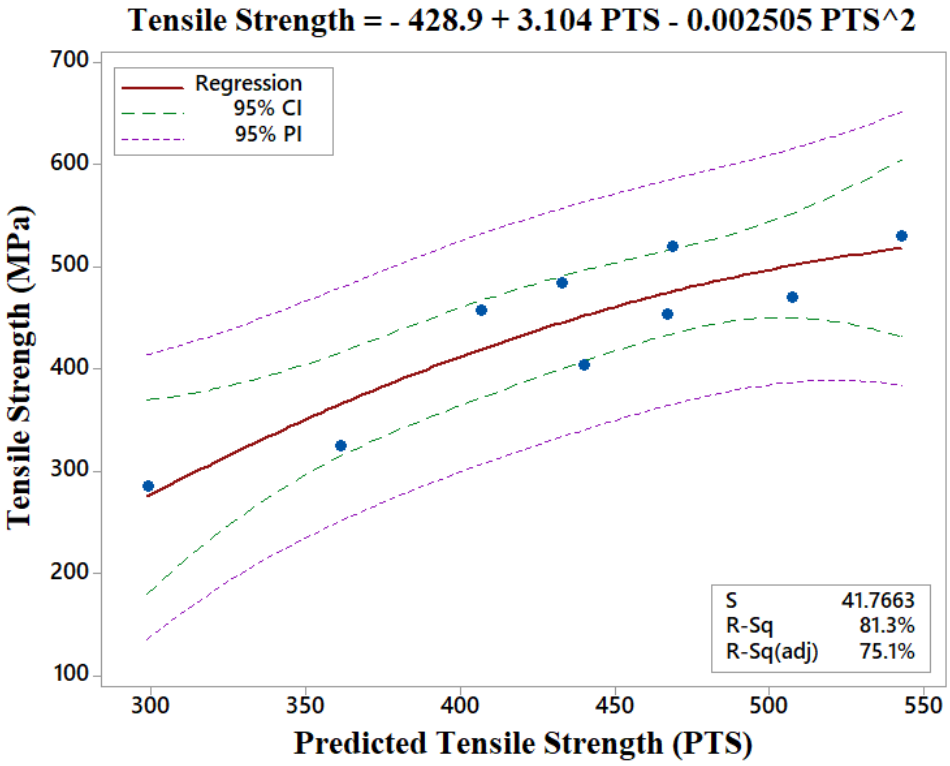

Figure 4.18 Fitted line plot for tensile strength

Regression analysis results of hardness are shown in Figure 4.19. R-sq value of hardness test results is calculated as 72.6%. It was determined that the fit assigned to the hardness values was reliable since almost all values were within the confidence interval.

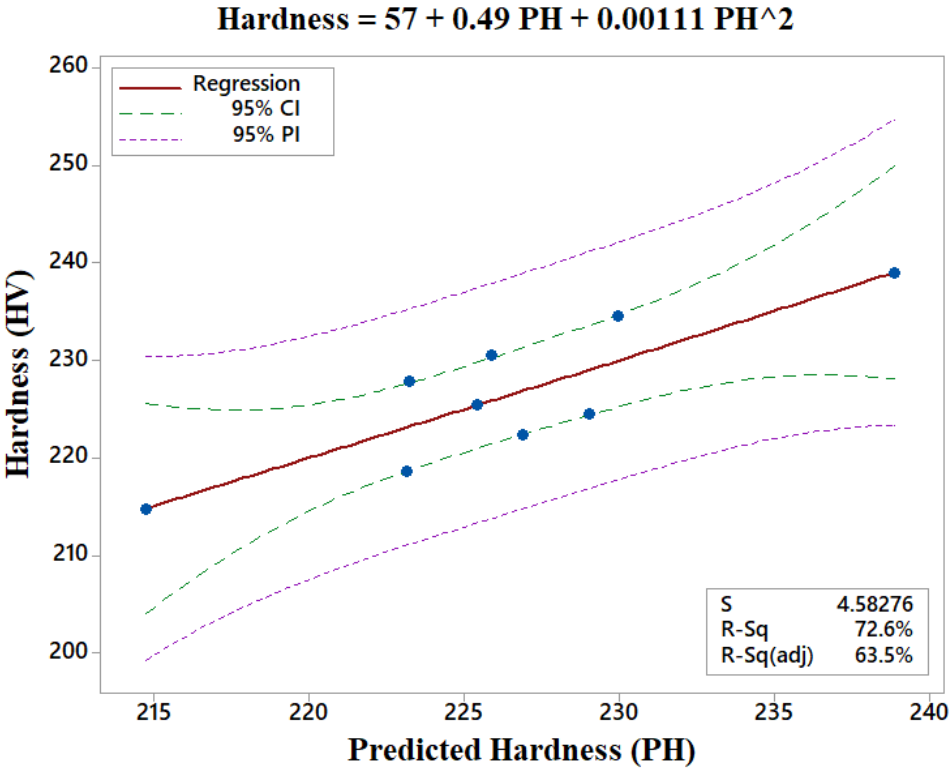

Figure 4.19 Fitted line plot for hardness

4.3 Gray Relational Analysis

Gray relational analysis was performed using the results of impact, tensile and hardness test. The gray relational analysis calculations for the impact energy result of A1B1C1 sample are given in detail below. The calculations for the A1B1C1 sample were also calculated for each value and the results of them are presented in the tables.

4.3.1 Normalization of the results

The gray relational analysis method, a multi-objective optimization tool, was used in this study. The approach is based on the logic of placing each response between 0 and 1. To do this, all responses are normalized. There are two alternative normalizations

based on how the responses contributed to the design. Equation 1.3 shows the "lower is better" approach, while Equation 1.2 shows the "higher is better" approach. The normalization value was calculated using Eq.1.2.

$$x_i^* \text{ (k)} = \frac{x_i^0 (k) - \min x_i^0(k)}{\max x_i^0(k) - \min x_i^0(k)} = \frac{42.55 - 42.55}{171.72 - 42.55} = 0 \quad (1.2)$$

The same procedure was applied to all results and the normalization results of them are shown in the Table 4.12.

Table 4.12 Normalization results

Experimental Set	Impact	Tensile	Hardness
1	0.000	0.000	0.441
2	0.189	0.705	0.155
3	0.326	0.758	0.648
4	0.705	0.484	0.817
5	0.131	0.689	1.000
6	0.748	0.959	0.310
7	0.737	0.811	0.400
8	0.287	0.160	0.538
9	1.000	1.000	0.000

4.3.2 Deviation Sequences

The deviation sequence values were calculated using Eq. 1.4. The results of all parameters are shown in Table 4.13.

$$\Delta_{0i}(1) = |1 - 0| = 1 \quad (1.4)$$

Table 4.13 Deviation Sequences

Experimental Set	Impact	Tensile	Hardness
1	1.000	1.000	0.559
2	0.811	0.295	0.845
3	0.674	0.242	0.352
4	0.295	0.516	0.183
5	0.869	0.311	0.000
6	0.252	0.041	0.690
7	0.263	0.189	0.600
8	0.713	0.840	0.462
9	0.000	0.000	1.000

4.3.3 Gray Relational Coefficient

GRC is express the relationship between the real and ideal normalized experimental results. GRC of A1B1C1 sample was calculated by using Eq. 1.5. The results of all parameters are shown in Table 4.14. Finally, the Gray Relational degree was found by the following Eq. 1.6.

$$\zeta_i(k) = \frac{\Delta_{min} + \zeta\Delta_{max}}{\Delta_{oi}(k) + \zeta\Delta_{max}} = \frac{0+(0.5)(1)}{1+(0.5)(1)} = 0.333 \quad (1.5)$$

Table 4.14 Gray Relational Coefficient

Experimental Set	Impact	Tensile	Hardness
1	0.333	0.333	0.472
2	0.381	0.629	0.372
3	0.426	0.674	0.587
4	0.629	0.492	0.732
5	0.365	0.616	1.000
6	0.665	0.924	0.420
7	0.655	0.726	0.455
8	0.412	0.373	0.520
9	1.000	1.000	0.333

4.3.4 Gray Relational Grades

Gray relational grades (GRG) were calculated with equal contribution. After calculating the GRG, they were ranked between each other. The optimum value was found from the ranking results. GRG and ranking results are shown in Table 4.15.

Table 4.15 Gray relational grades with equal contribution

#	Variables	A	B	C	Impact Energy	Tensile Strength	Hardness	GRG	Rank
	ABC	V	A	mm/min	Joule	MPa	HV		
1	A1B1C1	1	1	1	42.55	285	225.42	0.380	9
2	A1B2C2	1	2	2	66.95	457	218.50	0.461	7
3	A1B3C3	1	3	3	84.66	470	230.42	0.562	6
4	A2B1C3	2	1	3	133.60	403	234.50	0.618	4
5	A2B2C2	2	2	2	59.41	453	238.92	0.660	3
6	A2B3C1	2	3	1	139.21	519	222.25	0.670	2
7	A3B1C3	3	1	3	137.73	483	224.42	0.612	5
8	A3B2C1	3	2	1	79.56	324	227.75	0.435	8
9	A3B3C2	3	3	2	171.72	529	214.75	0.778	1

A: Voltage, B: Current, C: Welding Speed

According to the result of gray relational analysis, the optimum value was determined as A3B3C2 which was sample 9.

Since the R-sq value was low (72.6%) in the regression analysis, it was decided to determine the new gray relational grades by reducing the contribution ratio of the hardness test results. The contribution rate of the hardness test results was determined as 10%, and the contribution rate of the impact energy and tensile strength test results

was determined as 45%. A new gray relational analysis was performed with the updated contribution ratios. These results are presented in Table 4.16.

Table 4.16 Gray relational grades with 10% hardness, and 45% impact energy and tensile strength contribution

#	Variables	A	B	C	Impact Energy	Tensile Strength	Hardness	GRG	Rank
	ABC	V	A	mm/min	Joule	MPa	HV		
1	A1B1C1	1	1	1	42.55	285	225.42	0.347	9
2	A1B2C2	1	2	2	66.95	457	218.50	0.492	7
3	A1B3C3	1	3	3	84.66	470	230.42	0.554	5
4	A2B1C3	2	1	3	133.60	403	234.50	0.578	4
5	A2B2C2	2	2	2	59.41	453	238.92	0.542	6
6	A2B3C1	2	3	1	139.21	519	222.25	0.757	2
7	A3B1C3	3	1	3	137.73	483	224.42	0.667	3
8	A3B2C1	3	2	1	79.56	324	227.75	0.405	8
9	A3B3C2	3	3	2	171.72	529	214.75	0.933	1

A: Voltage, B: Current, C: Welding Speed

As a result of the new analysis, it was seen that the optimum value remained the same. On the other hand, there is a slight variation in other parameters.

4.4 Mechanical Test Results of Tempered Samples

Three new samples were joined with the parameters obtained as a result of the optimization. Samples which were heated at 250 ℃, 350 ℃, and 450 ℃ for 2 hours were named as sample A, sample B, and sample C, respectively.

4.4.1 Impact Test Results of Tempered Samples

According to the impact test results of tempered samples which were presented in Table 4.17. Significant increases were observed in the impact energy compared to the base metals. The fracture regions of the sample A, B, C, and 9 are shown in the Figure 4.20. Ductile rupture has occurred in the sample A and B. Despite having the highest impact energy, brittle rupture occurred in sample C.

Table 4.17 Impact test results of tempered samples and sample 9

Experimental Set	Impact Energy (J)
Sample 9	171.72
Sample A	155.26
Sample B	99.91
Sample C	175.51

Sample A: Heated at 250 ℃, Sample B: Heated at 350℃, Sample C: Heated at 450 ℃

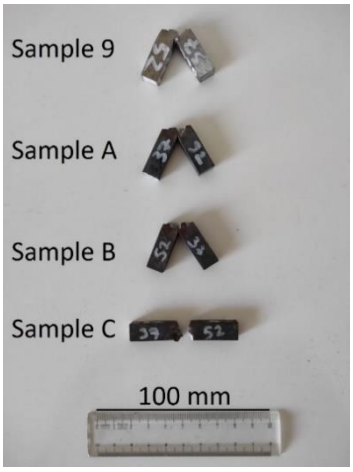

Figure 4.20 Fracture regions of the impact test sample A, B, C, and 9

4.4.2 Tensile Test Results of Tempered Samples

Tensile test results of tempered samples and sample 9 are shown in Table 4.18. Stress-strain graphs of tempered samples and sample 9 are also shown in Figure 4.21. Ductile rupture occurred in all samples. When the graphs are examined, tensile strength values decreases when temperature increases. Elongation values increases when temperature increases.

Table 4.18 Tensile test results of tempered samples and sample 9

Experimental Set	Tensile Strength (MPa)	Elongation (%)
Sample 9	529	17.5
Sample A	436	25.0
Sample B	430	25.3
Sample C	415	29.3

Sample A: Heated at 250 ℃, Sample B: Heated at 350℃, Sample C: Heated at 450 ℃

The lowest tensile strength was obtained in the sample C which was heated at 450℃. The highest tensile strength was obtained in the sample A which was heated at 250℃. Sample C has the highest elongation value. The lowest elongation value was seen in the sample A.

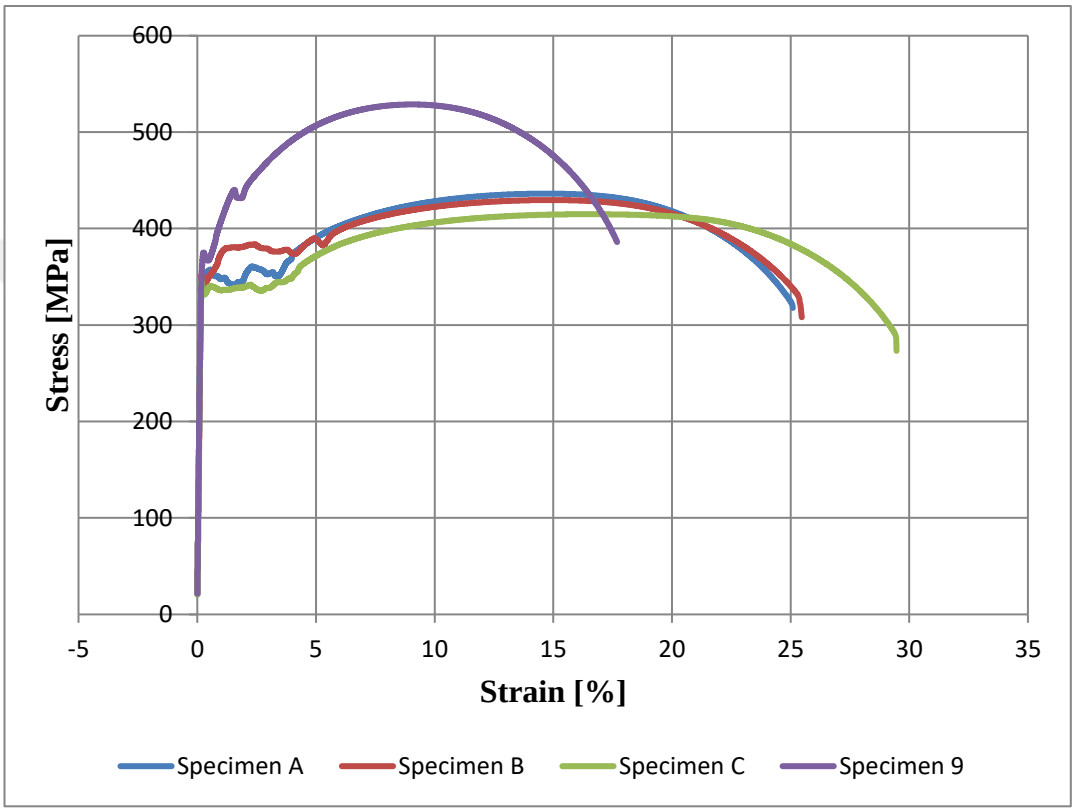

Figure 4.21 Stress-strain plot for Sample 9, A, B, and C

The fracture regions of tempered samples and sample 9 are shown in Figure 4.22. As can be seen from this figure that the fracture occurred in base material. As a result, it has been observed that the obtained results are compatible with the studies in the literature [60-63].

Figure 4.22 Fracture regions of the tempered tensile test samples and sample 9

4.4.3 Hardness Test Results of Tempered Samples

According to the impact test data presented in Table 4.19.

Table 4.19 Hardness test results of tempered samples and sample 9

Experimental Set	Hardness (HV)
Sample 9	215
Sample A	170
Sample B	167
Sample C	164

Sample A: Heated at 250 ℃, Sample B: Heated at 350℃, Sample C: Heated at 450 ℃

Hardness distribution of weld metal, heat affected zone and base metal of sample A, B, C, and 9 are given in Figure 4.23.

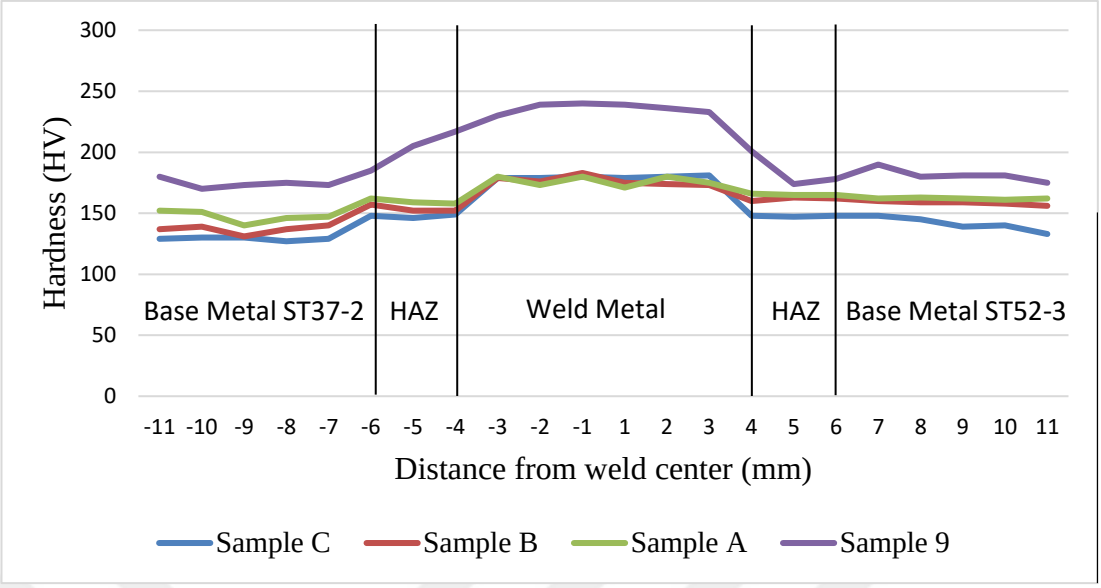

Figure 4.23 Hardness distribution of weld metal, heat affected zone (HAZ) and base metal of sample A, B, C, and 9

When the graph is examined, hardness values decreases when temperature increases. Sample A, B and C have low hardness value compared to sample 9. Weld metal and heat affected zone have high hardness value compared to base metal.

The lowest hardness value was obtained in the sample C which was heated at 450°C. The highest hardness value in between sample A, B, and C was obtained in the sample A which was heated at 250°C.

As a result, it has been observed that the obtained results are compatible with the studies in the literature [60-63].

4.4.4 Metallographic Examination of Tempered Samples and Sample 9

Most low carbon steels are essentially pure iron with small amounts of alloying elements such as manganese, silicon, and aluminum to improve their properties. With very few exceptions, the main component of low carbon steels is ferrite [64, 65]. Microstructures of base metals of sample A are shown in Figure 4.24 and 4.25. When the microstructure images of base metals were examined, it was observed that microstructure consisted of ferrite and perlite [55, 60, 66, 67]. The microstructure of the base metal was fine-grained and coaxial. When the images taken with 200x magnification were examined, it was evaluated that the ferritic structure was

distributed very homogenously, and the pearlitic structure showed a homogenous distribution, although in lesser amounts.

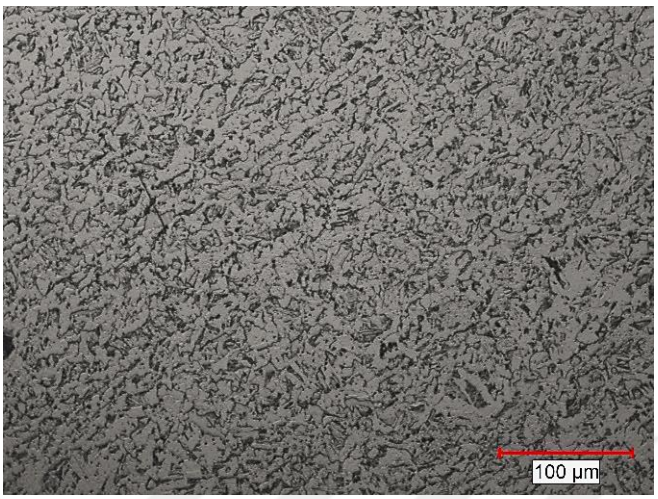

Figure 4.24 Optical microscope image of base metal (St37-2) of Sample A; 200x

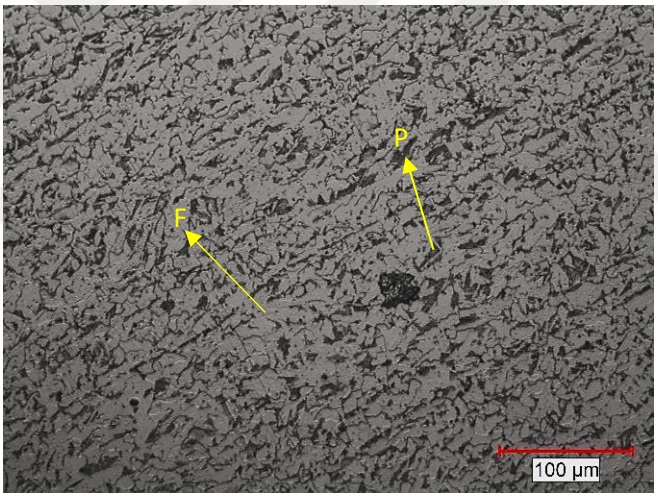

Figure 4.25 Optical microscope image of base metal (St52-3) of Sample A; 200x

Grain sizes of the samples were calculated according to the ASTM E112 standard. The average grain size of St37-2 base material which is in sample 9 has 9.74 micrometer (ASTM E-112, Grain Size No. 10). The average grain size of St52-3 base material which is in sample 9 has 8.92 micrometer (ASTM E-112, Grain Size No. 11). The average grain size of St37-2 base materials of sample 9, A, B, and C are shown in Figure 4.26.

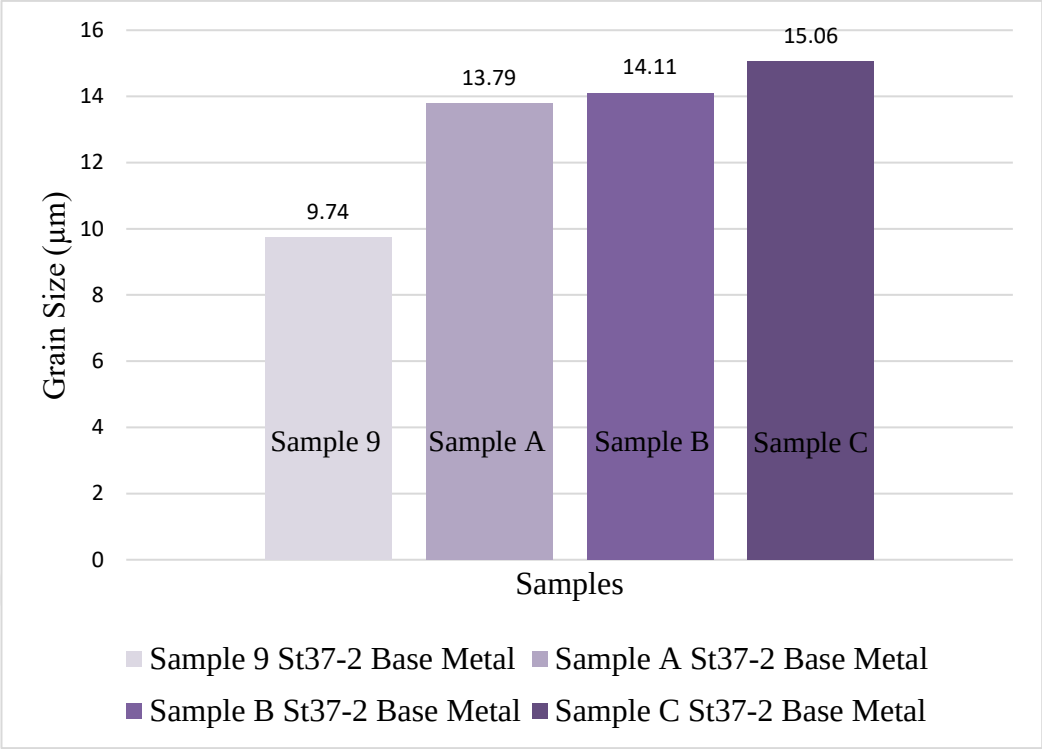

Figure 4.26 Average grain size of St37-2 base materials of sample 9 and sample A, B, and C which were heated at 250°C, 350°C, and 450°C, respectively

As can be seen from the particle sizes, sample C has the lowest hardness value among sample A, B, C, and 9.

In the heat affected zone of sample B, the structure is complex, and the distribution is uneven, as shown in Figure 4.27. The structures in the heat affected zone transform rapidly as they move away from the fusion line due to differences in heat input and heat conduction [68]. The transition from the St 37-2 steel to the weld metal region is clearly visible at 50x magnification. There is no significant thermomechanically affected zone in the samples.

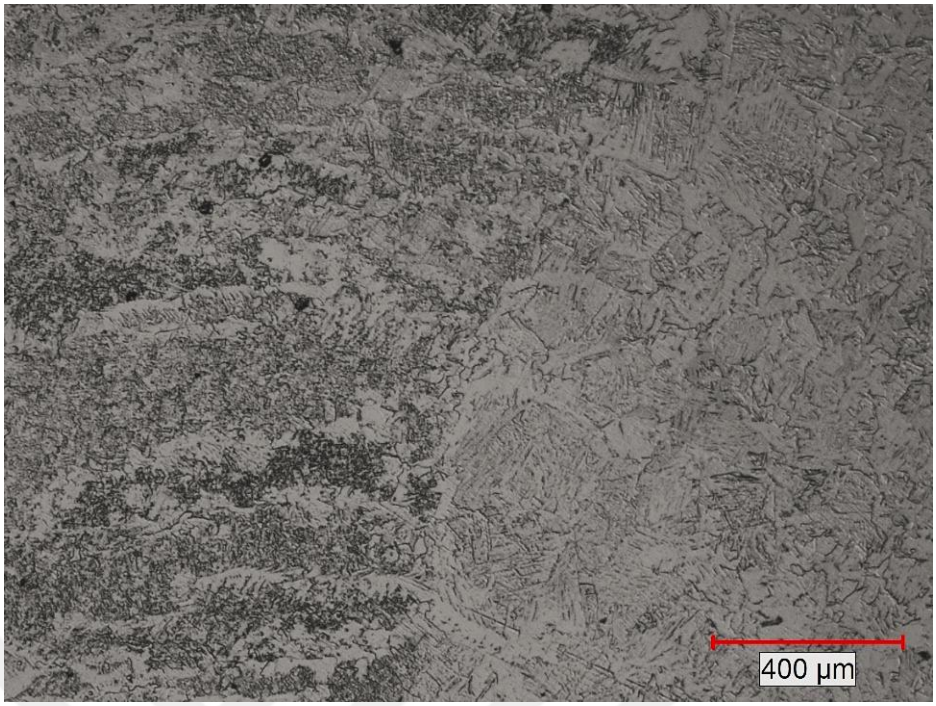

Figure 4.27 Transition zone from the HAZ region to the weld metal (Sample B); 50x

The average grain size of HAZ on St37-2 side which is in sample 9 has 7.76 micrometer (ASTM E-112, Grain Size No. 11). The average grain size of HAZ on side St52-3 which is in sample 9 has 8.31 micrometer (ASTM E-112, Grain Size No. 11). The average grain size of HAZ on side St37-2 and St52-3 base materials of sample 9, A, B, and C are shown in Figure 4.28 and 4.29, respectively.

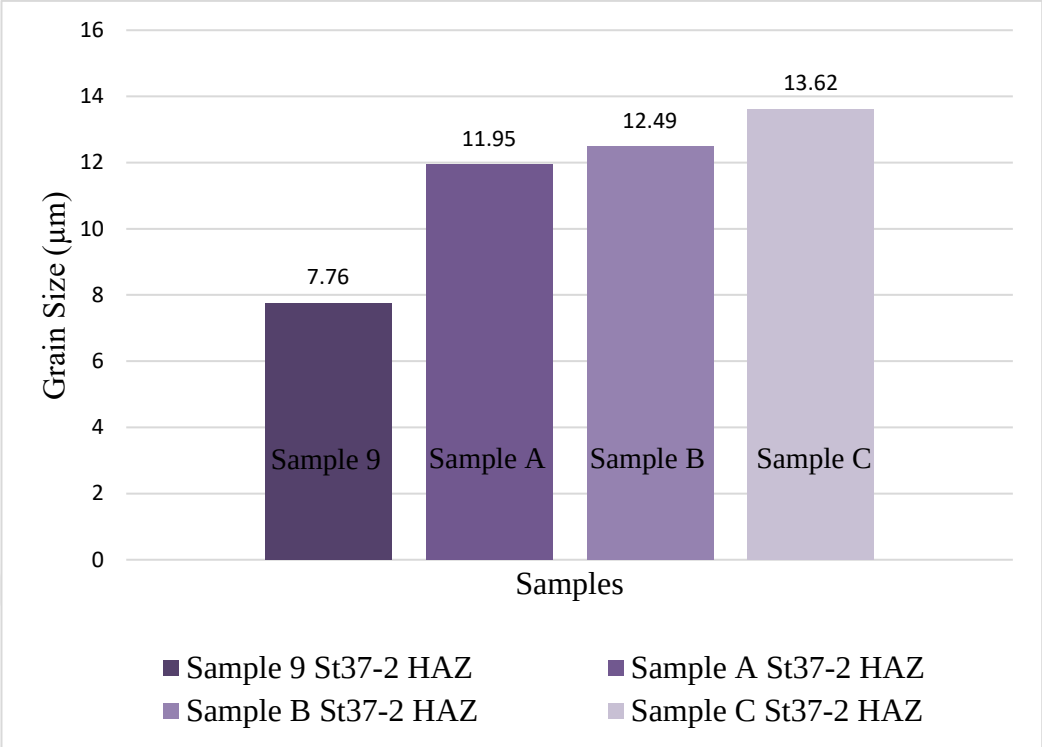

Figure 4.28 Average grain size of HAZ on side St37-2 which is in sample 9 and sample A, B, and C which were heated at 250°C, 350°C, and 450°C, respectively

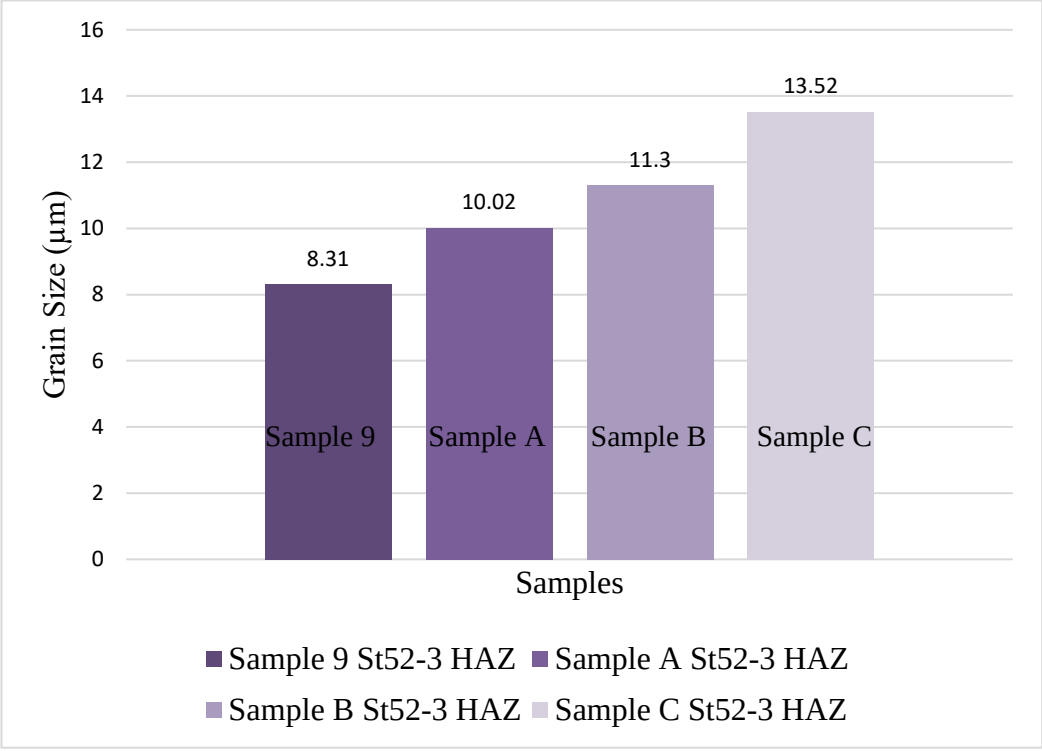

Figure 4.29 Average grain size of HAZ on side St52-3 which is in sample 9 and sample A, B, and C which were heated at 250°C, 350°C, and 450°C, respectively

The grain sizes in the heat affected zone are small compared to the grain sizes in the base material. As can be seen from the particle sizes, high hardness values were obtained in the HAZ according to the base metal.

Microstructures of weld metal of sample B is shown in Figure 4.30. When the microstructure images of weld metal were examined, it was observed that microstructure consisted of polygonal ferrite (PF), Widmanstatten ferrite (WF), and acicular ferrite (AF). It was observed that the microstructure obtained was similar to the studies in the literature [68]. Microstructures of weld metal of sample 9 is shown in Figure 4.31. When the microstructure images of weld metal of the sample 9 was examined, it was observed that microstructure mainly consisted of acicular ferrite. Polygonal ferrite was also observed in the microstructure. Unlike the sample 9, widmanstatten ferrite structures were found in sample B.

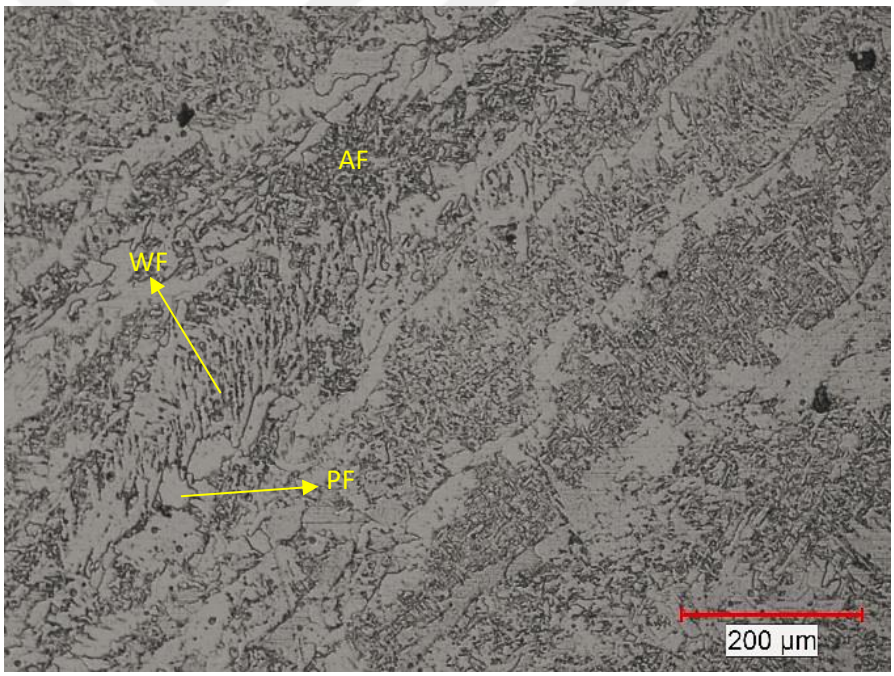

Figure 4.30 Optical microscope image of weld metal of Sample B; 100x

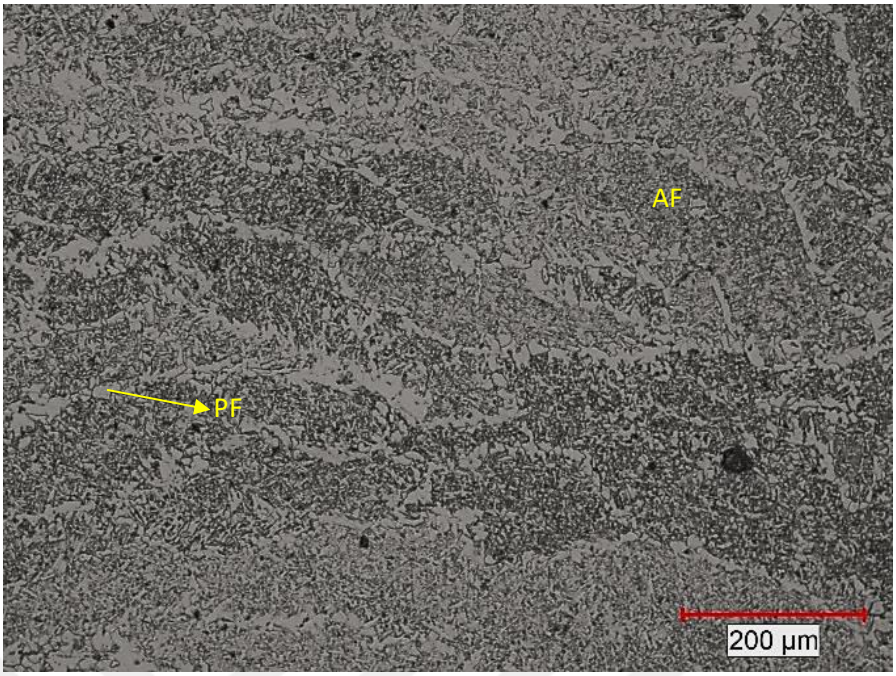

Figure 4.31 Optical microscope image of weld metal of Sample 9; 100x

Scanning Electron Microscope (SEM) analyses of weld metal of sample 9, A, B, and C were performed with a HITACHI TM4000Plus SEM instrument. SEM image of weld metal of sample B was shown in Figure 4.32. It was observed that microstructure consisted of PF, WF, and AF. SEM image of weld metal of sample 9 was shown in Figure 4.33. It was observed that microstructure consisted of AF and PF.

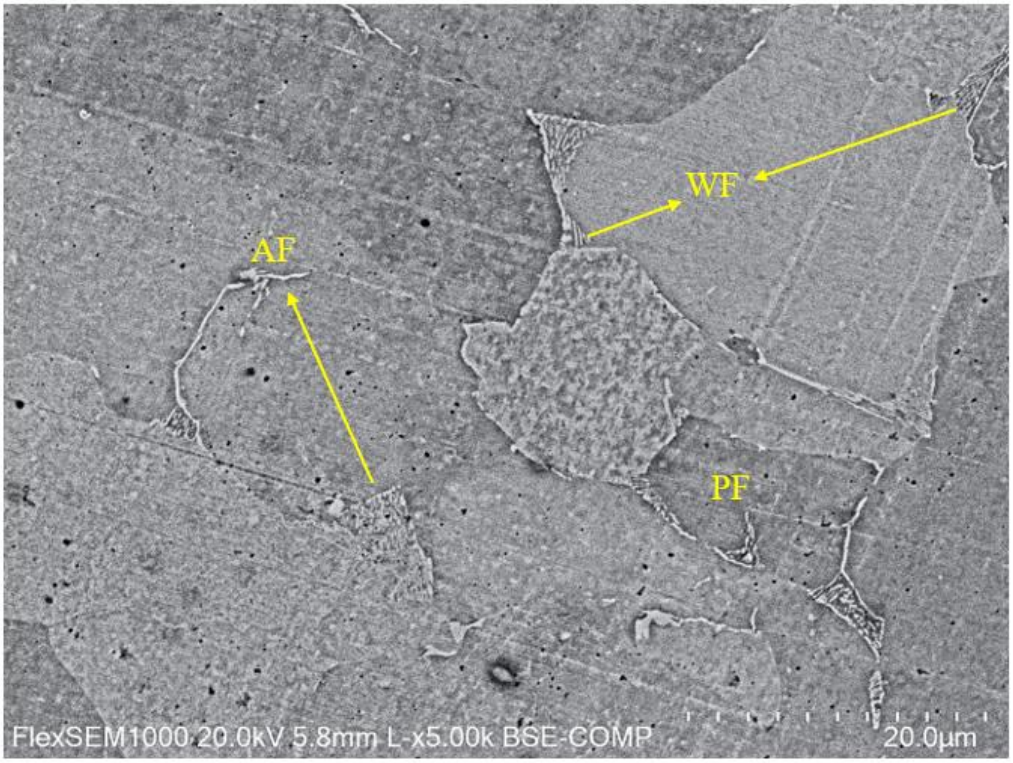

Figure 4.32 SEM image of weld metal of Sample B

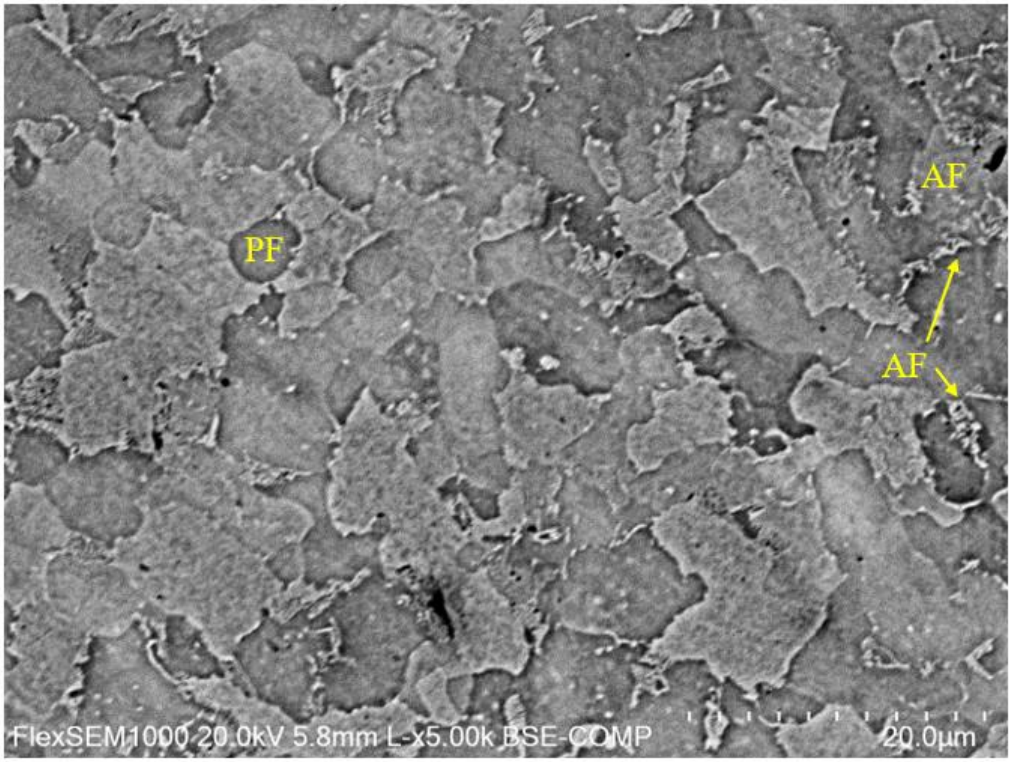

Figure 4.33 SEM image of weld metal of Sample 9

The average grain size of weld metal which is in sample 9 has 5.12 micrometer (ASTM E-112, Grain Size No. 12). The average grain size of weld metals of sample 9, A, B, and C are shown in Figure 4.34.

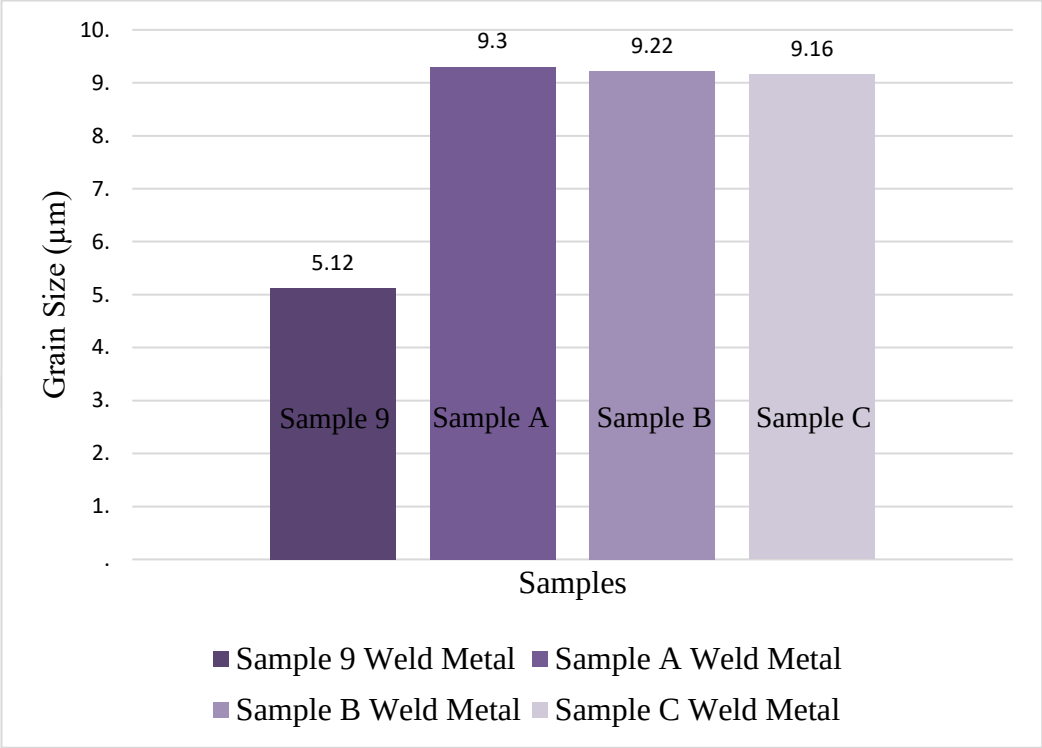

Figure 4.34 Average grain size of weld metals of sample 9 and sample A, B, and C which were heated at 250°C, 350°C, and 450°C, respectively

When the microstructure images of the samples were examined, an increase in the particle size was observed when the temper temperature which was applied to samples A, B, and C increased. Depending on the increase in particle size, the hardness values also decreased. As a result, it has been seen that the results obtained are compatible with the studies in the literature [60-63].

The X-Ray Diffraction (XRD) analyses of the weld metal of sample 9, A, B, and C were conducted for phase identification. XRD analyses were performed with a Rigaku Miniflex 600 XRD instrument. The XRD analysis of sample 9, A, B, and C are shown in Figure 4.35, 4.36, 4.37, and 4.38, respectively. According to results of XRD analysis, it was observed that there was no evidence of phase changes. The results of analyses support the presence of α-Iron (BCC, Ferrite) phase in the weld metal. The three peaks revealed in all XRD diagrams correspond to the ferrite phase. The peaks

and diffraction angle are indicated with their respective miller indices. Peaks corresponding to the ferrite was indexed based on respective (h, k, l) planes of phases.

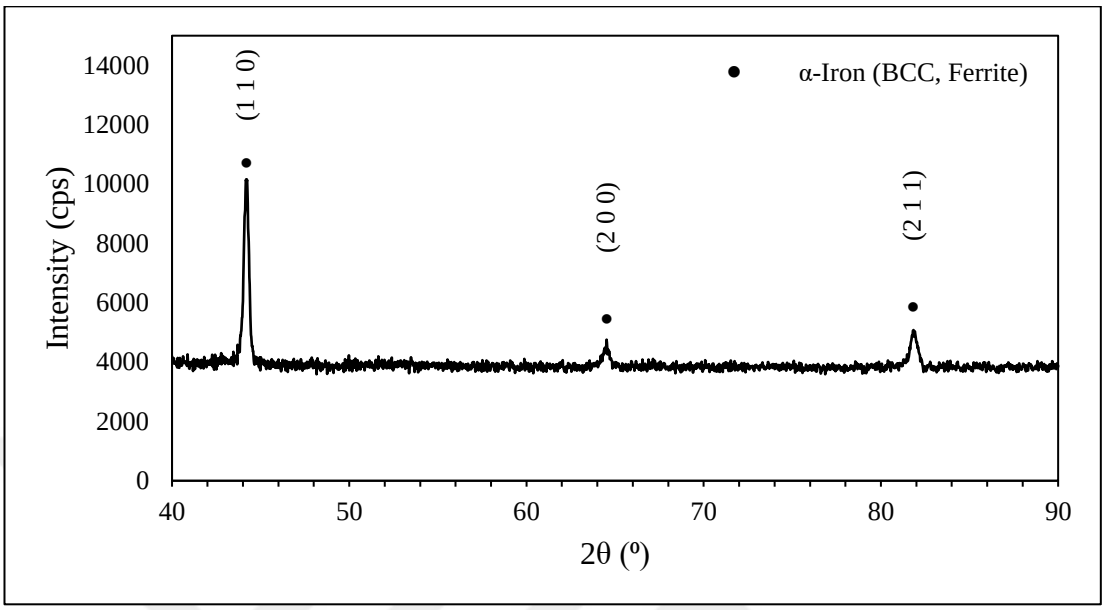

Figure 4.35 XRD pattern of weld metal of sample 9

It was observed that three peaks which were at the diffraction angles of 44.2º, 64.5º, and 81.8º revealed in XRD diagram of weld metal of sample 9.

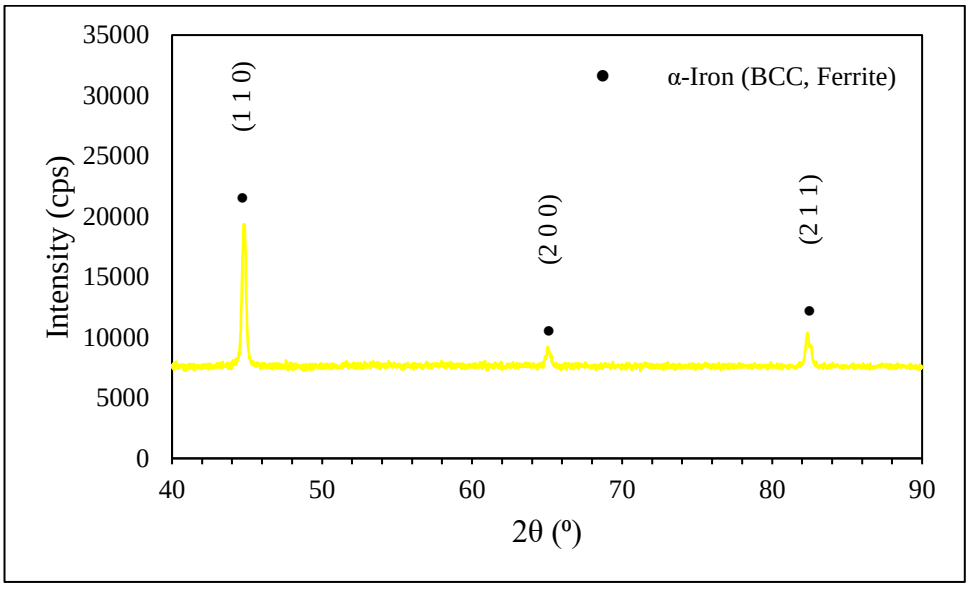

Figure 4.36 XRD pattern of weld metal of sample A

It was observed that three peaks which were at the diffraction angles of 44.8º, 65.2º, and 82.5º revealed in XRD diagram of weld metal of sample A.

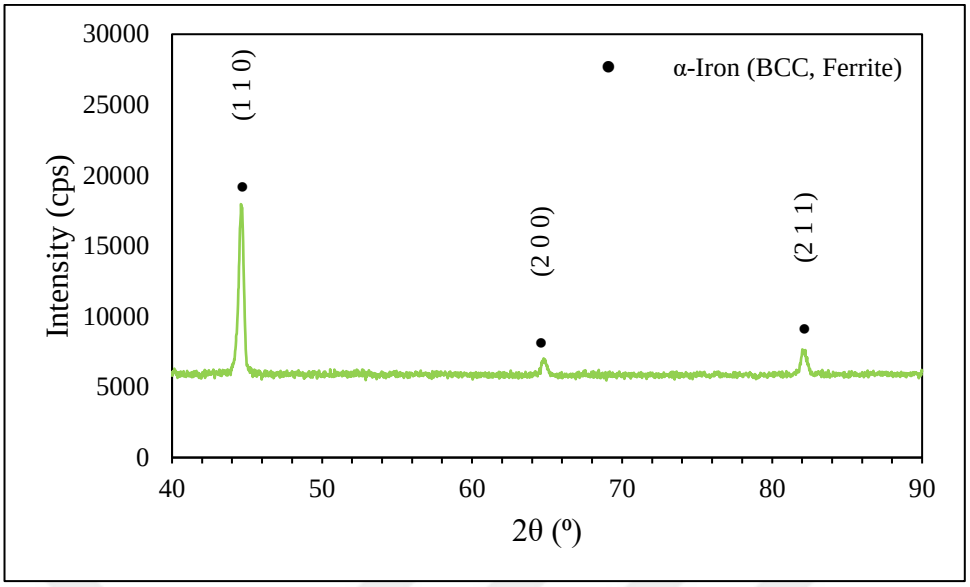

Figure 4.37 XRD pattern of weld metal of sample B

It was observed that three peaks which were at the diffraction angles of 44.7º, 65.0º, and 82.3º revealed in XRD diagram of weld metal of sample B.

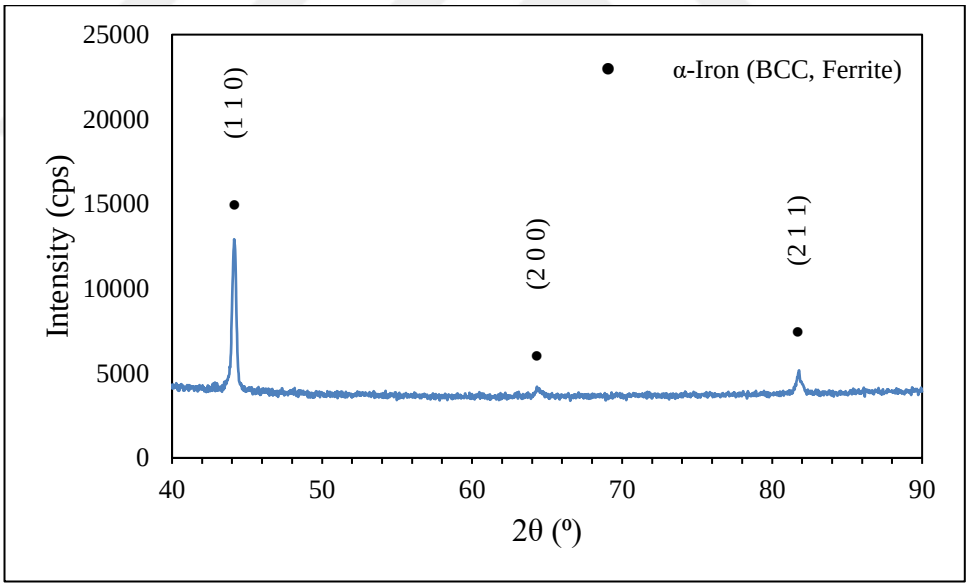

Figure 4.38 XRD pattern of weld metal of sample C

It was observed that three peaks which were at the diffraction angles of 44.4º, 64.5º, and 81.7º revealed in XRD diagram of weld metal of sample C. The X-ray diffraction analyses of sample A, B, and C are shown in Figure 4.39.

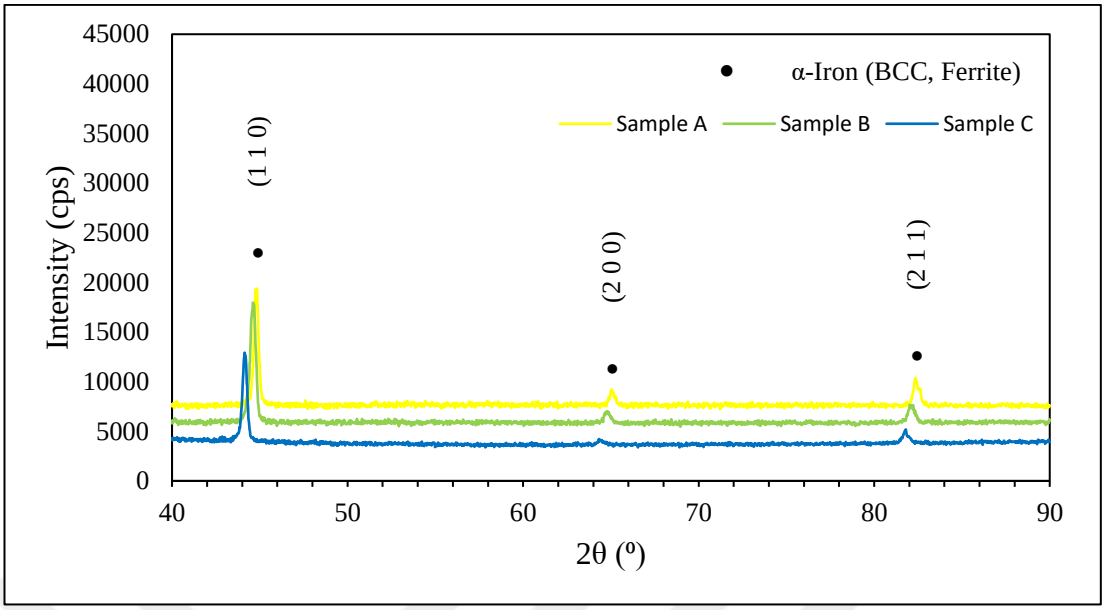

Figure 4.39 XRD pattern of weld metal of sample A, B, and C

4.5 Confirmation of Results

After determining the optimal level of process parameters, the error rate was calculated by comparing the test results obtained from the optimum process parameters with the predict values [69]. Since the optimum parameter values obtained as a result of Taguchi optimization are in the orthogonal array, there is no need for a validation experiment [70-72]. The validation and comparison of the results obtained through the combination of experimental and estimated parameters were shown in Table 4.20. The obtained results have negligible percentage of error. This error rate clearly shows that the study confirms its validity.

Table 4.20 The validation and comparison of the results

Description	Optimum Process Parameters		
	Prediction	Experimental	% of Error
Level	A3B3C2	A3B3C2	
Impact Energy	182.20	171.72	6.102958
Tensile Strength	543	529	2.646503
Hardness	214.71	214.75	0.018626

Taguchi analysis was performed by using the values of Gray relational grade. Main effects plot for S/N ratios of Gray relational grade values are shown in Figure 4.40. According to the results of this analysis, it has been seen that the optimum welding parameters are A3B3C2.

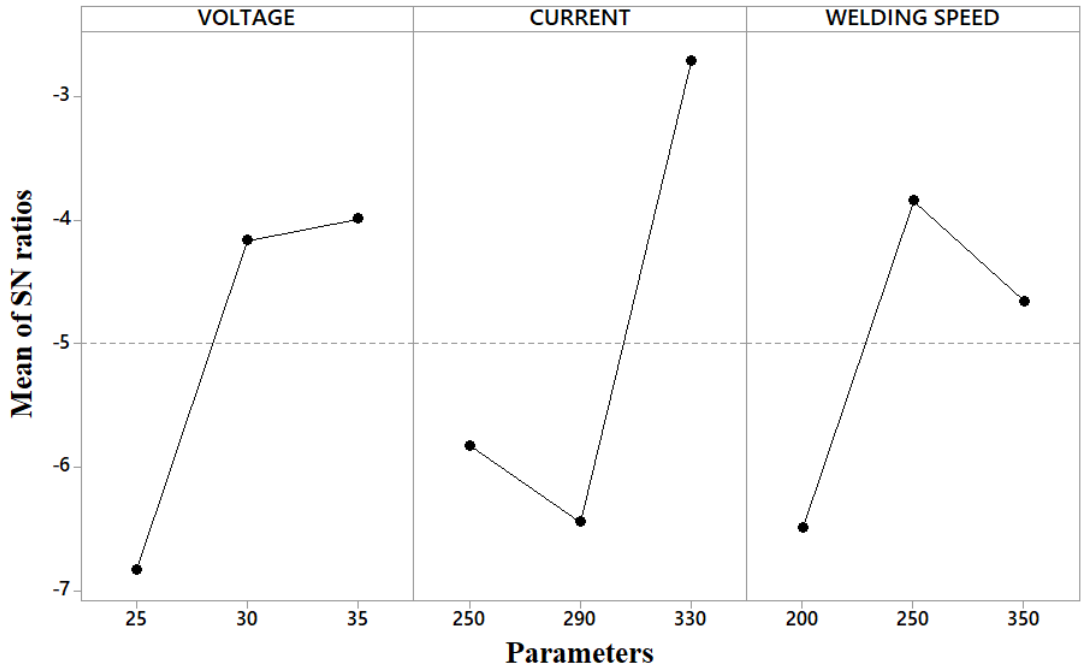

Figure 4.40 Main effects plot for S/N ratios of Gray relational grade values

CHAPTER 5

CONCLUSION and FUTURE WORKS

5.1 Conclusion

In this study, optimum welding parameters were determined by joining low alloy dissimilar steel materials which were St37-2 and St52-3 steels by GMAW method. The mechanical properties of the samples were examined in terms of tensile strength, impact strength and hardness. Taguchi method was used in design of experiment and the optimization processes. After Taguchi analysis, three new samples were welded under the optimum welding parameters. These samples were exposed to three different temper temperatures 250℃, 350℃, and 450℃. Thus, the effect of temper temperature on microstructure and mechanical properties was investigated.

Nowadays, the weldability of different alloy materials with GMAW is one of the most important subjects in the manufacturing industry where St37-2 and St52-3 materials are frequently used in various industries.

Firstly, in this study the most suitable weld structure was investigated experimentally and statistically by using different weld parameters. Then, the effect of temper temperature on the weld structure was investigated.

As seen in the experimental results, improvements in mechanical properties were obtained compared to low alloy steels. The results obtained from this study constitute a data source for future studies.

Optimum parameters according to Taguchi and Gray relational analysis are summarized in Table 5.1.

Table 5.1 Optimum parameters for welded samples

Method	Target	Optimum Parameters	ANOVA Contribution
Taguchi Analysis	Impact Energy	A3B3C2	Voltage
	Tensile Strength	A2B3C3	Current
	Hardness	A2B2C3	Voltage
Gray Relational Analysis	Overall	A3B3C2	

The results of the experimental and statistical analyzes are summarized below.

- Among the nine samples in the Taguchi experimental set, the highest tensile strength and impact energy were obtained at sample 9.
- According to the Gray relational analysis results, optimum welding parameters were obtained at 35 V, 330 A and 250 mm/min values.
- It was found that the most effective factors for the impact energy, tensile strength, and hardness were voltage, current, and voltage, respectively.
- The grain sizes in the HAZ and weld metal were smaller than the grain sizes in the base metal. According to the hardness test results, it has seen that higher hardness values are obtained in HAZ and weld metal compared to base metal.
- According to results of XRD analysis, it was observed that there was no evidence of phase changes. The results of analyses support the presence of α-Iron (BCC, Ferrite) phase in the weld metal.
- It has been observed that the porosities in the weld metal have a negative effect on the impact resistance.
- According to the mechanical test results of the samples joined with optimum welding parameters, it has seen that as the temper temperature increases, the

tensile strength decreases, the elongation increases, and the hardness value decreases. In addition, as the tempering temperature increased, an increase in grain size was observed, and accordingly, a decrease in hardness values was observed. Among the tempered samples, sample C was found to have the highest elongation value.

- As a result of the tensile test, it was observed that fractures occurred on the base metal in the tempered samples and the sample 9.
- It was observed that the elongation amount of all tempered samples was higher than the elongation amount of the sample 9.

5.2 Future Works

In future studies, by using optimum welding parameters, the effect of electrode wire on the mechanical properties of the weld can be examined by using different electrodes such as cored wire. Optimization can be made to determine the optimum electrode wire diameter by using electrodes with different chemical properties and different diameters. By using the optimum welding parameters, the effects of different weld groves like singe V and double V butt joints on the weld structure can be examined.

REFERENCES

[1] Anık, S., Anık, E., Vural, M (Ed.). *Kaynak Tekniği El Kitabı*. İstanbul: Gedik Eğitim Vakfı Kaynak Teknolojisi Eğitim Araştırma ve Muayene Enstitüsü, 2008

[2] Muzakki, H., Prasetyo, T., Umam, M. S. U., Lumintu, I., & Hartanto, D. (2020, July). Effect of Metal Inert Gas Welding Process Parameters to Tensile Strength on ST 37 Steel Sheet Joint. In *Journal of Physics: Conference Series* (Vol. 1569, No. 3, p. 032055). IOP Publishing.

[3] Utkarsh, S., Neel, P., Mahajan, M. T., Jignesh, P., & Prajapati, R. B. (2014). Experimental investigation of MIG welding for ST-37 using design of experiment. *International Journal of Scientific and Research Publications*, *4*(5), 1.

[4] Patil, S. R., & Waghmare, C. A. (2013). Optimization of MIG welding parameters for improving strength of welded joints. *Int. J. Adv. Engg. Res. Studies/II/IV/July-Sept*, *14*, 16.

[5] 2018 JETIR March 2018, Volume 5, Issue 3 www.jetir.org (ISSN-2349-5162) JETIR1803087, Journal of Emerging Technologies and Innovative Research (JETIR), Optimization of Mig Welding Parameters For Improving Strength Of Welded Joints, T Appa Rao , Paturi Venkata Rattayya Chowdary , Sriram. Vasamsetti

[6] Hooda, A., Dhingra, A., & Sharma, S. (2012). Optimization of MIG welding process parameters to predict maximum yield strength in AISI 1040. *International journal of Mechanical engineering and Robotics research*, *1*(3), 203-213.

[7] Das, B., Debbarma, B., Rai, R. N., & Saha, S. C. (2013). Influence of process parameters on depth of penetration of welded joint in mig welding process. *International journal of research in engineering and technology*, *2*(10), 220-224.

[8] Ghosh, N., Pal, P. K., & Nandi, G. (2017). GMAW dissimilar welding of AISI 409 ferritic stainless steel to AISI 316L austenitic stainless steel by using AISI 308 filler

wire. *Engineering science and technology, an international journal*, *20*(4), 1334-1341.

[9] Dixit, V., Thakur, Y., Gaurav, A., Singh, I., & Rajora, V. Influence of Varying Welding Current on Impact Strength of Metal Inert Gas Welding Joints.

[10] Biswal, B. B., Sarkar, B. K., & Mahanta, P. (Eds.). (2020). *Advances in Mechanical Engineering: Select Proceedings of ICRIDME 2018*. Springer Singapore.

[11] Ghazvinloo, H. R., & Honarbakhsh-Raouf, A. (2020). Mechanical strength of the weld metal in CK45 carbon steel. *Materials Science*, *56*(2), 210-213.

[12] Kaçar, R., & Kökemli, K. (2005). Effect of controlled atmosphere on the mig-mag arc weldment properties. *Materials & design*, *26*(6), 508-516.

[13] Rout, A., BBVL, D., & Biswal, B. B. (2020). Optimization of process variables of laser sensor assisted robotic GMAW process for mild steel material. *Materials and Manufacturing Processes*, *35*(15), 1690-1700.

[14] Deshpande, M. U., Kshirsagar, J. M., & Dharmadhikari, H. M. (2017). Optimization of GMAW Process Parameters to Improve the Length of Penetration in EN 10025 S 235 Grade. *Journal of Welding and Joining*, *35*(1), 74-78.

[15] Casarini, A., Coelho, J. P., Olívio, E., Braz-César, M. T., & Ribeiro, J. E. (2020). Optimization and influence of GMAW parameters for weld geometrical and mechanical properties using the Taguchi method and variance analysis. In *ICEUBI2019 International Congress on Engineering—Engineering for Evolution* (pp. 781-794).

[16] Hackenhaar, W., Gonzalez, A. R., Machado, I. G., & Mazzaferro, J. A. (2018). Welding parameters effect in GMAW fusion efficiency evaluation. *The International Journal of Advanced Manufacturing Technology*, *94*(1), 497-507.

[17] Nobrega, G., Souza, M. S., Rodríguez-Martín, M., Rodríguez-Gonzálvez, P., & Ribeiro, J. (2021). Parametric optimization of the GMAW welding process in thin

thickness of austenitic stainless steel by Taguchi method. *Applied Sciences*, *11*(18), 8742.

[18] Kuppusamy, A., Rameshkumar, K., Sumesh, A., & Premkumar, S. (2020). Gas Metal Arc Welding Process Parameter Optimization to Reduce Porosity Defect in a Longitudinal Seam Welding of Pressure Vessels. *SAE International Journal of Materials and Manufacturing*, *13*(1), 61-80.

[19] Sarkar, A., & Das, S. (2016). Selection of Appropriate Process Parameters for Gas Metal Arc Welding of a Steel under 100% Carbon Dioxide Gas Shield. *Indian Welding Journal*, *49*(4), 79-88.

[20] John, B., Paulraj, S., & Mathew, J. (2016). The role of shielding gas on mechanical, metallurgical and corrosion properties of corten steel welded joints of Railway Coaches using GMAW. *Advances in Science and Technology. Research Journal*, *10*(32).

[21] Ebrahimnia, M., Goodarzi, M., Nouri, M., & Sheikhi, M. (2009). Study of the effect of shielding gas composition on the mechanical weld properties of steel ST 37-2 in gas metal arc welding. *Materials & Design*, *30*(9), 3891-3895.

[22] Mezaache, M., Benaouda, O. F., Chaouch, S., Babes, B., & Amraoui, R. (2022). Optimizing MAG Welding Input Variables to Maximize Penetration Depth Using Particle Swarm Optimization Algorithm. *Engineering Proceedings*, *14*(1), 5.

[23] Sankar, B. V., Lawrence, I. D., & Jayabal, S. (2018). Experimental study and analysis of weld parameters by GRA on MIG welding. *Materials Today: Proceedings*, *5*(6), 14309-14316.

[24] Moghaddam, M. A., Golmezergi, R., & Kolahan, F. (2016). Multi-variable measurements and optimization of GMAW parameters for API-X42 steel alloy using a hybrid BPNN–PSO approach. *Measurement*, *92*, 279-287.

[25] Abima, C. S., Akinlabi, S. A., Madushele, N., & Akinlabi, E. T. (2021). Process Parameters Optimization for GMA Welding of AISI 1008 Steel Joints for Optimal Tensile Strength. *Revue des Composites et des Matériaux Avancés*, *31*(6).

[26] Kamble, A. G., & Rao, R. V. (2013). Experimental investigation on the effects of process parameters of GMAW and transient thermal analysis of AISI321 steel. *Advances in Manufacturing*, *1*(4), 362-377.

[27] Ampaiboon, A., Lasunon, O. U., & Bubphachot, B. (2015). Optimization and prediction of ultimate tensile strength in metal active gas welding. *The Scientific World Journal*, *2015*.

[28] Aghakhani, M., Jalilian, M. M., Karami, A., & Jalilian, M. M. (2012). Optimization of GMAW Process using Imperialist Competitive Algorithm. In *Applied Mechanics and Materials* (Vol. 110, pp. 3575-3579). Trans Tech Publications Ltd.

[29] Kumar, A., Khurana, M. K., & Yadav, P. K. (2016, September). Optimization of gas metal arc welding process parameters. In *IOP Conference Series: Materials Science and Engineering* (Vol. 149, No. 1, p. 012002). IOP Publishing.

[30] Srivastava, S., & Garg, R. K. (2017). Process parameter optimization of gas metal arc welding on IS: 2062 mild steel using response surface methodology. *Journal of Manufacturing Processes*, *25*, 296-305.

[31] Sathiya, P., Ajith, P. M., & Soundararajan, R. (2013). Genetic algorithm based optimization of the process parameters for gas metal arc welding of AISI 904 L stainless steel. *Journal of Mechanical Science and Technology*, *27*(8), 2457-2465.

[32] Kumar, S., & Singh, R. (2019). Optimization of process parameters of metal inert gas welding with preheating on AISI 1018 mild steel using grey based Taguchi method. *Measurement*, *148*, 106924.

[33] Ghosh, N., Rudrapati, R., Pal, P. K., & Nandi, G. (2017). Parametric optimization of gas metal Arc welding process by using Taguchi method on ferritic stainless steel AISI409. *Materials Today: Proceedings*, *4*(2), 2213-2221.

[34] Liang, Z. L., Yun, T. J., Oh, W. B., Lee, B. R., & Kim, I. S. (2020). A study on MOORA-based Taguchi method for optimization in automated GMA welding process. *Materials Today: Proceedings*, *22*, 1778-1785.

[35] Ates, H., Dursun, B., & Kurt, E. (2016). Estimation of mechanical properties of welded S355J2+ N steel via the artificial neural network. *Scientia Iranica*, *23*(2), 609-617.

[36] Kim, I. S., Basu, A., & Siores, E. (1996). Mathematical models for control of weld bead penetration in the GMAW process. *The International Journal of Advanced Manufacturing Technology*, *12*(6), 393-401.

[37] Groover, M. P. (2008). *Fundamentals of modern manufacturing: materials, processes, and systems*. John Wiley & Sons.

[38] Eryürek, İ. B. (2007). Gazaltı ark kaynağı. *Askaynak Kaynak Teknolojisi Kaynak Tekniği Ticaret ve Sanayi AŞ Yayınları, İstanbul*.

[39] Rizvi, S. A. (2018). Application of Taguchi technique to optimize the GMA welding parameters and study of fracture mode characterization of AISI 304H welded joints. *International Review of Applied Sciences and Engineering*, *9*(1), 9-16.

[40] Kılıç, A. Improving strength of rail steel and investigation of main mechanical and microstructural properties, Published / master's thesis, Ankara Yıldırım Beyazıt University, 2021

[41] Taguchi, G., Chowdhury, S., & Wu, Y. (2004). *Taguchi's quality engineering handbook*. John Wiley & Sons.

[42] Tklmas, *Grey relational analysis,* Retrieved July 12, 2022, https://en.wikipedia.org/wiki/Grey_relational_analysis, 2008.

[43] Xiao, X. C., Wang, X. Q., Fu, K. Y., & Zhao, Y. J. (2012). Grey relational analysis on factors of the quality of web service. *Physics Procedia*, *33*, 1992-1998.

[44] Geum, Y., Cho, Y., & Park, Y. (2011). A systematic approach for diagnosing service failure: Service-specific FMEA and grey relational analysis approach. *Mathematical and Computer Modelling*, *54*(11-12), 3126-3142.

[45] Patel, G. M., Krishna, P., & Parappagoudar, M. B. (2014). Optimization of squeeze cast process parameters using Taguchi and grey relational analysis. *Procedia Technology*, *14*, 157-164.

[46] Patil, A. N., Bhale, N. G. P., Raikar, N., & Prabhakaran, M. (2017). Car selection using hybrid fuzzy AHP and grey relation analysis approach. *International Journal of Performability Engineering*, *13*(5), 569.

[47] Özler, L. AISI 1010 Malzemesinin Sürtünmeli Delinmesinde Optimum Parametrelerin Gri İlişkisel Analiz Yöntemiyle Belirlenmesi. *Fırat Üniversitesi Mühendislik Bilimleri Dergisi*, *31*(2), 535-544. 2019

[48] N. Tosun, C. Cogun, and G. Tosun, "A study on kerf and material removal rate in wire electrical discharge machining based on Taguchi method," *J. Mater. Process. Technol.*, vol. 152, no. 3, pp. 316–322, 2004, doi: 10.1016/j.jmatprotec.2004.04.373.

[49] E. Nas and N. A. Ozbek, "Optimization the Machining Parameters in Turning of Hardened Hot Work Tool Steel Using Cryogenically Treated Tools," *Surf. Rev. Lett.*, 2019, doi: 10.1142/S0218625X19501774.

[50] E. Nas and S. Akıncıoğlu, "Kriyojenik İşlem Görmüş Nikel Esaslı Süper Alaşımın Elektro- Erozyon İşleme Performansı Optimizasyonu Optimization of Cryogenic Treated Nickel-Based Superalloy in Terms of Electro- Erosion Processing Performance," *Acad. Platf. J. Eng. Sci.*, vol. 7–1, pp. 115–126, 2019, doi: 10.21541/apjes.412042.

[51] Taşkesen A, Kütükde K. Experimental investigation and multi-objective analysis on drilling of boron carbide reinforced metal matrix composites using grey relational analysis. Meas J Int Meas Confed 2014. doi:10.1016/j.measurement.2013.08.040.

[52] Bilge T, Motorcu AR, Ivanov A. Optimization of drilling parameters for dimensional accuracy in drilling of compact laminate composite 2017;9:1–22.

[53] Yılmaz, E. and Güngör, F., "Gri İlişkisel Analiz Yöntemine Göre Farklı Sertliklerde Optimum Takım Tutucusunun Belirlenmesi," in *2. Ulusal Tasarım İmalat ve AnalizK ongresi*, 2010, pp. 1–9.

[54] Maijuansyah, M., Pradana, Y. R. A., Jatisukamto, G., & Solichin, S. (2019). Study on The Thermal Distortion, Hardness and Microstructure of St 37 Steel Plate Joined Using FCAW. *Journal of Mechanical Engineering Science and Technology (JMEST)*, *3*(1), 18-28.

[55] İpekoğlu, G., Küçükömeroğlu, T., Aktarer, S. M., Sekban, D. M., & Çam, G. (2019). Investigation of microstructure and mechanical properties of friction stir welded dissimilar St37/St52 joints. *Materials Research Express*, *6*(4), 046537.

[56] Amanollahi, A., Ebrahimzadeh, I., Raeissi, M., & Saeidi, N. (2021). Laminated steel/aluminum composites: Improvement of mechanical properties by annealing treatment. *Materials Today Communications*, *29*, 102866.

[57] Adedayo, A. V., Ibitoye, S. A., & Oluwole, O. O. (2011). Tempering heat treatment effects on steel welds. *Journal of Minerals and Materials Characterization and Engineering*, *10*(8), 755-764.

[58] Kumar, P., & Sinha, A. N. (2018). Microstructure and mechanical properties of pulsed Nd: YAG laser welding of st37 carbon steel. *Procedia computer science*, *133*, 733-739.

[59] Aghakhani, M., Mehrdad, E., & Hayati, E. (2011). Parametric optimization of gas metal arc welding process by Taguchi method on weld dilution. *International journal of modeling and optimization*, *1*(3), 216.

[60] Goo, B. C. (2021). Effect of Post-Weld Heat Treatment on the Fatigue Behavior of Medium-Strength Carbon Steel Weldments. *Metals*, *11*(11), 1700.

[61] Tanimu, I., Danjuma S, Y., & Shekarau Y, A. (2013). Effects of gas metal arc welding techniques on the mechanical properties of duplex stainless steel. *Journal of minerals and materials Characterization and Engineering*, *2013*.

[62] Pandey, C., Mahapatra, M. M., Kumar, P., & Saini, N. (2018). Dissimilar joining of CSEF steels using autogenous tungsten-inert gas welding and gas tungsten arc welding and their effect on δ-ferrite evolution and mechanical properties. *Journal of Manufacturing Processes*, *31*, 247-259.

[63] Olawale, J. O., Ibitoye, S. A., Oluwasegun, K. M., Shittu, M. D., & Ofoezie, R. C. (2012). Correlation between process variables in shielded metal-arc welding (SMAW) process and post weld heat treatment (PWHT) on some mechanical properties of low carbon steel welds. *Journal of Minerals and Materials Characterization and Engineering*, *11*(9), 891-895.

[64] Yılmaz, T. Masif ve Özlü Kaynak Telleri ile birleştirilen Hardox 400 Çeliklerinin Mekanik ve Mikroyapı Özellikleri, Published / master's thesis, Sakarya University, 2010.

[65] Handbook, A. S. M. (2004). Metallography and microstructures. *Edited by GF Vander Voort, ASM Intenational*, *9*.

[66] İrsel, G. (2022). Study of the microstructure and mechanical property relationships of shielded metal arc and TIG welded S235JR steel joints. *Materials Science and Engineering: A*, *830*, 142320.

[67] Boumerzoug, Z., Derfouf, C., & Baudin, T. (2010). Effect of welding on microstructure and mechanical properties of an industrial low carbon steel. *Engineering*, *2*(7), 502.

[68] Liu, J., Li, X., Zhou, Y., Yu, P., He, C., & Xu, Z. (2022). Microstructure and Mechanical Properties of Active Gas Arc Welding between 304 Austenitic Stainless Steel and Q235B Low Carbon Steel. *Journal of Materials Engineering and Performance*, 1-11.

[69] Mondal, S., Bandyopadhyay, A., & Pal, P. K. (2014). Application of artificial neural network for the prediction of laser cladding process characteristics at Taguchi-based optimized condition. *The International Journal of Advanced Manufacturing Technology*, *70*(9), 2151-2158.

[70] Ramarao, M., King, M. F. L., Sivakumar, A., Manikandan, V., Vijayakumar, M., & Subbiah, R. (2022). Optimizing GMAW parameters to achieve high impact strength of the dissimilar weld joints using Taguchi approach. *Materials Today: Proceedings*, *50*, 861-866.

[71] Ambekar, S. D., & Wadhokar, S. R. (2015). Parametric Optimization of Gas metal arc welding process by using Taguchi method on stainless steel AISI 410. *International Journal of Research in Modern Engineering and Emerging Technology*, *3*(1), 1-9.

[72] Selvaraj, D. P., Chandramohan, P., & Mohanraj, M. (2014). Optimization of surface roughness, cutting force and tool wear of nitrogen alloyed duplex stainless steel in a dry turning process using Taguchi method. *Measurement*, *49*, 205-215.

APPENDICES

Appendix A: Optical Micrographs

Appendix B: Tensile test results

Appendix A - Optical micrographs

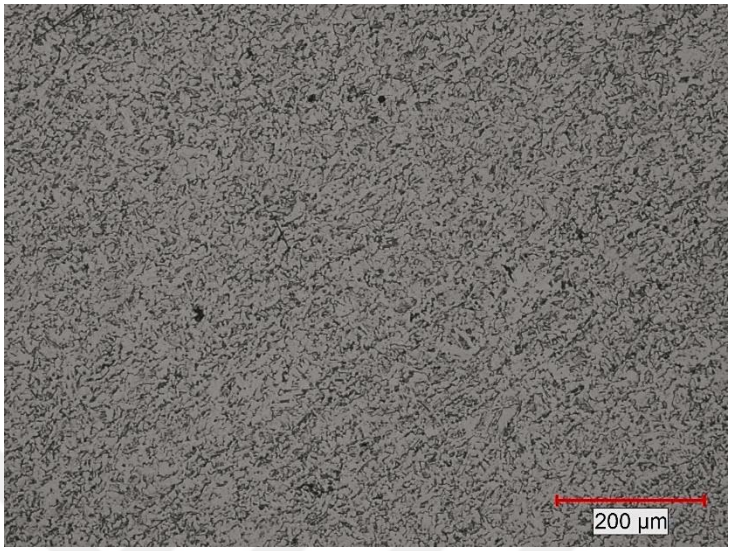

(a)

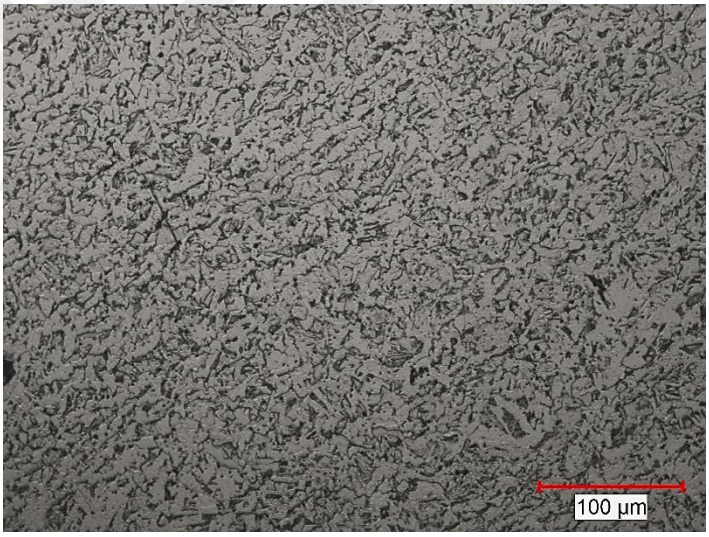

(b)

Figure A.1 Optical microscope image of base metal (St37-2) of sample 9; (a) 100x, (b) 200x

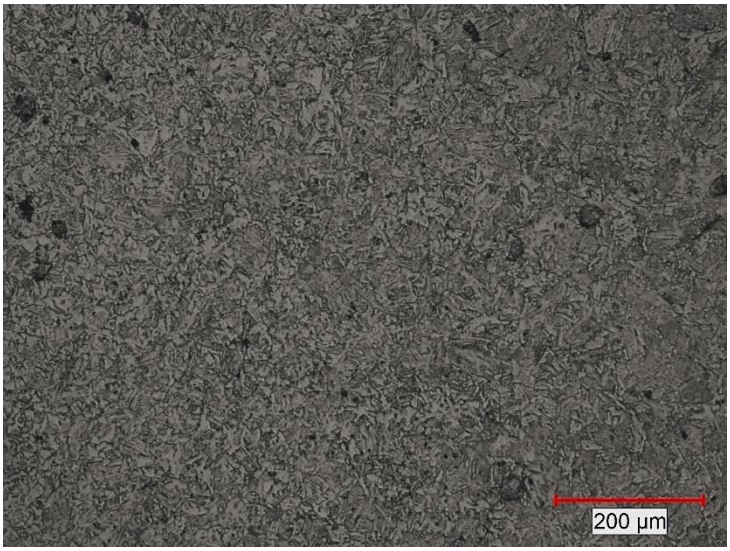

(a)

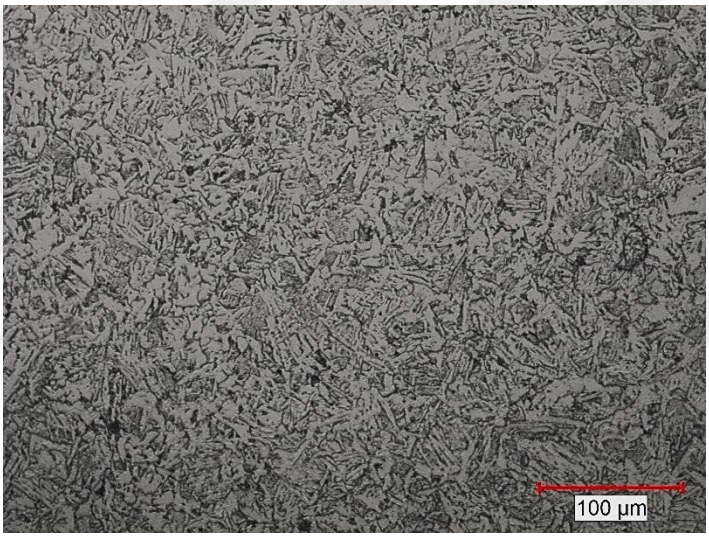

(b)

Figure A.2 Optical microscope image of HAZ region on St37-2 side of sample 9; (a) 100x, (b) 200x

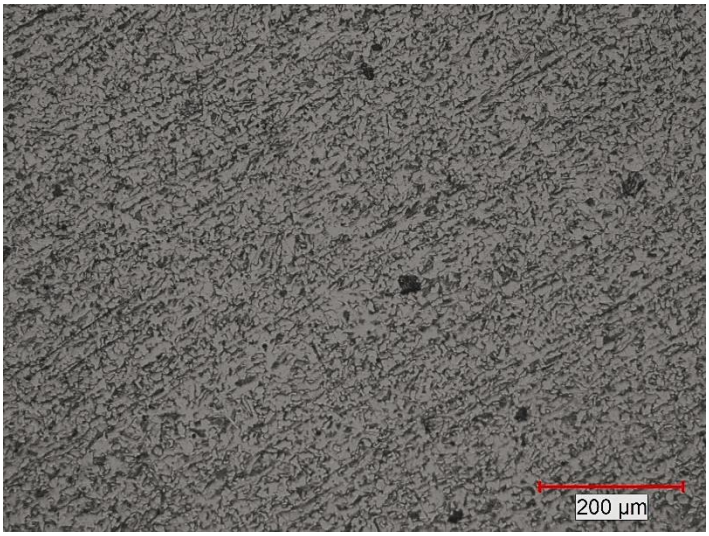

(a)

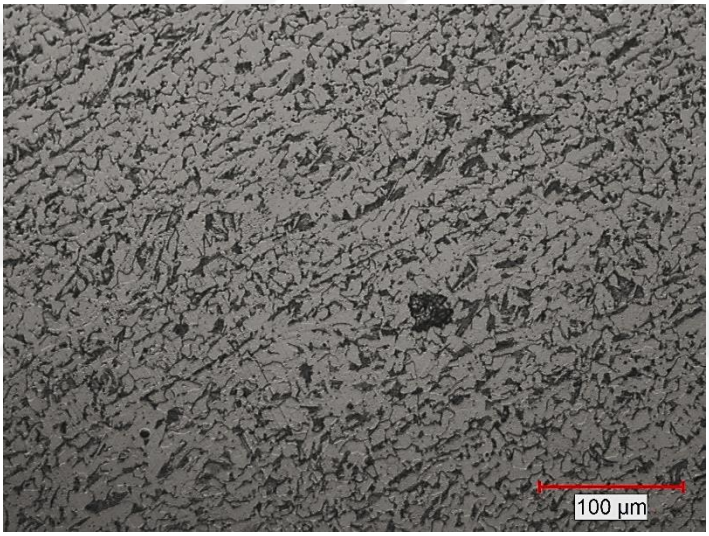

(b)

Figure A.3 Optical microscope image of base metal (St52-3) of sample 9; (a) 100x, (b) 200x

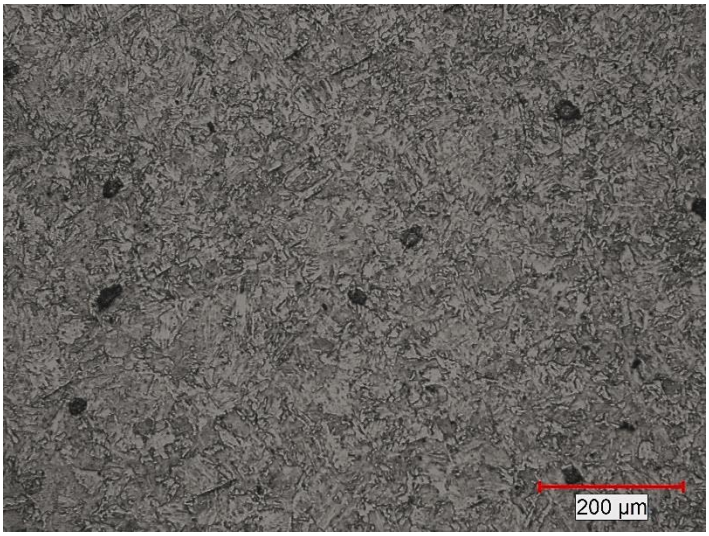

(a)

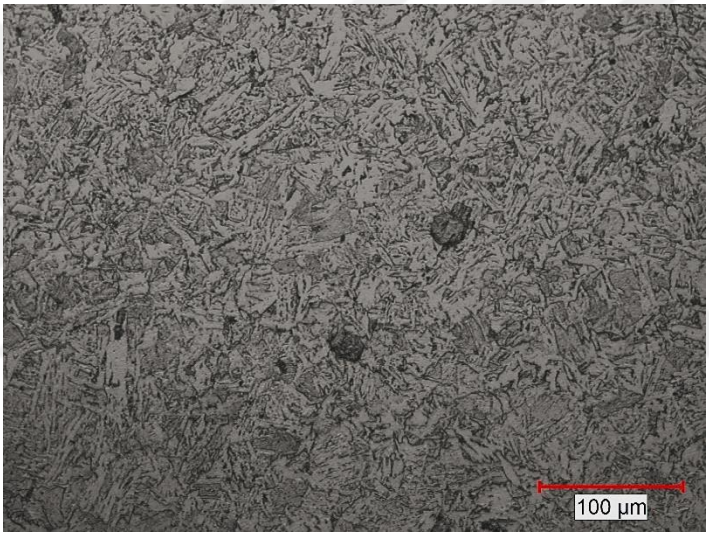

(b)

Figure A.4 Optical microscope image of HAZ region on St52-3 side of sample 9; (a) 100x, (b) 200x

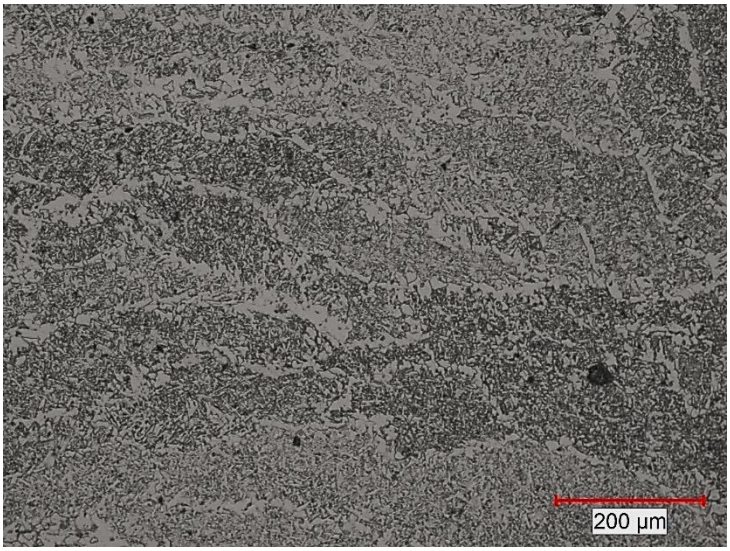

(a)

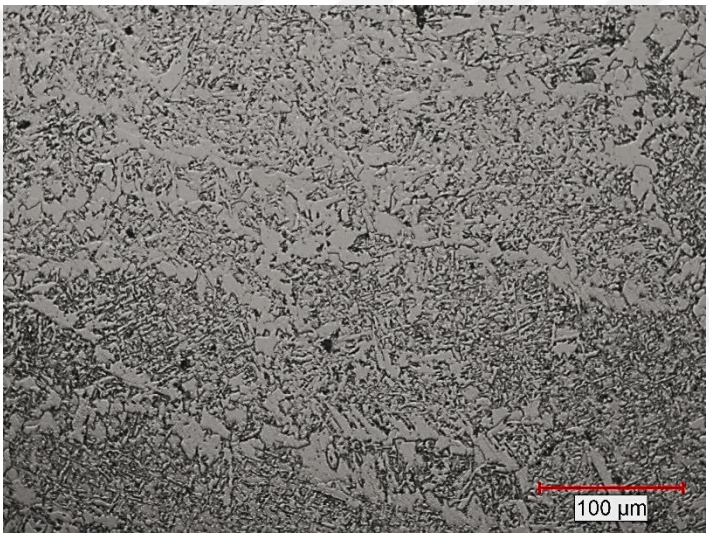

(b)

Figure A.5 Optical microscope image of weld metal of sample 9; (a) 100x, (b) 200x

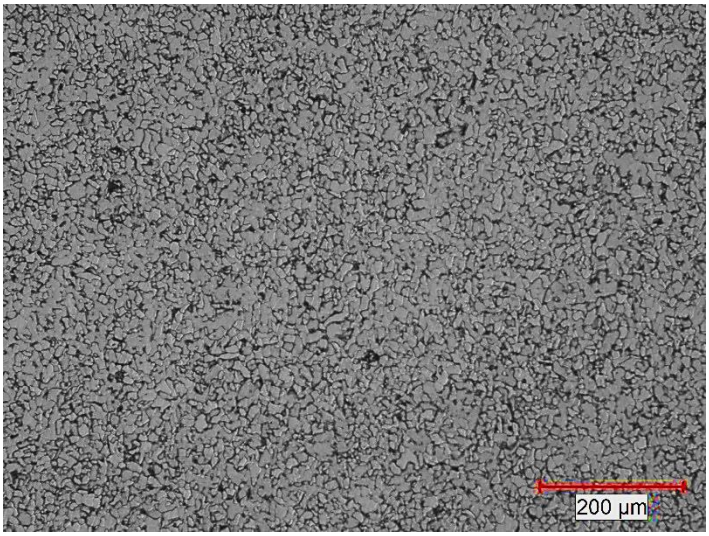

(a)

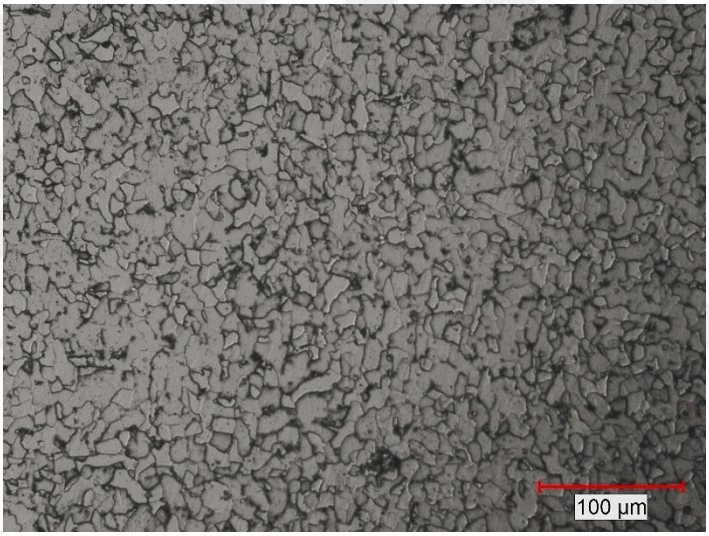

(b)

Figure A.6 Optical microscope image of base metal (St37-2) of sample A; (a) 100x, (b) 200x

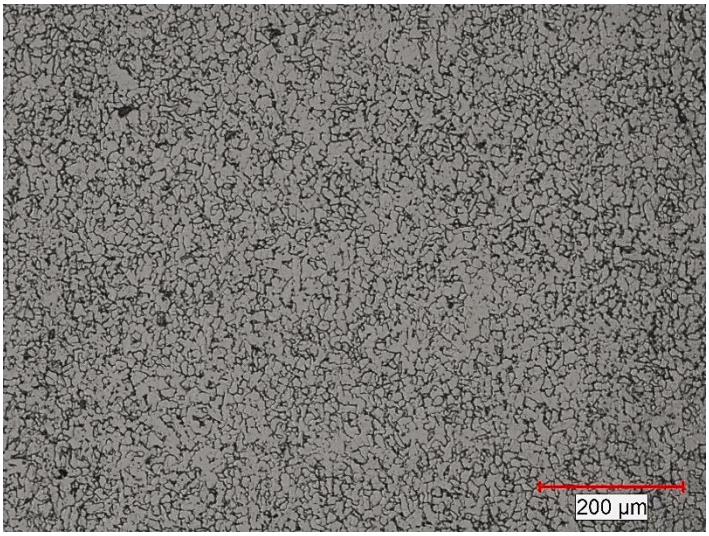

(a)

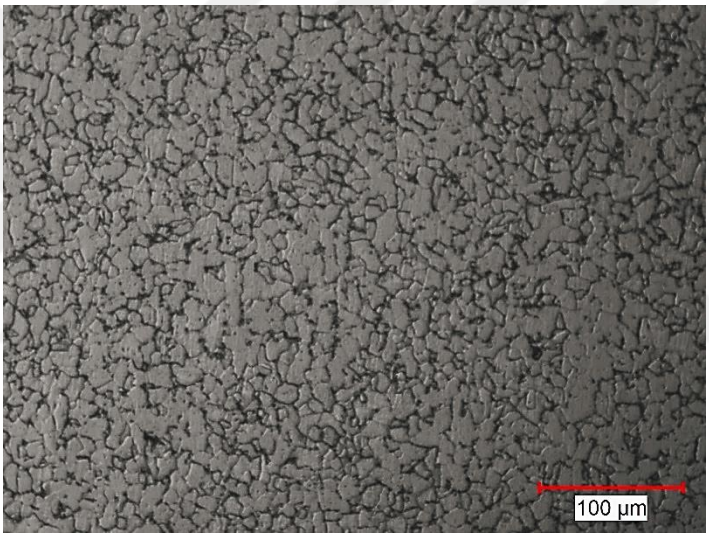

(b)

Figure A.7 Optical microscope image of HAZ region on St37-2 side of sample A; (a) 100x, (b) 200x

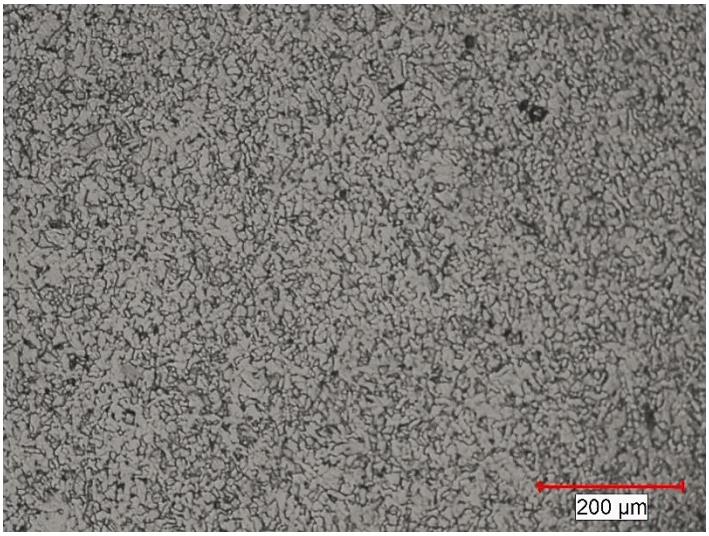

(a)

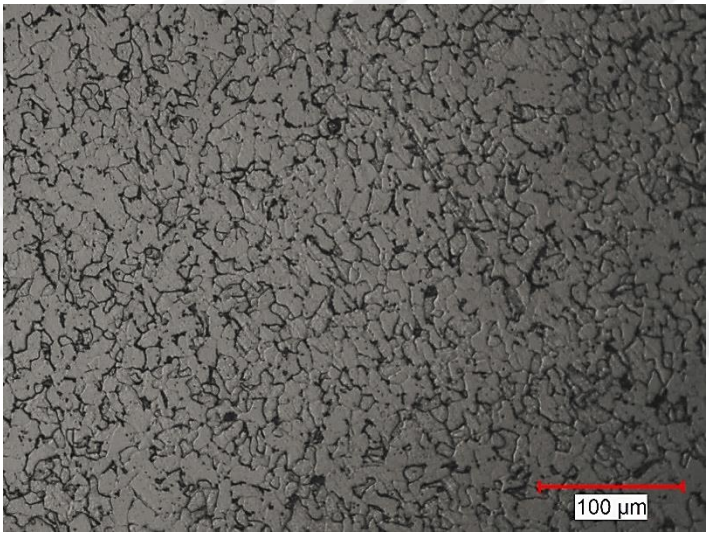

(b)

Figure A.8 Optical microscope image of base metal (St52-3) of sample A; (a) 100x, (b) 200x

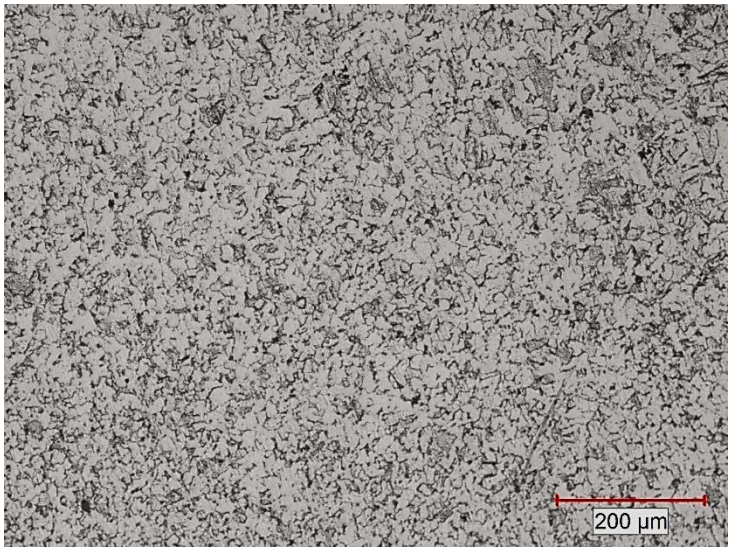

(a)

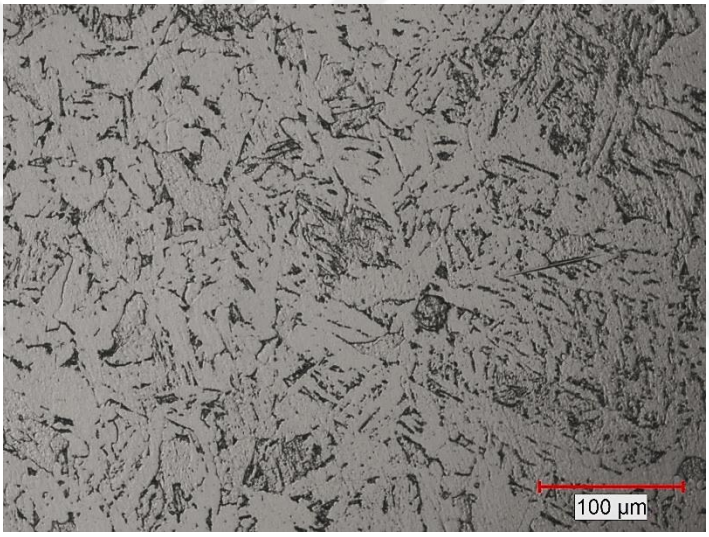

(b)

Figure A.9 Optical microscope image of HAZ region on St52-3 side of sample A; (a) 100x, (b) 200x

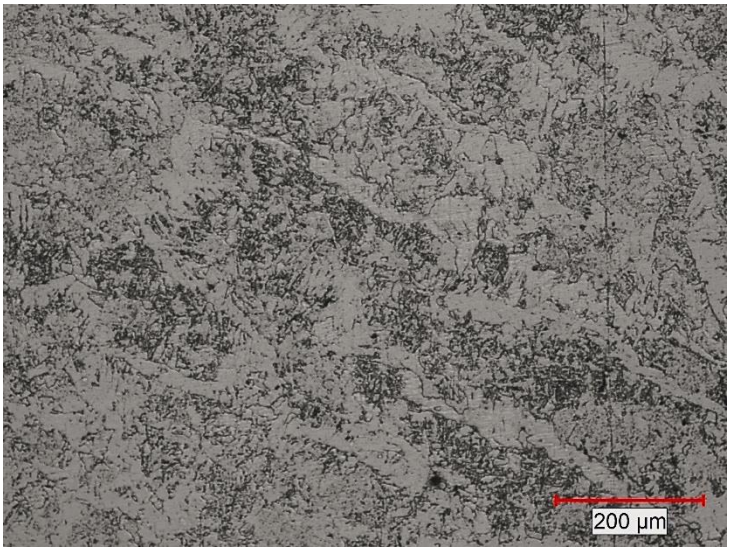

(a)

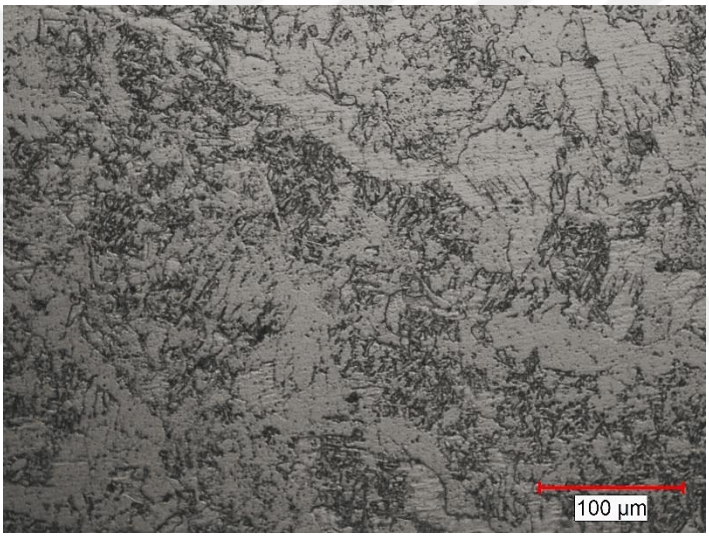

(b)

Figure A.10 Optical microscope image of weld metal of sample A; (a) 100x, (b) 200x

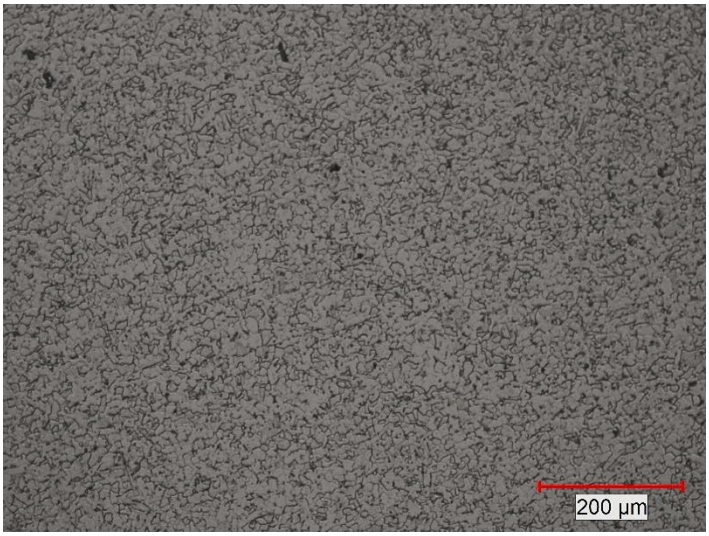

(a)

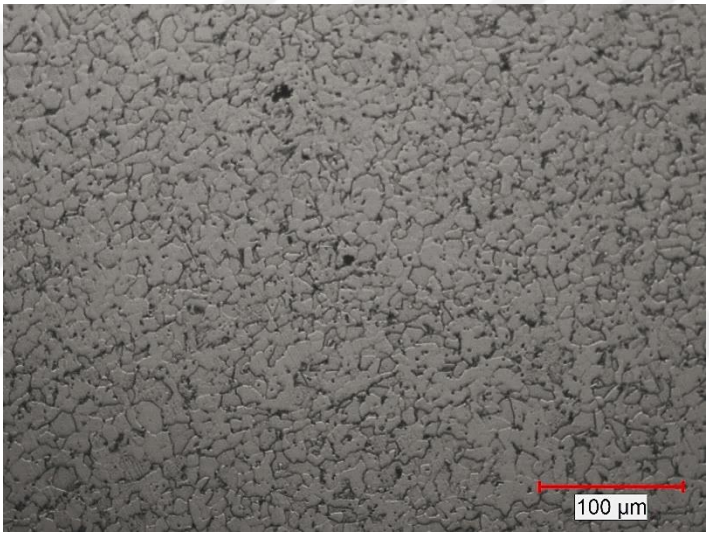

(b)

Figure A.11 Optical microscope image of base metal (St37-2) of sample B; (a) 100x, (b) 200x

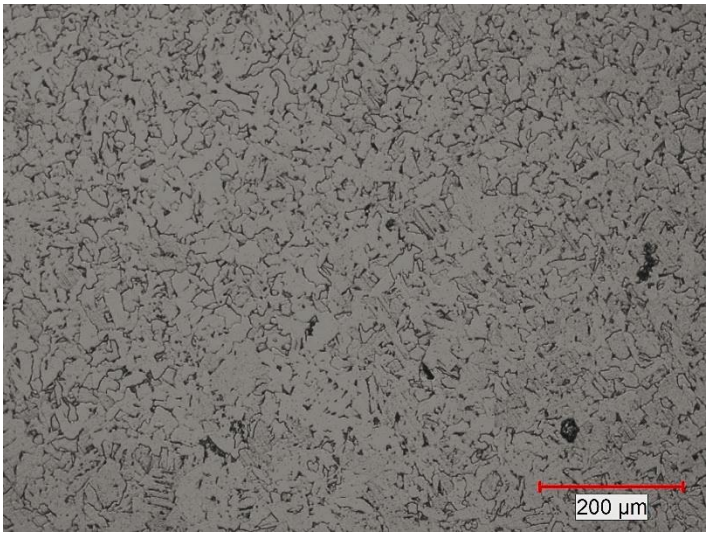

(a)

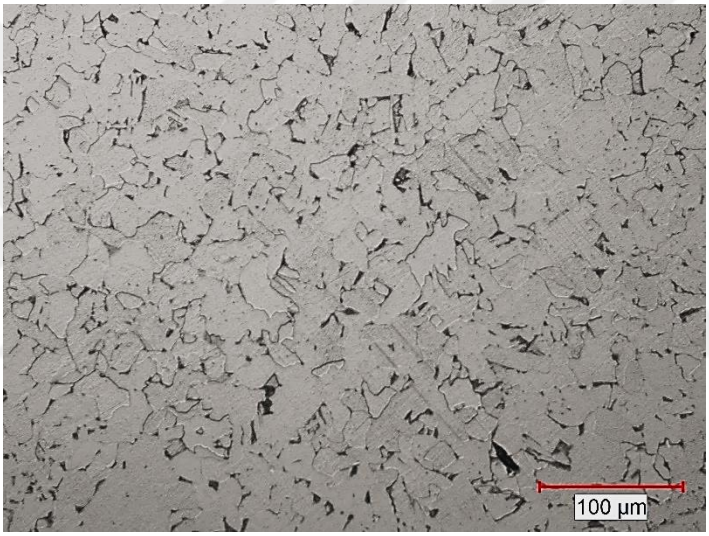

(b)

Figure A.12 Optical microscope image of HAZ region on St37-2 side of sample B; (a) 100x, (b) 200x

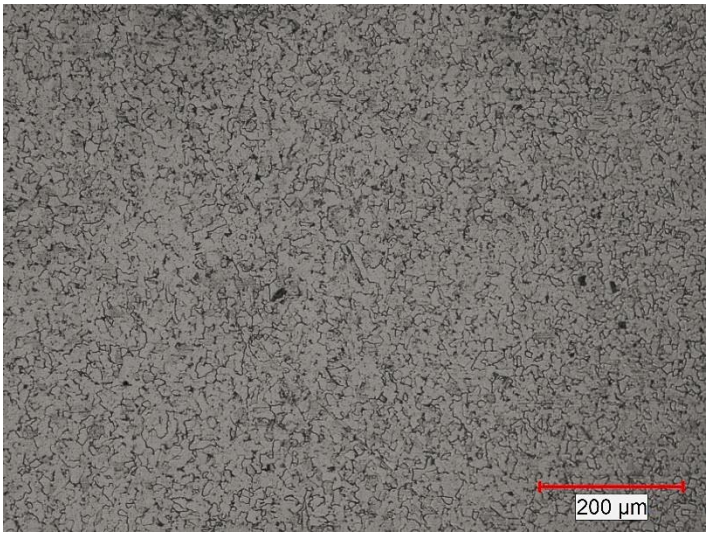

(a)

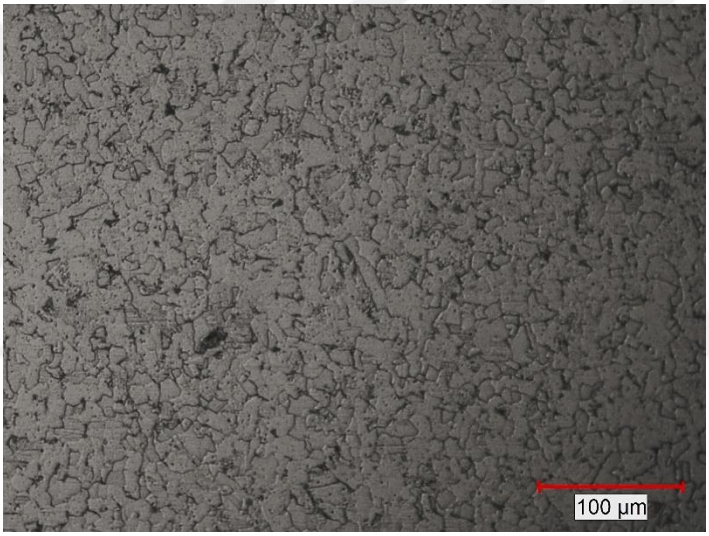

(b)

Figure A.13 Optical microscope image of base metal (St52-3) of sample B; (a) 100x, (b) 200x

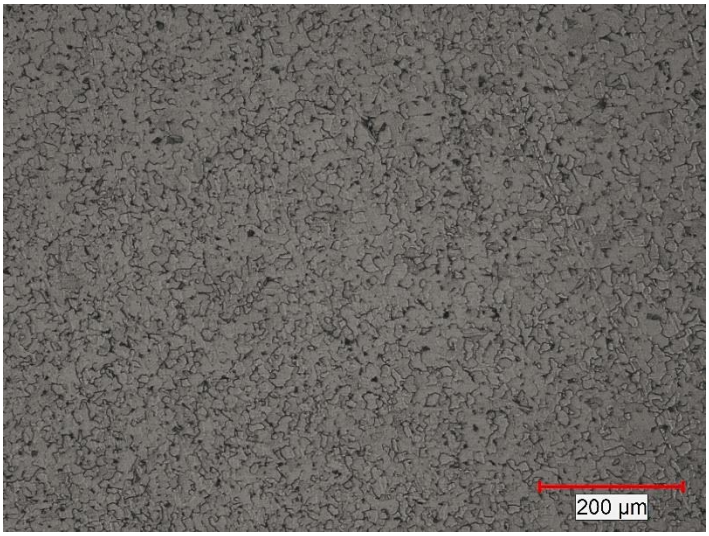

(a)

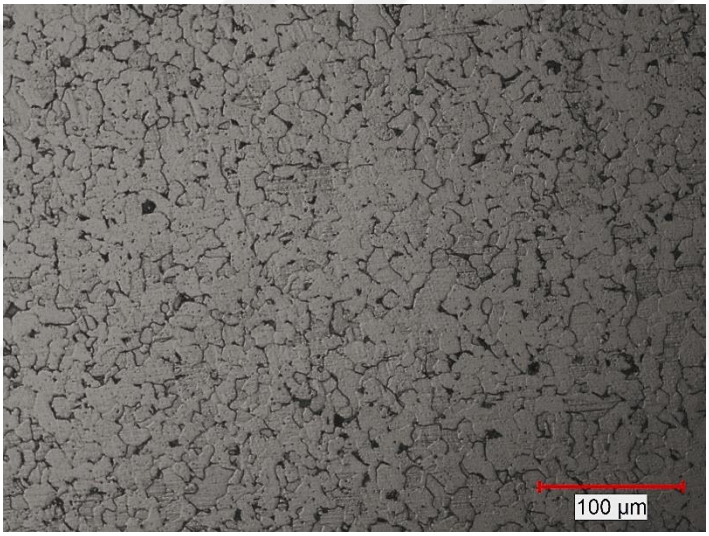

(b)

Figure A.14 Optical microscope image of HAZ region on St52-3 side of sample B; (a) 100x, (b) 200x

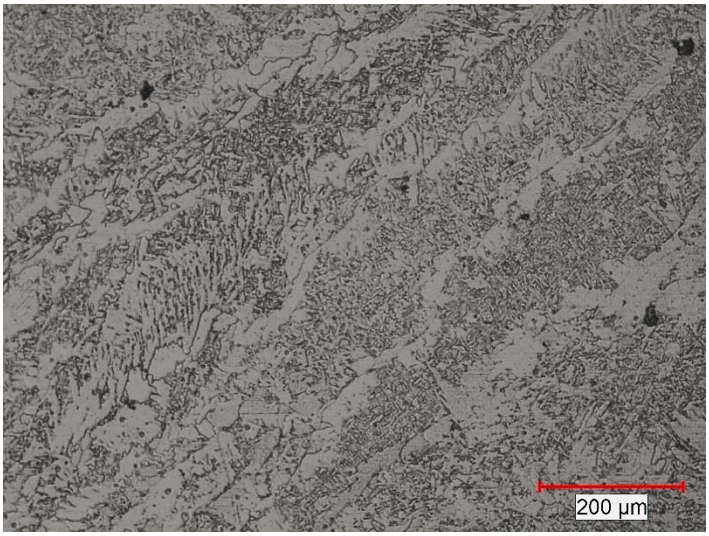

(a)

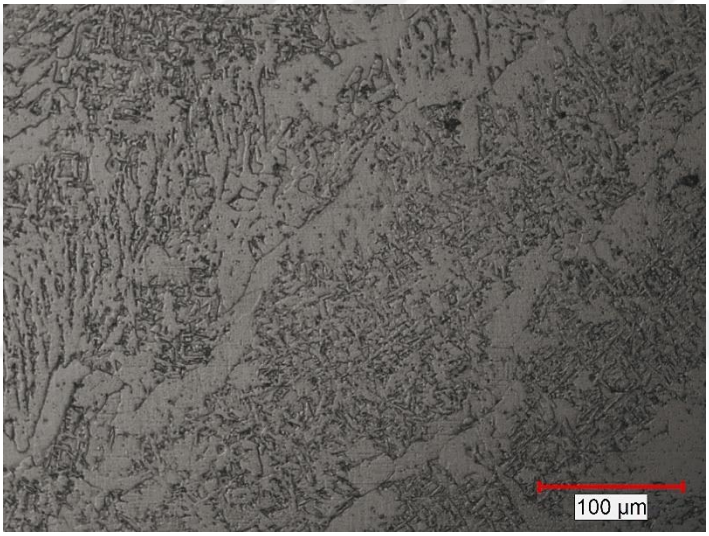

(b)

Figure A.15 Optical microscope image of weld metal of sample B; (a) 100x, (b) 200x

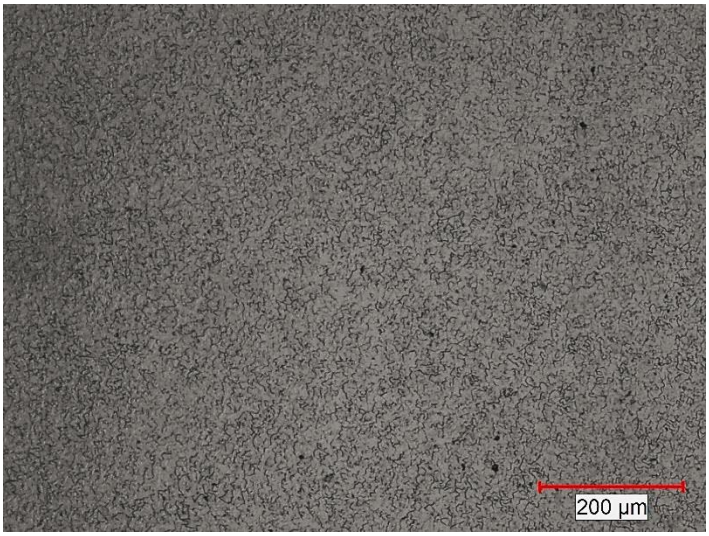

(a)

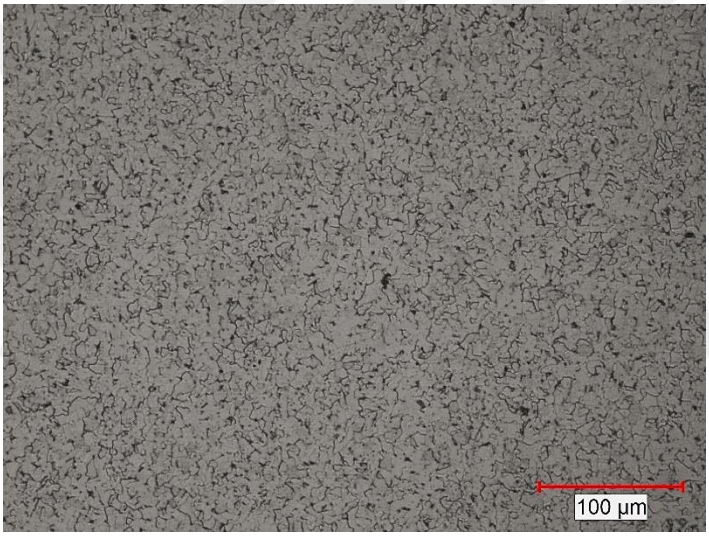

(b)

Figure A.16 Optical microscope image of base metal (St37-2) of sample C; (a) 100x, (b) 200x

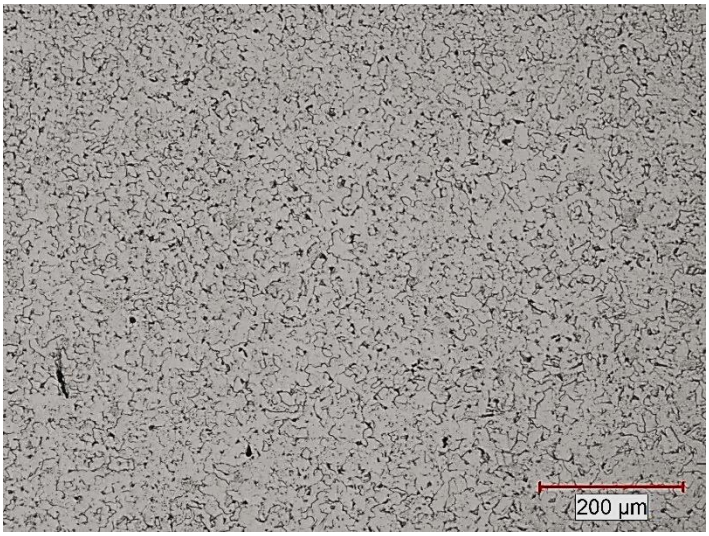

(a)

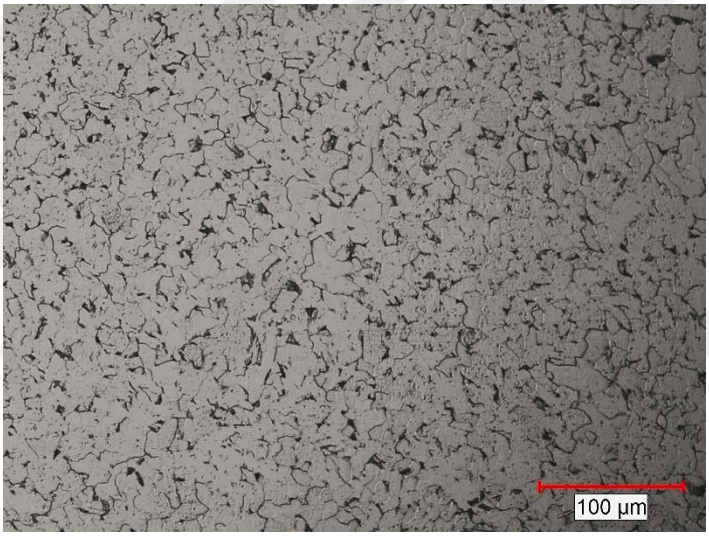

(b)

Figure A.17 Optical microscope image of HAZ region on St37-2 side of sample C; (a) 100x, (b) 200x

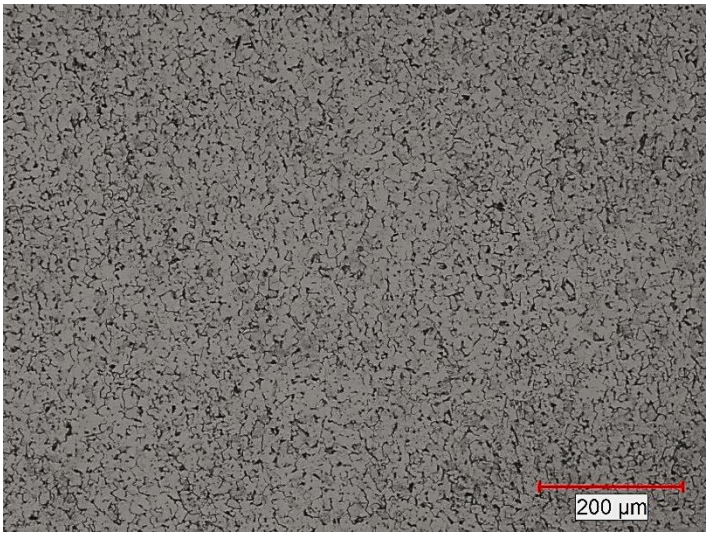

(a)

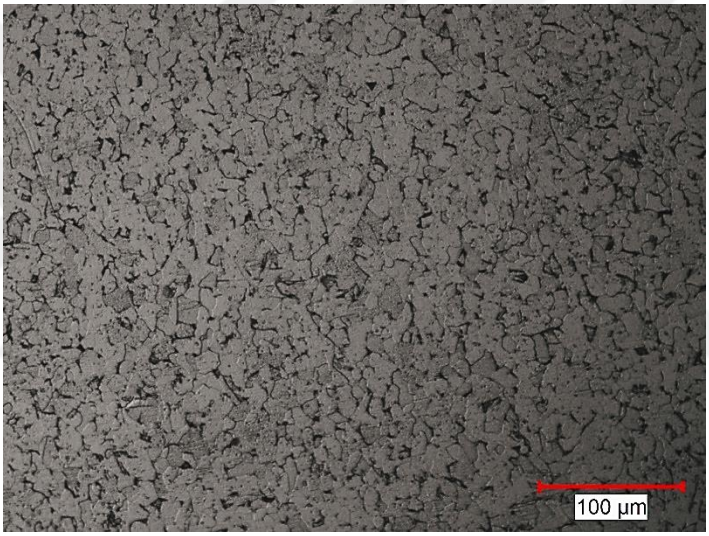

(b)

Figure A.18 Optical microscope image of base metal (St52-3) of sample C; (a) 100x, (b) 200x

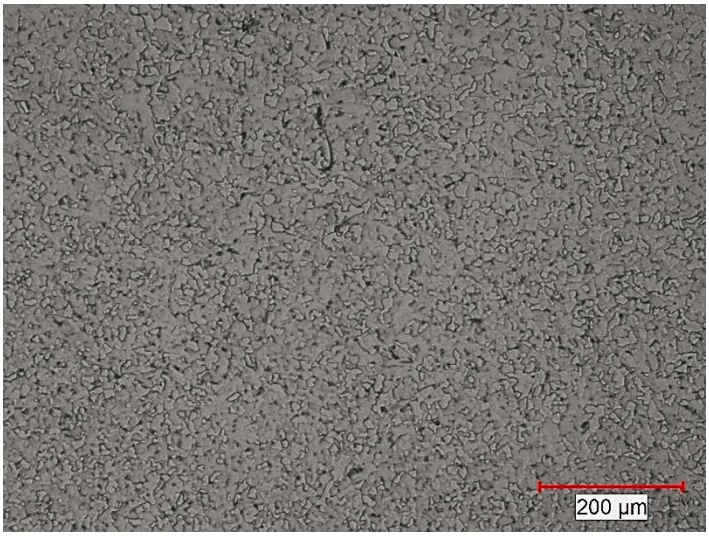

(a)

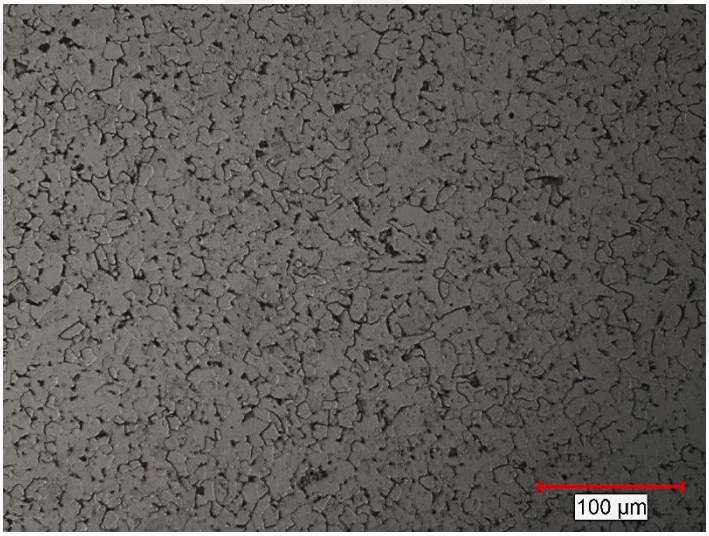

(b)

Figure A.19 Optical microscope image of HAZ region on St52-3 side of sample C; (a) 100x, (b) 200x

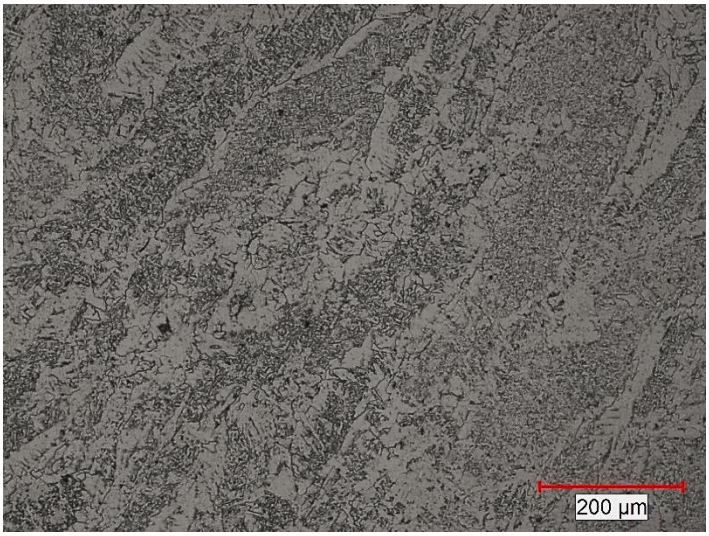

(a)

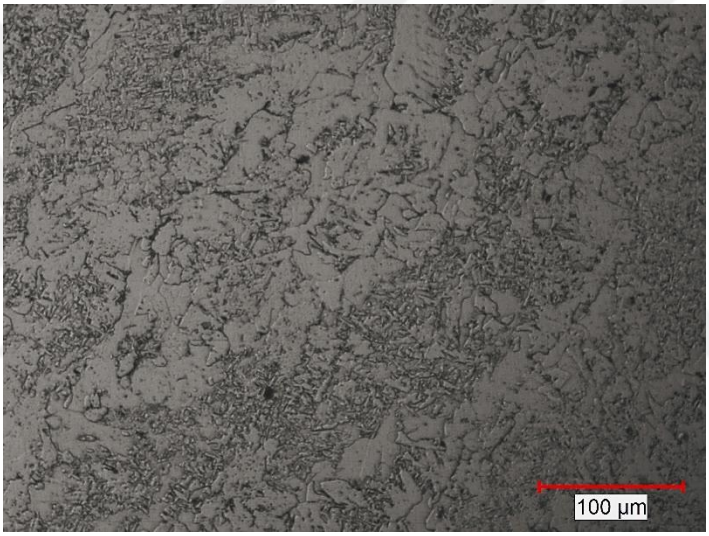

(b)

Figure A.20 Optical microscope image of weld metal of sample C; (a) 100x, (b) 200x

Appendix B - Tensile test results

TCDD

DATEM İŞLETME MÜDÜRLÜĞÜ

DATEM

Zwick / Roell

30.03.22

Test report

Job no. : MT-22-017-1
Test standard : TS EN ISO 6892-1 (Metod B)
Tester : ONDER AKGUNLU
Machine data : Kullanilan Cihazlar: MT-UST-1,MT-KUM-4,MT-SM-4, MT-CC-09
Ortam Sicakligi: 19,4 °C
Nem: % 22,1 RH
Olculen Numune Genisligi: 25,04 mm
Kalinligi: 8.89 mm

Test speeds	:	Method B		Speed, yield point	:	15	MPa/s
Pre-load	:	20	MPa	Test speed	:	0,004	1/s
Speed, E-Modulus	:	30	MPa/s				

Test results:

No.	m_E GPa	$R_{p0.2}$ MPa	R_m MPa	F_m kN	A_{90} %	L_0 mm	S_0 mm²
1	138	269	285	63,52	1,7	90,00	222,61

Series graph:

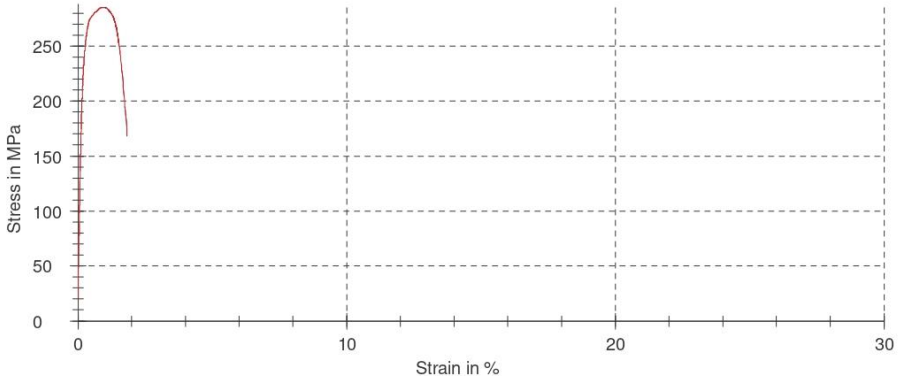

Statistics:

Series n = 1	m_E GPa	$R_{p0.2}$ MPa	R_m MPa	F_m kN	A_{90} %	L_0 mm	S_0 mm²
$\bar{x}$	138	269	285	63,52	1,7	90,00	222,61
s	-	-	-	-	-	-	-
v	-	-	-	-	-	-	-

MT-22-017-1.zs2 **Page 1/1**

Figure B.1 Tensile test result of A1B1C1

DATEM İŞLETME MÜDÜRLÜĞÜ

Zwick / Roell

30.03.22

Test report

Job no. : MT-22-017-2
Test standard : TS EN ISO 6892-1 (Metod B)
Tester : ONDER AKGUNLU
Machine data : Kullanilan Cihazlar: MT-UST-1,MT-KUM-4,MT-SM-4, MT-CC-09
Ortam Sicakligi: 19,5℃
Nem: % 23 RH
Olculen Numune Genisligi: 25,01 mm
Kalinligi: 9.21 mm

Test speeds	: Method B		Speed, yield point	: 15	MPa/s
Pre-load	: 20	MPa	Speed in the yield range	: 0,00025	1/s
Speed, E-Modulus	: 30	MPa/s	Test speed	: 0,004	1/s

Test results:

No.	m_E GPa	R_{eH} MPa	R_{eL} MPa	R_m MPa	F_m kN	A_{90} %	L_0 mm	S_0 mm²
1	230	391	382	457	105,34	4,8	90,00	230,34

Series graph:

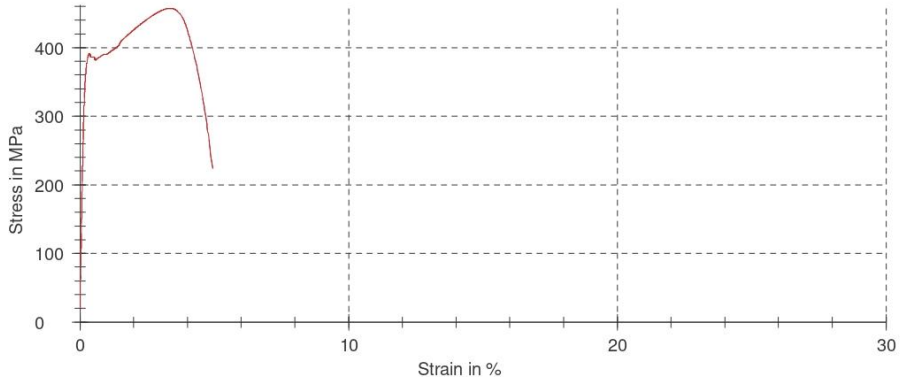

Statistics:

Series n = 1	m_E GPa	R_{eH} MPa	R_{eL} MPa	R_m MPa	F_m kN	A_{90} %	L_0 mm	S_0 mm²
$\bar{x}$	230	391	382	457	105,34	4,8	90,00	230,34
s	-	-	-	-	-	-	-	-
v	-	-	-	-	-	-	-	-

MT-22-017-2.zs2 **Page 1/1**

Figure B.2 Tensile test result of A1B2C2

DATEM İŞLETME MÜDÜRLÜĞÜ

Zwick / Roell

31.03.22

Test report

Job no. : MT-22-017-3
Test standard : TS EN ISO 6892-1 (Metod B)
Tester : ONDER AKGUNLU
Machine data : Kullanilan Cihazlar: MT-UST-1,MT-KUM-4,MT-SM-4, MT-CC-09
Ortam Sicakligi: 19,4 °C
Nem: % 27,5 RH
Olculen Numune Genisligi: 25,00 mm
Kalinligi: 8.17 mm

Test speeds	: Method B		Speed, yield point	: 15	MPa/s
Pre-load	: 20	MPa	Speed in the yield range	: 0,00025	1/s
Speed, E-Modulus	: 30	MPa/s	Test speed	: 0,004	1/s

Test results:

No.	m_E GPa	R_{eH} MPa	R_{eL} MPa	R_m MPa	F_m kN	A_{90} %	L_0 mm	S_0 mm²
1	218	448	441	470	95,98	2,8	90,00	204,25

Series graph:

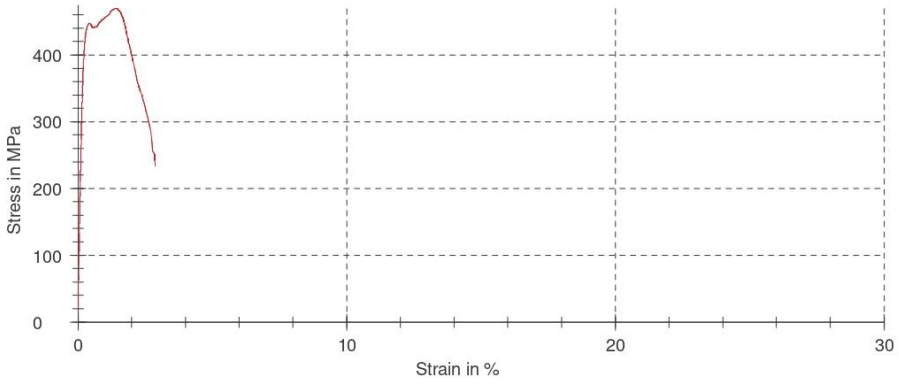

Statistics:

Series n = 1	m_E GPa	R_{eH} MPa	R_{eL} MPa	R_m MPa	F_m kN	A_{90} %	L_0 mm	S_0 mm²
$\bar{x}$	218	448	441	470	95,98	2,8	90,00	204,25
s	-	-	-	-	-	-	-	-
v	-	-	-	-	-	-	-	-

MT-22-017-3.ZP2

Page 1/1

Figure B.3 Tensile test result of A1B3C3

DATEM İŞLETME MÜDÜRLÜĞÜ

Zwick / Roell

31.03.22

Test report

Job no.	:	MT-22-017-4
Test standard	:	TS EN ISO 6892-1 (Metod B)
Tester	:	ONDER AKGUNLU
Machine data	:	Kullanilan Cihazlar: MT-UST-1,MT-KUM-4,MT-SM-4, MT-CC-09 Ortam Sicakligi: 19,4 °C Nem: % 27,5 RH Olculen Numune Genisligi: 25,01 mm Kalinligi: 9.11 mm

Test speeds	:	Method B		Speed, yield point	:	15	MPa/s
Pre-load	:	20	MPa	Test speed	:	0,004	1/s
Speed, E-Modulus	:	30	MPa/s				

Test results:

No.	m_E GPa	$R_{p0.2}$ MPa	R_m MPa	F_m kN	A_{90} %	L_0 mm	S_0 mm²
1	209	376	403	91,80	3,2	90,00	227,84

Series graph:

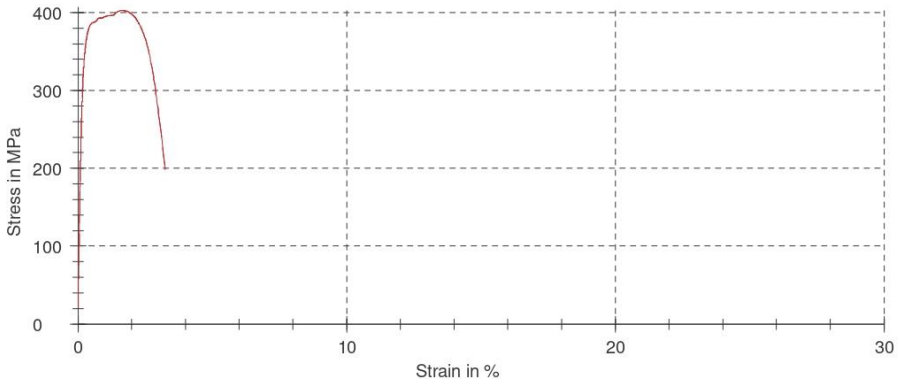

Statistics:

Series n = 1	m_E GPa	$R_{p0.2}$ MPa	R_m MPa	F_m kN	A_{90} %	L_0 mm	S_0 mm²
$\bar{x}$	209	376	403	91,80	3,2	90,00	227,84
s	-	-	-	-	-	-	-
v	-	-	-	-	-	-	-

MT-22-017-4.zs2

Page 1/1

Figure B.4 Tensile test result of A2B1C2

DATEM İŞLETME MÜDÜRLÜĞÜ

Zwick / Roell

31.03.22

Test report

Job no. : MT-22-017-5
Test standard : TS EN ISO 6892-1 (Metod B)
Tester : ONDER AKGUNLU
Machine data : Kullanilan Cihazlar: MT-UST-1,MT-KUM-4,MT-SM-4, MT-CC-09
Ortam Sicakligi: 19,4 ℃
Nem: % 27,5 RH
Olculen Numune Genisligi: 25,07 mm
Kalinligi: 9.35 mm

Test speeds	:	Method B	Speed, yield point	:	15	MPa/s
Pre-load	:	20 MPa	Test speed	:	0,004	1/s
Speed, E-Modulus	:	30 MPa/s				

Test results:

No.	m_E GPa	$R_{p0.2}$ MPa	R_m MPa	F_m kN	A_{90} %	L_0 mm	S_0 mm²
1	196	419	453	106,21	3,3	90,00	234,40

Series graph:

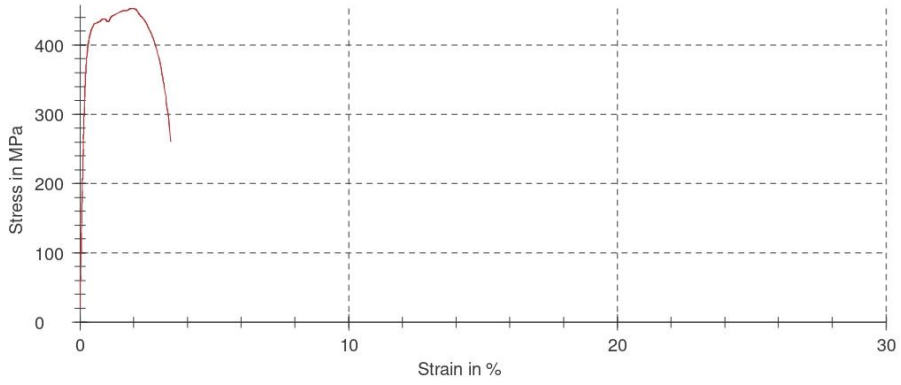

Statistics:

Series n = 1	m_E GPa	$R_{p0.2}$ MPa	R_m MPa	F_m kN	A_{90} %	L_0 mm	S_0 mm²
$\bar{x}$	196	419	453	106,21	3,3	90,00	234,40
s	-	-	-	-	-	-	-
v	-	-	-	-	-	-	-

MT-22-017-5.zs2 **Page 1/1**

Figure B.5 Tensile test result of A2B2C3

TCDD

DATEM İŞLETME MÜDÜRLÜĞÜ

DATEM

Zwick / Roell

31.03.22

Test report

Job no. : MT-22-017-6
Test standard : TS EN ISO 6892-1 (Metod B)
Tester : ONDER AKGUNLU
Machine data : Kullanilan Cihazlar: MT-UST-1,MT-KUM-4,MT-SM-4, MT-CC-09
Ortam Sicakligi: 19,4 °C
Nem: % 27,5 RH
Olculen Numune Genisligi: 25,01 mm
Kalinligi: 8.43 mm

Test speeds	: Method B		Speed, yield point	: 15	MPa/s
Pre-load	: 20	MPa	Speed in the yield range	: 0,00025	1/s
Speed, E-Modulus	: 30	MPa/s	Test speed	: 0,004	1/s

Test results:

No.	m_E GPa	R_{eH} MPa	R_{eL} MPa	R_m MPa	F_m kN	A_{90} %	L_0 mm	S_0 mm²
1	210	395	392	519	109,51	8,3	90,00	210,83

Series graph:

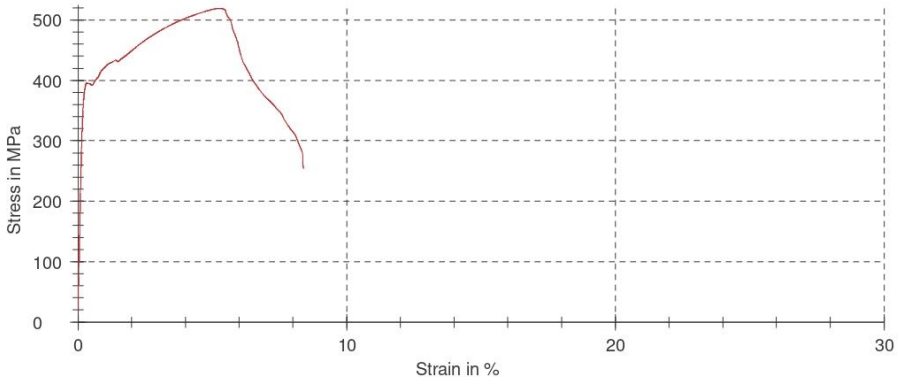

Statistics:

Series n = 1	m_E GPa	R_{eH} MPa	R_{eL} MPa	R_m MPa	F_m kN	A_{90} %	L_0 mm	S_0 mm²
$\bar{x}$	210	395	392	519	109,51	8,3	90,00	210,83
s	-	-	-	-	-	-	-	-
v	-	-	-	-	-	-	-	-

MT-22-017-6.zs2 **Page 1/1**

Figure B.6 Tensile test result of A2B3C1

TCDD

DATEM İŞLETME MÜDÜRLÜĞÜ

DATEM

Zwick / Roell

31.03.22

Test report

Job no. : MT-22-017-7
Test standard : TS EN ISO 6892-1 (Metod B)
Tester : ONDER AKGUNLU
Machine data : Kullanilan Cihazlar: MT-UST-1,MT-KUM-4,MT-SM-4, MT-CC-09
Ortam Sicakligi: 19,4 ℃
Nem: % 27,5 RH
Olculen Numune Genisligi: 25,01 mm
Kalinligi: 8.65 mm

Test speeds	: Method B		Speed, yield point	: 15	MPa/s
Pre-load	: 20	MPa	Speed in the yield range	: 0,00025	1/s
Speed, E-Modulus	: 30	MPa/s	Test speed	: 0,004	1/s

Test results:

No.	m_E GPa	R_{eH} MPa	R_{eL} MPa	R_m MPa	F_m kN	A_{90} %	L_0 mm	S_0 mm²
1	210	386	379	483	104,49	5,3	90,00	216,34

Series graph:

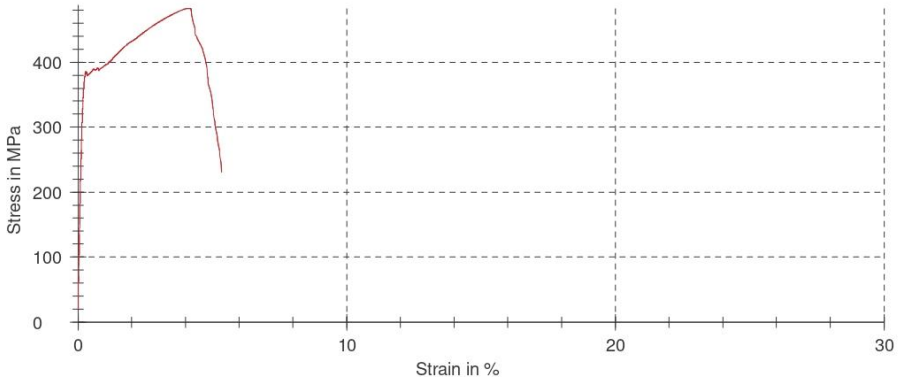

Statistics:

Series n = 1	m_E GPa	R_{eH} MPa	R_{eL} MPa	R_m MPa	F_m kN	A_{90} %	L_0 mm	S_0 mm²
$\bar{x}$	210	386	379	483	104,49	5,3	90,00	216,34
s	-	-	-	-	-	-	-	-
v	-	-	-	-	-	-	-	-

MT-22-017-7.zs2

Page 1/1

Figure B.7 Tensile test result of A3B1C3

DATEM İŞLETME MÜDÜRLÜĞÜ

Zwick / Roell

31.03.22

Test report

Job no.	:	MT-22-017-8
Test standard	:	TS EN ISO 6892-1 (Metod B)
Tester	:	ONDER AKGUNLU
Machine data	:	Kullanilan Cihazlar: MT-UST-1,MT-KUM-4,MT-SM-4, MT-CC-09 Ortam Sicakligi: 19,4 °C Nem: % 27,5 RH Olculen Numune Genisligi: 25,05 mm Kalinligi: 9.30 mm

Test speeds	:	Method B		Speed, yield point	:	15	MPa/s
Pre-load	:	20	MPa	Test speed	:	0,004	1/s
Speed, E-Modulus	:	30	MPa/s				

Test results:

No.	m_E GPa	$R_{p0.2}$ MPa	R_m MPa	F_m kN	A_{90} %	L_0 mm	S_0 mm²
1	167	308	324	75,52	2,1	90,00	232,97

Series graph:

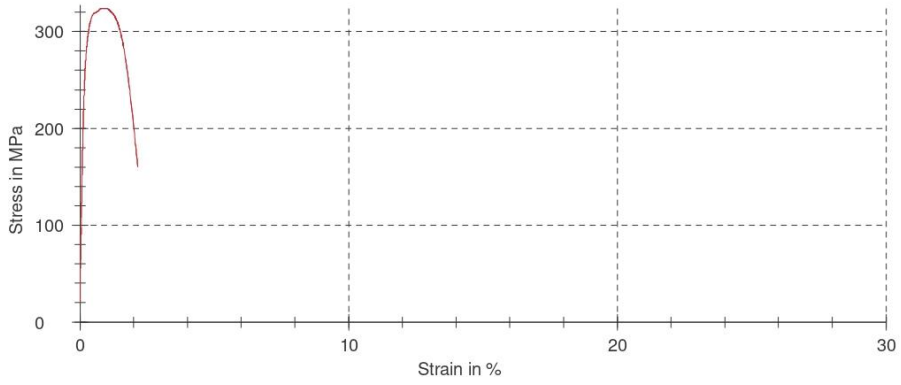

Statistics:

Series n = 1	m_E GPa	$R_{p0.2}$ MPa	R_m MPa	F_m kN	A_{90} %	L_0 mm	S_0 mm²
$\bar{x}$	167	308	324	75,52	2,1	90,00	232,97
s	-	-	-	-	-	-	-
v	-	-	-	-	-	-	-

MT-22-017-8.zs2

Page 1/1

Figure B.8 Tensile test result of A3B2C1

TCDD

DATEM İŞLETME MÜDÜRLÜĞÜ

DATEM

Zwick / Roell

31.03.22

Test report

Job no.	:	MT-22-017-9
Test standard	:	TS EN ISO 6892-1 (Metod B)
Tester	:	ONDER AKGUNLU
Machine data	:	Kullanilan Cihazlar: MT-UST-1,MT-KUM-4,MT-SM-4, MT-CC-09
		Ortam Sicakligi: 19,4 °C
		Nem: % 27,5 RH
		Olculen Numune Genisligi: 25,01 mm
		Kalinligi: 7.81 mm

Test speeds	:	Method B		Speed, yield point	: 15	MPa/s
Pre-load	:	20	MPa	Speed in the yield range	: 0,00025	1/s
Speed, E-Modulus	:	30	MPa/s	Test speed	: 0,004	1/s

Test results:

No.	m_E GPa	R_{eH} MPa	R_{eL} MPa	R_m MPa	F_m kN	A_{90} %	L_0 mm	S_0 mm²
1	236	375	367	529	103,26	17,5	90,00	195,33

Series graph:

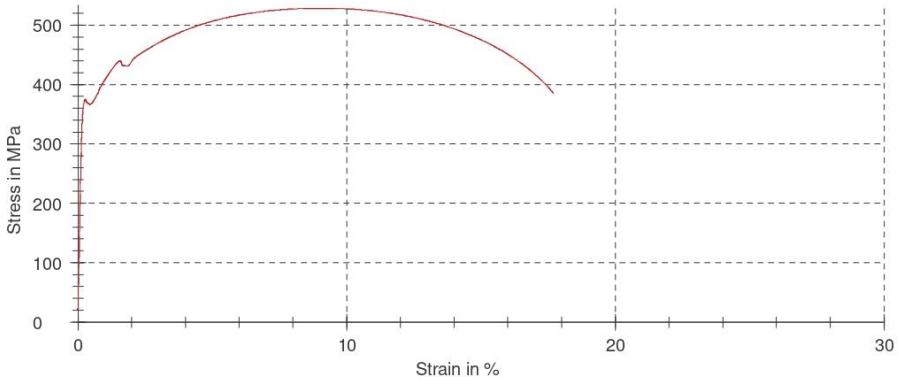

Statistics:

Series n = 1	m_E GPa	R_{eH} MPa	R_{eL} MPa	R_m MPa	F_m kN	A_{90} %	L_0 mm	S_0 mm²
$\bar{x}$	236	375	367	529	103,26	17,5	90,00	195,33
s	-	-	-	-	-	-	-	-
v	-	-	-	-	-	-	-	-

MT-22-017-9.zs2

Page 1/1

Figure B.9 Tensile test result of A3B3C2

DATEM İŞLETME MÜDÜRLÜĞÜ

Zwick / Roell

26.10.22

Test report

Job no.	:	MT-22-042-2
Test standard	:	TS EN ISO 6892-1 (Metod B)
Tester	:	ONDER AKGUNLU
Machine data	:	Kullanilan Cihazlar: MT-UST-1,MT-KUM-4,MT-SM-4, MT-CC-09
		Ortam Sicakligi: 19,9℃
		Nem: %33,8 RH
		Olculen Numune Genisligi: 25,01 mm
		Kalinligi: 7,92 mm

Test speeds	:	Method B		Speed, yield point	: 15	MPa/s
Pre-load	:	20	MPa	Speed in the yield range	: 0,00025	1/s
Speed, E-Modulus	:	30	MPa/s	Test speed	: 0,004	1/s

Test results:

No.	m_E GPa	R_{eH} MPa	R_{eL} MPa	R_m MPa	F_m kN	A_{90} %	L_0 mm	S_0 mm²
1	220	358	342	436	86,40	25,0	90,00	198,08

Series graph:

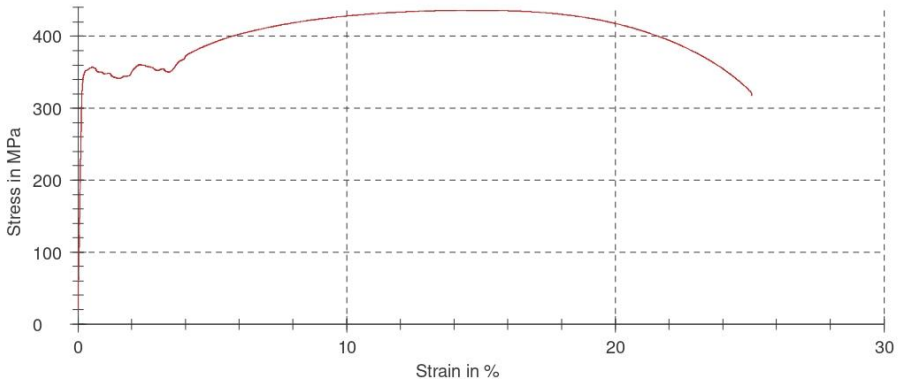

Statistics:

Series n = 1	m_E GPa	R_{eH} MPa	R_{eL} MPa	R_m MPa	F_m kN	A_{90} %	L_0 mm	S_0 mm²
$\bar{x}$	220	358	342	436	86,40	25,0	90,00	198,08
s	-	-	-	-	-	-	-	-
v	-	-	-	-	-	-	-	-

MT-22-042-2.zs2

Page 1/1

Figure B.10 Tensile test result of sample A

DATEM İŞLETME MÜDÜRLÜĞÜ

Zwick / Roell

27.10.22

Test report

Job no.	:	MT-22-042-3
Test standard	:	TS EN ISO 6892-1 (Metod B)
Tester	:	ONDER AKGUNLU
Machine data	:	Kullanilan Cihazlar: MT-UST-1,MT-KUM-4,MT-SM-4, MT-CC-09
		Ortam Sicakligi: 20,1 ℃
		Nem: %38,6 RH
		Olculen Numune Genisligi: 25,01 mm
		Kalinligi: 8,01 mm

Test speeds	:	Method B		Speed, yield point	: 15	MPa/s
Pre-load	:	20	MPa	Speed in the yield range	: 0,00025	1/s
Speed, E-Modulus	:	30	MPa/s	Test speed	: 0,004	1/s

Test results:

No.	m_E GPa	R_{eH} MPa	R_{eL} MPa	R_m MPa	F_m kN	A_{90} %	L_0 mm	S_0 mm²
1	206	352	342	430	86,05	25,3	90,00	200,33

Series graph:

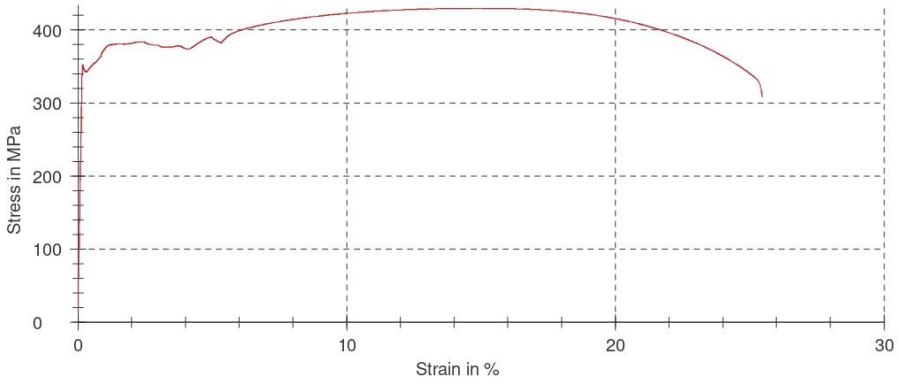

Statistics:

Series n = 1	m_E GPa	R_{eH} MPa	R_{eL} MPa	R_m MPa	F_m kN	A_{90} %	L_0 mm	S_0 mm²
$\bar{x}$	206	352	342	430	86,05	25,3	90,00	200,33
s	-	-	-	-	-	-	-	-
v	-	-	-	-	-	-	-	-

MT-22-042-3.zs2

Page 1/1

Figure B.11 Tensile test result of sample B

DATEM İŞLETME MÜDÜRLÜĞÜ

Zwick / Roell

27.10.22

Test report

Job no.	:	MT-22-042-4
Test standard	:	TS EN ISO 6892-1 (Metod B)
Tester	:	ONDER AKGUNLU
Machine data	:	Kullanilan Cihazlar: MT-UST-1,MT-KUM-4,MT-SM-4, MT-CC-09
		Ortam Sicakligi: 20,1 ℃
		Nem: %38,6 RH
		Olculen Numune Genisligi: 25,00 mm
		Kalinligi: 8,01 mm

Test speeds	:	Method B		Speed, yield point	: 15	MPa/s
Pre-load	:	20	MPa	Speed in the yield range	: 0,00025	1/s
Speed, E-Modulus	:	30	MPa/s	Test speed	: 0,004	1/s

Test results:

No.	m_E GPa	R_{eH} MPa	R_{eL} MPa	R_m MPa	F_m kN	A_{90} %	L_0 mm	S_0 mm²
1	223	345	332	415	83,07	29,3	90,00	200,25

Series graph:

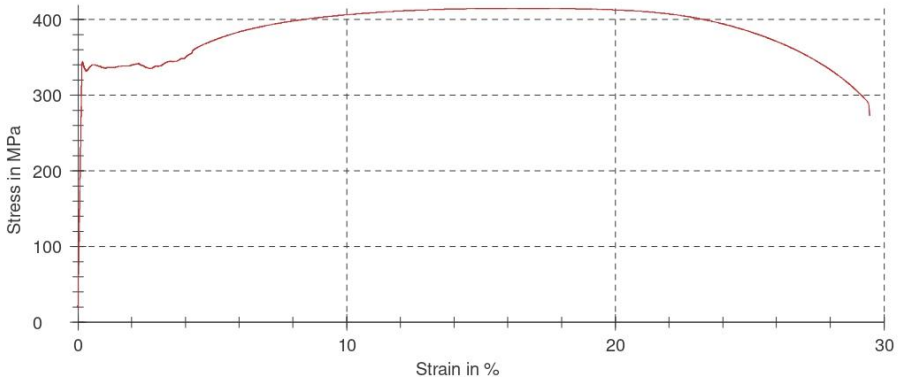

Statistics:

Series n = 1	m_E GPa	R_{eH} MPa	R_{eL} MPa	R_m MPa	F_m kN	A_{90} %	L_0 mm	S_0 mm²
$\bar{x}$	223	345	332	415	83,07	29,3	90,00	200,25
s	-	-	-	-	-	-	-	-
v	-	-	-	-	-	-	-	-

MT-22-042-4.zs2

Page 1/1

Figure B.12 Tensile test result of sample C

CURRICULUM VITAE

PERSONAL INFORMATION

Name Surname **:** Yasin SANCAR
Date of Birth **:**
E-mail **:**

EDUCATION

Bachelor **:** Ankara Yıldırım Beyazıt University (2013 - 2018)
Master Degree **:** Ankara Yıldırım Beyazıt University (2020 - 2022)

WORK EXPERIENCE

Production eng. **:** SKYMARK Aerospace (2018 – 2021)

Scientific Programs
Assistant Specialist **:** TÜBİTAK (2021-continued)

PUBLICATIONS

Conference Proceedings / Presentations

[1] Sancar, Y., & Sarıkavak, Y. Weldability Process of Dissimilar Alloy Steel Materials and Post Welding Mechanical Analysis. 8th International Marmara Sciences Congress, Kocaeli, Turkey, 2022